ELECTRICAL IMPEDANCE COMPUTED TOMOGRAPHY -- ALGORITHMS AND SYSTEMS

by

Zhen Mu

A thesis

presented to the University of Manitoba

in partial fulfillment of the

requirements for the degree of

Doctor of Philosophy

Department of Electrical and Computer Engineering

Winnipeg, Manitoba, 1994

ISBN 0-612-13386-9

Name Zhen Mu

Dissertation Abstracts International is arranged by broad, general subject categories. Please select the one subject which most nearly describes the content of your dissertation. Enter the corresponding four-digit code in the spaces provided.

ELECTRONICS AND ELECTRICAL

SUBJECT TERM

0544

SUBJECT CODE

U·M·I

Subject Categories

THE HUMANITIES AND SOCIAL SCIENCES

COMMUNICATIONS AND THE ARTS
- Architecture 0729
- Art History 0377
- Cinema 0900
- Dance 0378
- Fine Arts 0357
- Information Science 0723
- Journalism 0391
- Library Science 0399
- Mass Communications 0708
- Music 0413
- Speech Communication 0459
- Theater 0465

EDUCATION
- General 0515
- Administration 0514
- Adult and Continuing 0516
- Agricultural 0517
- Art 0273
- Bilingual and Multicultural 0282
- Business 0688
- Community College 0275
- Curriculum and Instruction 0727
- Early Childhood 0518
- Elementary 0524
- Finance 0277
- Guidance and Counseling 0519
- Health 0680
- Higher 0745
- History of 0520
- Home Economics 0278
- Industrial 0521
- Language and Literature 0279
- Mathematics 0280
- Music 0522
- Philosophy of 0998
- Physical 0523
- Psychology 0525
- Reading 0535
- Religious 0527
- Sciences 0714
- Secondary 0533
- Social Sciences 0534
- Sociology of 0340
- Special 0529
- Teacher Training 0530
- Technology 0710
- Tests and Measurements 0288
- Vocational 0747

LANGUAGE, LITERATURE AND LINGUISTICS
- Language
  - General 0679
  - Ancient 0289
  - Linguistics 0290
  - Modern 0291
- Literature
  - General 0401
  - Classical 0294
  - Comparative 0295
  - Medieval 0297
  - Modern 0298
  - African 0316
  - American 0591
  - Asian 0305
  - Canadian (English) 0352
  - Canadian (French) 0355
  - English 0593
  - Germanic 0311
  - Latin American 0312
  - Middle Eastern 0315
  - Romance 0313
  - Slavic and East European 0314

PHILOSOPHY, RELIGION AND THEOLOGY
- Philosophy 0422
- Religion
  - General 0318
  - Biblical Studies 0321
  - Clergy 0319
  - History of 0320
  - Philosophy of 0322
- Theology 0469

SOCIAL SCIENCES
- American Studies 0323
- Anthropology
  - Archaeology 0324
  - Cultural 0326
  - Physical 0327
- Business Administration
  - General 0310
  - Accounting 0272
  - Banking 0770
  - Management 0454
  - Marketing 0338
- Canadian Studies 0385
- Economics
  - General 0501
  - Agricultural 0503
  - Commerce-Business 0505
  - Finance 0508
  - History 0509
  - Labor 0510
  - Theory 0511
- Folklore 0358
- Geography 0366
- Gerontology 0351
- History
  - General 0578
  - Ancient 0579
  - Medieval 0581
  - Modern 0582
  - Black 0328
  - African 0331
  - Asia, Australia and Oceania 0332
  - Canadian 0334
  - European 0335
  - Latin American 0336
  - Middle Eastern 0333
  - United States 0337
- History of Science 0585
- Law 0398
- Political Science
  - General 0615
  - International Law and Relations 0616
  - Public Administration 0617
- Recreation 0814
- Social Work 0452
- Sociology
  - General 0626
  - Criminology and Penology 0627
  - Demography 0938
  - Ethnic and Racial Studies 0631
  - Individual and Family Studies 0628
  - Industrial and Labor Relations 0629
  - Public and Social Welfare 0630
  - Social Structure and Development 0700
  - Theory and Methods 0344
- Transportation 0709
- Urban and Regional Planning 0999
- Women's Studies 0453

THE SCIENCES AND ENGINEERING

BIOLOGICAL SCIENCES
- Agriculture
  - General 0473
  - Agronomy 0285
  - Animal Culture and Nutrition 0475
  - Animal Pathology 0476
  - Food Science and Technology 0359
  - Forestry and Wildlife 0478
  - Plant Culture 0479
  - Plant Pathology 0480
  - Plant Physiology 0817
  - Range Management 0777
  - Wood Technology 0746
- Biology
  - General 0306
  - Anatomy 0287
  - Biostatistics 0308
  - Botany 0309
  - Cell 0379
  - Ecology 0329
  - Entomology 0353
  - Genetics 0369
  - Limnology 0793
  - Microbiology 0410
  - Molecular 0307
  - Neuroscience 0317
  - Oceanography 0416
  - Physiology 0433
  - Radiation 0821
  - Veterinary Science 0778
  - Zoology 0472
- Biophysics
  - General 0786
  - Medical 0760

EARTH SCIENCES
- Biogeochemistry 0425
- Geochemistry 0996
- Geodesy 0370
- Geology 0372
- Geophysics 0373
- Hydrology 0388
- Mineralogy 0411
- Paleobotany 0345
- Paleoecology 0426
- Paleontology 0418
- Paleozoology 0985
- Palynology 0427
- Physical Geography 0368
- Physical Oceanography 0415

HEALTH AND ENVIRONMENTAL SCIENCES
- Environmental Sciences 0768
- Health Sciences
  - General 0566
  - Audiology 0300
  - Chemotherapy 0992
  - Dentistry 0567
  - Education 0350
  - Hospital Management 0769
  - Human Development 0758
  - Immunology 0982
  - Medicine and Surgery 0564
  - Mental Health 0347
  - Nursing 0569
  - Nutrition 0570
  - Obstetrics and Gynecology 0380
  - Occupational Health and Therapy 0354
  - Ophthalmology 0381
  - Pathology 0571
  - Pharmacology 0419
  - Pharmacy 0572
  - Physical Therapy 0382
  - Public Health 0573
  - Radiology 0574
  - Recreation 0575
  - Speech Pathology 0460
  - Toxicology 0383
- Home Economics 0386

PHYSICAL SCIENCES

Pure Sciences
- Chemistry
  - General 0485
  - Agricultural 0749
  - Analytical 0486
  - Biochemistry 0487
  - Inorganic 0488
  - Nuclear 0738
  - Organic 0490
  - Pharmaceutical 0491
  - Physical 0494
  - Polymer 0495
  - Radiation 0754
- Mathematics 0405
- Physics
  - General 0605
  - Acoustics 0986
  - Astronomy and Astrophysics 0606
  - Atmospheric Science 0608
  - Atomic 0748
  - Electronics and Electricity 0607
  - Elementary Particles and High Energy 0798
  - Fluid and Plasma 0759
  - Molecular 0609
  - Nuclear 0610
  - Optics 0752
  - Radiation 0756
  - Solid State 0611
- Statistics 0463

Applied Sciences
- Applied Mechanics 0346
- Computer Science 0984
- Engineering
  - General 0537
  - Aerospace 0538
  - Agricultural 0539
  - Automotive 0540
  - Biomedical 0541
  - Chemical 0542
  - Civil 0543
  - Electronics and Electrical 0544
  - Heat and Thermodynamics 0348
  - Hydraulic 0545
  - Industrial 0546
  - Marine 0547
  - Materials Science 0794
  - Mechanical 0548
  - Metallurgy 0743
  - Mining 0551
  - Nuclear 0552
  - Packaging 0549
  - Petroleum 0765
  - Sanitary and Municipal 0554
  - System Science 0790
- Geotechnology 0428
- Operations Research 0796
- Plastics Technology 0795
- Textile Technology 0994

PSYCHOLOGY
- General 0621
- Behavioral 0384
- Clinical 0622
- Developmental 0620
- Experimental 0623
- Industrial 0624
- Personality 0625
- Physiological 0989
- Psychobiology 0349
- Psychometrics 0632
- Social 0451

ELECTRICAL IMPEDANCE COMPUTED TOMOGRAPHY-

ALGORITHMS AND SYSTEMS

BY

ZHEN MU

A Thesis submitted to the Faculty of Graduate Studies of the University of Manitoba in partial fulfillment of the requirements for the degree of

DOCTOR OF PHILOSOPHY

Dedicated to

China

and to

my father Chengzhang Mu

and

my mother Shuchun Liu

ABSTRACT

Electrical Impedance Computed Tomography (EICT) seeks to create an image of the conductivity distribution inside a body, based on boundary measurements. This thesis studies one class of EICT algorithms with iterative characters—the error function minimization algorithms—whose features have not been fully explored. Research shows that these algorithms can reconstruct images from under–determined problems, while the algorithms with Newton–Raphson–like procedures cannot do. With the use of the sparse matrix technique and the Point Iterative Point Accumulative scheme, the algorithms are capable of dealing with large amount of data generated from three–dimensional EICT systems. Compared with other algorithms, they are relatively insensitive to measurement errors. Acceleration schemes based on imaging processing techniques are introduced to improve the speed of convergence and the quality of images. Designing excitation patterns is a key issue of EICT systems. This thesis suggests two approaches, with sensitivity analysis and graph theory, to design better excitation patterns. Such designs do not require excitation patterns to be updated during the imaging procedure. Searching for a proper finite element mesh depends on the true conductivity distribution of individual problems. This thesis proposes a procedure of starting an algorithm with a coarse mesh and switching to a finer mesh later to reduce computing time, and to find a mesh that is suitable for a particular problem. The contradiction between image resolution and reconstruction speed is also discussed in this thesis. An alternate method, associated with the error function minimization algorithms, is introduced to increase resolution economically. It solves electrical field potentials with a pre–designed mesh, but improves element conductivities by interpolating conductivity distribution within each element. Simulations in two– and three–dimensions using the discussed algorithms are conducted. Excitation pattern effects on three–dimensional images are specially addressed. A set of principles for industrial applications is then presented and a real EICT system is described.

ACKNOWLEDGMENTS

First of all, I wish to express my sincere and profound gratitude to my adviser, Dr. A. Wexler, for his introducing me to this topic, and for his valuable guidance, encouragement, discussions and support in every phase of this work. His critical comments and thoughtful corrections on my research work always pointed me in the right direction. Many thanks are due to Dr. R. Gordon and Dr. W. Moon for their valuable discussions and suggestions during the research and their critical review for this thesis. Thanks are also given to Dr. Robert Allen for his help at the beginning of my work, to Mr. Guye Strobel of Atomic Energy Canada Ltd. for his experimental measurements, and to Mr. Yonghua Liu for his discussions. Quantic Electroscan Inc. is thanked for providing the preliminary programs and results for the start of this work.

The University of Manitoba Graduate Fellowship, financial support from an NSERC grant, and the Scholarship from the World Bank are greatly acknowledged.

At this moment, I would like to thank all my teachers throughout my education. Special thanks are given to Mr. Chuyan Chen, Professor Mingda Qin, Professor Minghao Zhang, Professor Ruji Huang, and Professor Kai Zuo. Their patient guidance, valuable advice, and critical corrections gave me the ability and the strength to finish this work.

Finally, I wish to express my special gratitude to my dearest parents, Chengzhang Mu and Shuchun Liu, and my brothers, Jun Mu and Min Mu, for their love, understanding, encouragement and patience, and to my husband, Chuanzhu Shi, for his love and support during this study.

LIST OF TABLES

LIST OF FIGURES

CONTENTS

CHAPTER 1

INTRODUCTION

In recent years, Electrical Impedance Computed Tomography(EICT) has received increasing attention. Progress in image reconstruction algorithms has been achieved and applications in biomedicine and in geophysics have been reported[4, 13, 37]. EICT offers the advantages of reduced biological hazard and less expensive hardware. As a result, it can be used as an alternative means for continuous monitoring in medical or environmental applications.

1.1 Electrical Impedance Computed Tomography

Electrical impedance methods have been used in geological and mineral prospecting applications for a long time[38]. Such methods is to employ an artificial source of current which is introduced into the ground through point electrodes or long–line contacts. By measuring potentials at other electrodes in the vicinity of the current flow, it is then possible to determine an effective or apparent resistivity of the subsurface.

Electrical impedance methods have also been applied in the medical field to measure certain overall cardiac parameters, such as intrathoracic fluid volumes, based on large conductivity contrasts in the human body (due mainly to the salinity differences between fluids contained within and between various organs). Henderson and Webster[13] built an "Impedance Camera" system to display isoadmittance contours of the chest under the assumption that the currents injected into the body flowed in a ray–like manner. Current through each electrode arranged on a patient's back was recorded, and the corresponding impedance of the volume was calculated for contour display. Although this technique does not account for current spread throughout inhomogenerous body organs and so cannot yield detailed images, the information could be a significant diagnostic tool, particularly in cases of pulmonary edema.

EICT is a development of the traditional electrical impedance measurement methods. It attempts to image the electrical impedance (or resistivity/conductivity) distribution inside a body using electrical measurements on its boundary. When a current is injected into a body through its surface, potential distribution on the surface is measured.

The main differences between EICT and traditional electrical impedance measurement methods are that: first, the distribution of the conductivity inside a body is not in any presumed pattern (currents do not flow in a ray–like pattern as for X–ray tomography); and second, the target model is not constructed based on lumped–elements, i.e. not network models, but by electrical field estimations.

1.2 Developments on EICT Models and Algorithms

Price[31] first introduced the term EICT in 1978, indicating the application possibilities for EICT in medical science and proposing network models for an EICT medical system. However, such models, as shown in Figure 1.1, were proven to be too simple to represent the elec-

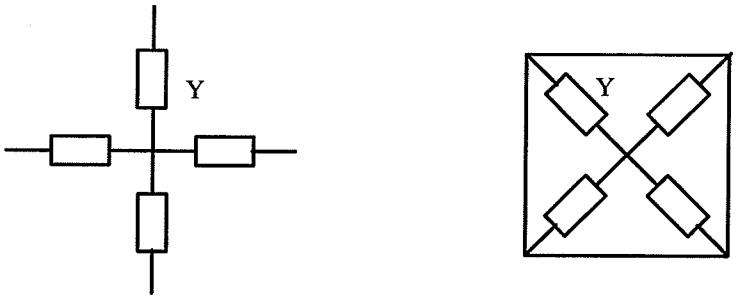

Figure 1.1 Network models proposed by Price for EICT

trical current behaviour within the body. The algorithm Price suggested for the reconstructing conductivity distribution produced images of low quality[2].

Wexler, Fry and Neuman[41] investigated the problem and pointed out that part of the reason for the poor image quality, with the prior proposal and some other related methods, was that they all assumed that the current injected into the body followed ray–like paths. In fact, true current paths depend on the conductivity distribution inside the body, which is unknown at

the outset. The effect of contact and spreading resistance, thus included, lowers the quality of measurements that need to be accurate in order to produce fine tomographic detail.

To describe the current flow path in a continuous medium correctly, electric field equations, i.e. the Poisson or the Laplace equations at low frequencies, must be employed in EICT algorithms. As the method considered to be most suitable for the problems not only in the field with arbitrary geometry but also of the inhomogeneous field, the Finite Element Method (FEM) is appropriate to calculate potential distributions during the EICT imaging process[4, 22]. Wexler, Fry and Neuman[41] and Murai and Kagawa[27] therefore introduced finite element models for this method and discussed the conductivity distribution estimation procedure from electric field solution and network sensitivity theory, respectively. They indicated that the estimation of electrical conductivity distribution within the body is an inverse and nonlinear problem. As a result, an iterative approach had to be implemented for image reconstruction.

With improvements of EICT, Tamburi, Roeper, and Wexler[37] applied their algorithm to the mapping of an effluent plume in the vicinity of a leaking landfill site. Woo et al. [44] using simulation and human body experiments demonstrated that average lung resistivity can be measured with an EICT system using the modified Newton–Raphson algorithm. For the purpose of environmental protection, Atomic Energy of Canada Ltd. has proposed and is testing an initial prototype of an EICT system, to image saturation levels for monitoring buffer material in high–level radioactive waste repositories[35, 36].

1.3 Applications of EICT

Although EICT is still in a research and development phase, many successful experiments and applications indicate its potential for future use within the industry.

1.3.1 Environmental monitoring

With the end of the Cold War, stored nuclear material and wastes in the United States and

Russia have become a recognized threat to our environment. Reportedly, "during the Cold War, a corner of Washington state was home to the plutonium industry. Cleaning up the deadly mess is now providing the biggest environmental challenge ever". There are 14 US nuclear weapon industries spread over 14 main locations in the United States. Hanford, Washington is estimated to have two–thirds of the highly radioactive waste. From 1945 to 1986, an estimated 190,000 cubic meters of highly radioactive waste and 760 billion litres of less radioactive liquid waste and toxic chemicals were stored, dumped or poured into ground there. From the nuclear pollution point of view, people in North America and Russia are living on the most polluted places on Earth. Long–term monitoring is needed while the cleaning up of waste proceeds. EICT may provide an economical, safe, and convenient way to conduct monitoring. Atomic Energy Canada Ltd. is building an EICT system for such a purpose. The simulation and primary experimental results are in conformity with the theoretical calculations.

1.3.2 Medical applications

EICT has potential for use in medical applications, due mainly to impedance differences between different tissues and organs. Table 1.1 shows the impedance differences between some typical parts of the human body at low frequencies.

Breast cancer diagnosis Approximately 1 in 12 Canadian women will develop breast cancer over their lifetimes. Every year some 9000 Canadian women develop breast cancer (about 74 per 100,000)[47]. Although curable, particularly when detected at an early stage, breast cancer kills 4300 Canadian women per year (about 33 per 100,000) and is the major cause of cancer deaths among women. Because it tends to occur earlier in life than other cancers, and earlier than other major causes of death – such as cardiovascular disease—, breast cancer has been shown to be the greatest cause of early loss of life among Canadian women. In many western countries, the yearly incidence is between 75 and 95 cases per 100,000 women and increasing. It is one of the leading causes of death in women over 30 years of age.

Table 1.1

Resistivity of body tissues at low frequencies

Tissue	Resistivity
Blood	208
Liver	506
Heart	216
Lung	744
Fat	2060
Skeletal	643

* Mean resistivity in Ohm.cm

The means to prevent breast cancer has not been found. Mammography used to be considered as the only reliable method of detecting nonpalpable cancers, and could detect many small breast cancers in the early stages when they may still be curable. However, there are questions on its reliability now. Besides, mammography involves radiation, and is expensive to apply in clinical bases. In recent years, there has been a great interest in developing alternative techniques for breast cancer imaging. Potentially fruitful areas for research are: digital mammography, applications of digital imaging process and pattern recognition techniques in digital mammography, and digital diagnosis.

EICT is one such area which may be able to provide inexpensive and less hazardous diagnosis of breast cancer in its early stage. Research has been carried out in measuring the impedance of breasts[18]. The resistivity of cancer tissue is about 20 times higher than that of normal breast tissue. Simulation results in two–dimensions show that a tumor area covering 1% of the cross–sectional breast model area produces more than 4% of the variation in voltage magnitude at the surface electrodes when compared to voltages for a normal breast. As a relatively new breast cancer detection approach, EICT may provide earlier detection than

is currently possible. This technique would also be effective on young women[18].

Other possible diagnoses Based on the discussion above on the possible medical applications of EICT, we can see the potential for diagnosing other lung diseases, or monitoring heart movement dynamically, when X–ray based techniques cannot be used.

1.3.3 Mine detection

There are still dangerous places on the Earth as a result of major wars. In Cambodia, for example, life is continuously threatened by underground mines. It was reported that 6 to 10 million explosive mines can still be found in rural areas, making shortage of cultivatable land there even more critical. Traditional detection methods cannot solve this problem because most of the mines are covered with plastic materials. EICT is considered to be the only way possible to clear that land. In Canada, there are unexploded underground ordnance at Suffield, Alberta. It would take years to clean them up using traditional methods. The Department of National Defence has tried to find efficient approaches to detecting those ordnances. Again, EICT might be a way to distinguish metal and plastic–covered ordnance from soil.

1.4 Purposes of This Thesis Research

Although significant progress has been made in EICT algorithms and systems, this method is still in its research stage as a relatively new image–generating technique. EICT's potential applications in environmental and medical areas demand more thorough studies related to industrial settings. This thesis describes research conducted on EICT algorithms as well as problems arising from practical EICT systems. It seeks to formulate a set of theoretical and practical principles on which to base an industrial (medical/environmental) EICT machine.

1.4.1 Studying EICT algorithms

Algorithm development has been the major research area of EICT. For EICT algorithms with iterative features, those using Newton–Raphson–like procedures have been studied the most. Such algorithms give faster convergence rates than other iterative algorithms. However, the large matrix inversion restricts the algorithm's ability to deal with large, three–di-

mensional imaging systems, which is important in practical applications. This thesis investigates alternate types of iterative EICT algorithms that do not use Newton–Raphson–like procedures and have not been fully studied. The sparse–matrix technique and the Point Iterative Point Accumulative method for field solutions[33] can be introduced in these algorithms to enhance their ability to handle large, three–dimensional systems. Previous comparisons of different algorithms showed that the speed of convergence of this type of algorithm is slow. Improvements on the convergence rate, therefore, are sought in this thesis.

There are other EICT algorithms[1, 11, 12, 39, 40], such as backprojection. Some of the algorithms assume that current flows in a ray–like manner, while others do not have iterative characters. Research on those algorithms is beyond the scope of this thesis. We have focused only on iterative algorithms which produce solutions from electric field equations directly without any assumption about the paths of injected current.

1.4.2 Research on EICT's resolution

EICT is currently considered to be a low–resolution technique. Little work has been done to investigate the causes of this problem and possible improvements. Two causes of low resolution are discussed in this thesis. One is that the number of electrodes in an EICT system limits the number of unknown element conductivities. The average element size of a finite element mesh therefore cannot be designed fine enough to accommodate the actual sizes of small objects existing in the region to be examined or to describe the sharp edges of objects. The other cause is that the precision of measured boundary potentials cannot reflect small changes caused by variations in conductivity distribution.

This thesis tries to find an another way to increase the resolution of EICT image under limited measurements. It also includes research to improve image quality in areas where boundary measurements are sensitive to the conductivity changes.

1.4.3 Investigating modelling effects on algorithm success and image quality

Most of the previous simulation results using different EICT algorithms were obtained by assuming congruency between the objects and a finite element mesh. Such an artificial situa-

tion in image reconstruction makes the simulation results less realistic. In practice, the shapes of objects and contrasts between objects and background are unknown. As a result, the proper mesh suitable for a particular problem is unknown in advance. It is impossible to design a finite element mesh that exactly covers the shape of the objects. This thesis investigates the effects of non–congruence (i.e. when the edges of a finite element mesh do not describe target objects exactly) on the success of EICT algorithms and the quality of EICT images. Schemes to search for a suitable mesh for each individual EICT imaging problem are proposed.

1.4.4 Three–dimensional imaging simulations with EICT

Most of the reported simulations and experiments with different EICT algorithms dealt with images reconstructed using two–dimensional finite element models. It is believed that the principles of algorithms which are successful in two–dimensional imaging would be easily extended to the three–dimension space. However, there are specific requirements to be satisfied in three–dimensional EICT imaging which have to be discussed if an EICT system is to be realized. Industrial applications of EICT require images recovered from solid three–dimensional electrical field models by appropriate algorithms within a reasonable computing time. In most applications, excitations/measurements on all six sides of a three–dimensional body are not allowed. For example, mine detection problem is one of such cases where it is a problem to reconstruct object images in a three–dimensional body with excitations/measurements available only on the top two–dimensional surface. Breast cancer diagnosis with EICT is also such a problem since it allows excitations/measurements placed on five sides of a breast, if, for the simplicity, recovering the breast as a cube. There has been limited discussions and research on the effects of the limited excitations/measurements in three–dimensional EICT imaging. Another feature of EICT in three dimensions is the complexity of finite element models. Since the amount of data to be processed in a three–dimensional EICT system is much larger, compared with those in a two–dimensional system, the finite element model cannot be as complicated as that in a two–dimensional problem. This thesis simulates

three–dimensional problems with solid finite element models, and studies image quality with incomplete excitations/measurements.

1.4.5 Designing excitation patterns

Design of excitation pattern is important to the success of EICT algorithms. Previous work focused on searching for better current injection patterns which induce the maximally measurable boundary potentials[10, 17]. Since the best excitation patterns depend on the known conductivity, these kinds of designs result in on–line data processing and hence difficulties in eliminating contact resistances. This thesis discusses the relationships between the image quality and the convergence speed with different excitation patterns. Methods of designing excitation patterns which do not depend on the *a priori* knowledge of the true image are desirable. Better excitation patterns can be decided before an EICT algorithm begins, and the original approaches to eliminating contact resistance will not be affected.

1.4.6 Outline of the thesis

In the first and second chapters, this thesis presents a general review on the research and applications of EICT and important previous work done in developing efficient iterative EICT algorithms. Error function minimization algorithms are selected as the algorithms, since they are suitable for EICT three–dimensional imaging. It is also pointed out in Chapter 2 that the speed of convergence should not be taken as the only factor when EICT algorithms are evaluated.

In Chapter 3, the thesis proposes the use of a multi–port resistive network as the discretized model for EICT to eliminate discretization effects introduced by numerical methods when EICT algorithms are used in continuous conductivity distribution imaging. Then, network theory can be used in guiding the analysis of EICT problems, such as the excitation/measurement effects of various EICT methods. Graph theory and sensitivity analysis based algorithms are developed for excitation/measurement pattern designs of EICT systems. The network recovery shows an important feature of the error function minimization algorithms: under–determined problems can be handled, which the algorithms with Newton–Raphson

like procedures cannot solve. The thesis also discusses the possibility of, and schemes for placing the limited number of electrodes more efficiently, to reveal interior details of interest.

Chapters 4 and 5 explain the causes of a slow convergence rate of error function minimization algorithms and propose improvements to speed up convergence. An image processing technique based method, i.e. peak detection method, is then introduced to predict possible positions of target objects. An adaptive modification scheme and an acceleration factor are put into the element conductivity updating procedure to speed up convergence. Simulation results show significant improvements in convergence speed and image quality. The sharp edges of objects can be better recovered. The image processing technique combined with the function minimization method, gives an alternate way to improve solutions in EICT inverse problems.

The design of a finite element mesh used by EICT algorithms also affects both the convergence speed and the image quality. To date, there has never been complete discussions on such issues. Chapter 6 addresses the relationships between the finite element meshes and the final solutions. It suggests the use of different meshes in evaluating field potentials and in updating conductivity distribution. The method discussed in this chapter resolves the controversy of finer finite element meshes and limited numbers of electrodes used in an EICT system. It can greatly improve the image quality without increasing computational effort. The effect of finite element mesh refinement on solution uniqueness is also discussed. A procedure is proposed to make use of various mesh densities in the EICT imaging process to find a suitable mesh for a particular problem. Such a procedure avoids using a too fine mesh at the beginning of a solution process and keeps rapid convergence speed to a preset limit until an educated initial guess for a better mesh is reached.

Chapter 7 discusses two– and three–dimensional imaging procedure with EICT algorithms. A solid finite element model in three dimensions is set up for the purpose of three–dimensional simulations. With the help of network models, the effects of excitations/measure-

ments on image quality in two– and three–dimensional imaging are addressed. EICT algorithms cannot be employed in an industrial system unless its robustness is tested. In Chapter 7, a number of simulations are carried out to determine how image quality is affected by the boundary distortion effect and the measurement random error effect. It is demonstrated that error function minimization algorithms and improvements introduced in this thesis are relatively robust.

Chapter 8 summarizes the results of research which the thesis discovers and builds on the findings of Chapter 3 to 7 by giving a set of guidelines for designing EICT systems by industrial applicants. As an example, the EICT system developed and tested by the Atomic Energy Canada Ltd. is described in this chapter.

There are still many issues that need to be discussed. Chapter 9 presents the conclusions learnt in this thesis work and proposes possible research topics to be performed in the future.

CHAPTER 2

EICT ALGORITHM SUMMARY

Most EICT algorithms are nonlinear reconstruction algorithms with iterative characters. Starting from an initial guess of a given conductivity distribution, an algorithm is applied to update conductivity in a way that creates a steady improvement in the agreement between predicted and measured data. The main issues in such algorithms are stability and speed of convergence. In the past decade, efforts have been made to develop EICT algorithms with faster convergence speed and to devise other schemes to improve image quality[4, 15, 46]. Optimal reconstruction algorithms are still under development.

Most of the iterative EICT algorithms currently used employ the Poisson (Laplace) equation to describe the continuous electrical field problems and solve potential distributions with the Finite Element Method (FEM) . They can be classified into two types: one solves the electrical field equations by applying different boundary conditions to the body, and searches for the true conductivity distribution by minimizing the specified error functions with a least–square technique; the other connects conductivity distribution changes with the transfer impedance for a pair of current and voltage electrodes by network sensitivity theory[27], and improves the estimated conductivity distribution iteratively with Newton–Raphson–like procedures. In this thesis, we call the first type "Error Function Minimization Algorithms"; and the second type, "Matrix Inversion Algorithms".

2.1 The Finite Element Method

One of the main differences between traditional electrical impedance measurement methods and EICT is that the latter uses electric field equations to govern this inverse problem without assuming electric current paths in advance. FEM is the numerical method used in solving electric field equations to obtain the potential distributions inside the region of interest under

an assumed conductivity distribution and boundary conditions.

2.1.1 Numerical solution of the Poisson's equation with the FEM

The Poisson equation is given by

$$-\nabla \cdot \kappa \nabla \phi = f \tag{2–1}$$

where κ, ϕ, and f are the conductivity, potential distributions, and current source distributions within the region. The first step of the FEM divides the region of interest up into many smaller regions called elements. The total region is then described on an element–by–element basis. The most common shape for individual elements is the triangle or quadrilateral. Figure 2.1 shows a two–dimensional region with quadrilateral elements.

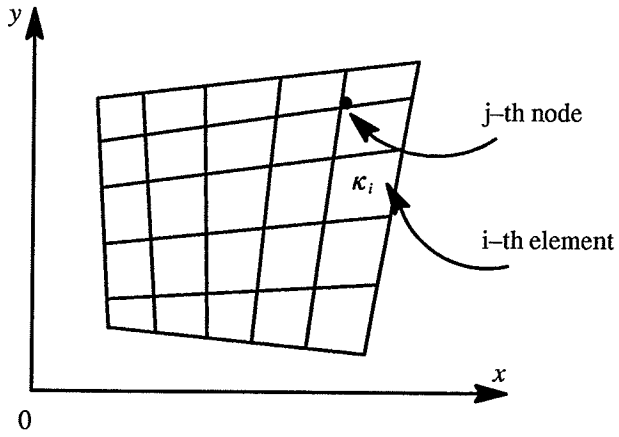

Figure 2.1 An arbitrary region divided into quadrilateral elements

The FEM uses the variational principle, in which the field is represented using a piecewise continuous function and the variational integral is minimized with respect to the residual or functional to best approximate the actual field. A complete description of the variational method is given by Mikhlin[22].

When the total region is divided into smaller elements, the values of conductivity κ_i within each element are assumed to be constant. The field ϕ is given by

$$\phi = \sum_{i=1}^{n} \alpha_i(x, y)\phi_i \tag{2–2}$$

where $\alpha_i(x, y)$, known as a shape function in the FEM, is the interpolation polynomial defined

over the x–y surface for node i, and n is the total number of nodes within the element. Equation (2–2) then can be written as

$$\phi = \underline{\alpha}^T \underline{\phi} = \underline{\phi}^T \underline{\alpha} \tag{2–3}$$

The appropriate functional for the solution of the Poisson's equation is

$$F = \int\int_B \kappa[(\frac{\partial \phi}{\partial x})^2 + (\frac{\partial \phi}{\partial y})^2]\ dxdy - 2\oint_B \phi h\ ds - 2\int\int_B \phi f\ dxdy \tag{2–4}$$

where h is the Neumann condition on the boundary. To find the minimum, (2–4) is differentiated with respect to the variational parameter ϕ and set to zero. Then,

$$\frac{\partial F}{\partial \phi} = 2\int\int_B \kappa[\frac{\partial \phi}{\partial x}\frac{\partial(\frac{\partial \phi}{\partial x})}{\partial \phi} + \frac{\partial \phi}{\partial y}\frac{\partial(\frac{\partial \phi}{\partial y})}{\partial \phi}]\ dxdy - 2\frac{\partial}{\partial \phi}\oint_B \phi h\ ds - 2\frac{\partial}{\partial \phi}\int\int_B \phi f\ dxdy = 0 \tag{2–5}$$

Substituting (2–2) into (2–5) and differentiating with respect to the new variational parameter ϕ_i, we have

$$\frac{\partial F}{\partial \phi_i} = 2\int\int_B \kappa[\frac{\partial \phi}{\partial x}\frac{\partial(\frac{\partial \phi}{\partial x})}{\partial \phi_i} + \frac{\partial \phi}{\partial y}\frac{\partial(\frac{\partial \phi}{\partial \phi})}{\partial \phi_i}]\ dxdy - 2\int_B h\frac{\partial \phi}{\partial \phi_i}\ ds - 2\int\int_B f\frac{\partial \phi}{\partial \phi_i}\ dxdy = 0 \tag{2–6}$$

Since

$$\frac{\partial \phi}{\partial \phi_i} = \alpha_i \qquad \frac{\partial(\frac{\partial \phi}{\partial \phi_i})}{\partial x} = \frac{\partial \alpha_i}{\partial x} \qquad \frac{\partial(\frac{\partial \phi}{\partial \phi_i})}{\partial y} = \frac{\partial \alpha_i}{\partial y}$$

and

$$\frac{\partial \phi}{\partial x} = \frac{\partial \alpha_1}{\partial x}\phi_1 + \frac{\partial \alpha_2}{\partial x}\phi_2 + \ldots$$

(2–6) can be reduced to

$$\int\int_B \kappa[(\frac{\partial \alpha_i}{\partial x}\phi_i + \frac{\partial \alpha_j}{\partial x}\phi_j + \ldots)\frac{\partial \alpha_i}{\partial x} + (\frac{\partial \alpha_i}{\partial y}\phi_i + \frac{\partial \alpha_j}{\partial y}\phi_j + \ldots)\frac{\partial \alpha_i}{\partial y}]\ dxdy$$

$$- 2\int_B h\alpha_i ds - 2\int\int_B f\alpha_i\ dxdy = 0 \qquad i,j = 1,2,\ldots,n \tag{2–7}$$

The first integral yields a square n x n matrix where n is the number of variational nodal points and the latter two integrals can be summed to yield a vector of length n. The resulting set of linear equations can be put in standard matrix form as

$$S\underline{\phi} = \underline{b} \tag{2–8}$$

where

$$s_{ij} = \int\int_B \kappa\left(\frac{\partial\alpha_i}{\partial x}\frac{\partial\alpha_j}{\partial x} + \frac{\partial\alpha_i}{\partial y}\frac{\partial\alpha_j}{\partial y}\right) dxdy \tag{2–9}$$

$$b_{ij} = \int_B h\alpha_i ds + \int\int_B f\alpha_i \, dxdy \qquad i,j = 1,2,\ldots,n \tag{2–10}$$

and ϕ_i are the unknowns to be solved.

The problem now is to perform the integrations. One approach is to map a standard square element into a general quadrilateral before integration. The transformation

$$x = \sum_{i=1}^{4} \alpha_i(\xi,\eta)x_i \qquad y = \sum_{i=1}^{4} \alpha_i(\xi,\eta)y_i \tag{2–11}$$

is used to map the square element in local coordinates to the general quadrilateral in global coordinates as shown in Figure 2.2.

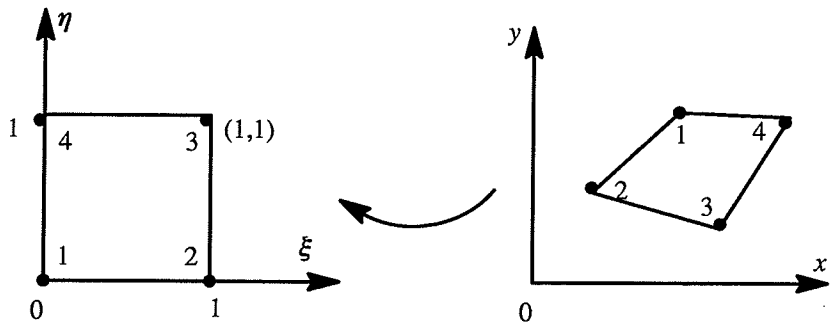

Figure 2.2 Transformation from local to global coordinates

The shape functions for the standard element in $\xi-\eta$ space are

$$\alpha_1 = (1-\xi)(1-\eta) = 1-\xi-\eta+\xi\eta$$

$$\alpha_2 = \xi(1-\eta) = \xi-\xi\eta$$

$$\alpha_3 = \xi\eta$$

$$\alpha_4 = \eta(1-\xi) = \eta + \xi\eta \tag{2–12}$$

To integrate (2–9), we then introduce new variables of integration

$$x = x(\xi,\eta) \qquad y = y(\xi,\eta)$$

To map the element in local space to global space, the Jacobian transformation is introduced as

$$J = \frac{\partial(x,y)}{\partial(xi,\eta)} = \begin{bmatrix} \frac{\partial x}{\partial \xi} & \frac{\partial x}{\partial \eta} \\ \frac{\partial y}{\partial \xi} & \frac{\partial y}{\partial \eta} \end{bmatrix} \tag{2–13}$$

Then, (2–9) can be simplified as

$$\int\int_B f(x,y)\ dxdy = \int\int_{B^*} f\ [x(\xi,\eta), y(\xi,\eta)]\ |J|\ d\xi d\eta \tag{2–14}$$

The values of $\frac{\partial \alpha_i}{\partial x}$ and $\frac{\partial \alpha_i}{\partial y}$ can then be determined by

$$\begin{bmatrix} \frac{\partial \alpha_i}{\partial x} \\ \frac{\partial \alpha_i}{\partial y} \end{bmatrix} = [J] \begin{bmatrix} \frac{\partial x}{\partial \xi} \\ \frac{\partial y}{\partial \xi} \end{bmatrix} / |J| \tag{2–15}$$

Now, we have a desired result to perform the integration over a square element.

2.1.2 Gaussian quadrature

Many numerical quadrature schemes are available for finite integration over a standard interval. Gaussian quadrature method[4], which can integrate a polynomial of degree $2m-1$ accurately with m sampling locations, is employed in this thesis.

In one dimension, the Gaussian quadrature formula for estimating an integral of a function $f(\xi)$ on the interval $-1 \le \xi \le 1$ takes the form

$$\int_{-1}^{+1} f(\xi)\ d\xi \approx \sum_{i=1}^{m} W_i f(\xi_i) \tag{2–16}$$

where ξ_i is some points located in the interval. W_i is a weight associated with the i–th point,

and m is the number of points. The weights and points are found by supposing that f is a polynomial of degree 2m–1 and then computing the points and weights that guarantee an exact result for such a polynomial. When m is even, all points come in $\pm$ pairs with individual points in each pair having equal weight. When m is odd, $\xi = 0$ is one of the points and the remaining points again come in pairs having equal weights. If $f(\xi) = f_0 + f_1\xi$, then

$$\int_{-1}^{+1} f(\xi)\ d\xi = 2f_0 \equiv W_1 f_0 \tag{2–17}$$

which requires that $\xi_1 = 0$ and $W_1 = 2$. If $f(\xi) = f_0 + f_1\xi + f_2\xi^2 + f_3\xi^3$, then

$$\int_{-1}^{+1} f(\xi)\ d\xi = 2f_0 + 2f_2/3 \equiv 2W_1(f_0 + f_2\xi_1^2) \tag{2–18}$$

which requires that $\xi_1,\ \xi_2 = \pm\frac{1}{\sqrt{3}}$ and $W_1,\ W_2 = 1$. Similarly, if $f(\xi) = \sum_{j=0}^{5} f_j\xi^j$, then

$$\int_{-1}^{+1} f(\xi)\ d\xi = 2f_0 + 2\frac{f_2}{3} + 2\frac{f_4}{5} \equiv 2W_1(f_0 + f_2\xi_1^2 + f_4\xi_1^4) + W_2 f_0 \tag{2–19}$$

which requires that $\xi_1,\ \xi_3 = \pm\sqrt{\frac{3}{5}}$, $\xi_2 = 0$, and $W_1,\ W_3 = \frac{5}{9}$, $W_2 = \frac{8}{9}$. The results of these calculations for one–dimensional integration are summarized in Table 2.1.

For multiple integration in two or three dimensions, the Gaussian quadrature formulas are generalizations of those in one dimension:

$$\int_{-1}^{+1}\int_{-1}^{+1} g(\xi,\eta)\ d\xi d\eta = \sum_{i,j} W_i W_j g(\xi_i,\eta_j) \tag{2–20}$$

and

Table 2.1

Gaussian quadrature weights and locations

# of points	Locations	Weights W_i
1	$\xi_1 = 0$	2
2	$\xi_1, \xi_2 = \pm \frac{1}{\sqrt{3}}$	1
3	$\xi_1, \xi_3 = \pm \sqrt{\frac{3}{5}}$ $\xi_2 = 0$	$\frac{5}{9}$ $\frac{8}{9}$

$$\int_{-1}^{+1}\int_{-1}^{+1}\int_{-1}^{+1} h(\xi,\eta,\zeta)\ d\xi d\eta d\zeta = \sum_{i,j,k} W_i W_j W_k h(\xi_i,\eta_j,\zeta_k) \qquad (2\text{–}21)$$

The same locations and weights may be used in each of directions ξ, η, ζ .

2.1.3 Higher–order and three–dimensional elements

Higher–order approximations may be obtained by adding more nodes to the elements. Then, the degree of approximation can be improved from linear to quadratic by taking 9–node quadrilaterals as shown in Figure 2.3 (a). The higher–order elements used in the FEM can

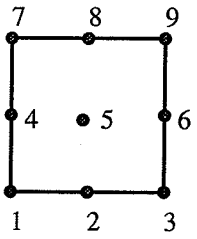

(a) Higher–order element in two dimensions

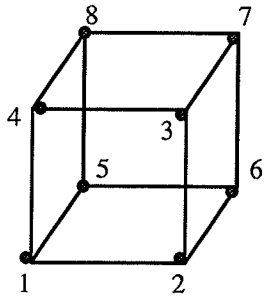

(b) Linear element in three dimensions

Figure 2.3 Higher–order and three–dimensional elements

give better results for problems with curved boundaries. However, increasing the number

of nodes in each element means increasing the number of unknowns in the whole system. More computational effort is then needed.

A simple element of the FEM in three dimensions can be created by adding depth to a two–dimensional element without changing the shape. The standard element in three–dimensions is the linear element with 8 nodes as shown in Figure 2.3 (b).

The complete mathematical derivations for these elements may be found in standard references[4].

2.2 Error Function Minimization Algorithms

An error function minimization algorithm defines an error function based on potential distribution solutions from an initial assumption of conductivity distribution. The conductivity distribution is updated by minimizing the error functions with a least–square technique. Such algorithms include the Wexler algorithm[41], the Kohn–Vogelius algorithm[19], and other algorithms[4]. The main differences between these algorithms are at the element conductivity updating step. This thesis will focus the discussions on the algorithms of Wexler and Kohn–Vogelius in this chapter.

2.2.1 Algorithms of Wexler and Kohn–Vogelius

Wexler, Fry, and Neuman presented their algorithm in 1985, and Kohn and Vogelius reported on a very similar one in 1986. Considering their similarities, only the procedure of the Wexler algorithm is discussed in details.

To perform an EICT algorithm, a grid of electrodes has to be established over the surface of the body to be studied. (The surface would be the ground in the geophysical situations, or the surface of the human body in the medical applications) The basic principle of the EICT algorithm is that the surface voltages measured under a given current density are characteristic of a particular conductivity distribution inside the body. By injecting and extracting current at a pair of electrodes arranged at the surface of the body, and by guessing at the conductivity distribution, one can calculate a potential distribution throughout the body and, of

course, at the surface. In the Wexler algorithm, such calculation is performed by solving the Poisson equation, as described in (2–1), for continuously inhomogeneous media. Since the inverse problem with a single excitation configuration will not, in general, produce a unique solution, the measured potentials on the surface induced by this particular excitation are not sufficient to give an acceptable image of the interior. Therefore, a sequence of linearly independent excitations is necessary. The set of surface potentials corresponding to the sequence of excitations is obtained by solving equation (2–1) using the non–homogenous Neumann boundary condition

$$\kappa(s)\frac{\partial \phi}{\partial n} = h(s) \tag{2–22}$$

where h is current density on the surface of the body.

Assuming a given conductivity distribution, the required energy functional for solving (2–1) is

$$F = \int \kappa \nabla \phi \cdot \nabla \phi \; dv - 2\int \phi f \; dv \tag{2–23}$$

Using the Rayleigh–Ritz discretization procedure described in (2–4)

equation (2–23) becomes

$$F = \underline{\phi}^T \int \kappa \nabla \underline{\alpha} \cdot \nabla \underline{\alpha}^T \; dv \; \underline{\phi} - 2\underline{\phi}^T \int \underline{\alpha} f \; dv \tag{2–24}$$

Differentiating with respect to the field unknowns yields

$$\frac{\partial F}{\partial \underline{\phi}} = 2\int \kappa \nabla \underline{\alpha} \cdot \nabla \underline{\alpha}^T \; dv \; \underline{\phi} - 2\int \underline{\alpha} f \; dv \tag{2–25}$$

which if equated to zero and rearranged becomes

$$\int \kappa \nabla \underline{\alpha} \cdot \nabla \underline{\alpha}^T \; dv \; \underline{\phi} = \int \underline{\alpha} f \; dv \tag{2–26}$$

or as we have seen in (2–8)

$$S\underline{\phi} = \underline{b}$$

where

$$s_{ij} = \int \kappa_i \nabla\alpha_i \cdot \nabla\alpha_j \; dv \tag{2–27}$$

and

$$b_j = \int \alpha_i f_i \; dv \tag{2–28}$$

Equation (2–26) is a system of linear equations that can be solved for the discretized field with different approaches.

Expanding (2–26) along row i and solving for the i–th unknown gives

$$\phi_i = \frac{\int \alpha_i \; f \; dv - \sum_j [\int \kappa_i \nabla\alpha_i \cdot \nabla\alpha_j \; dv] \; \phi_j}{\int \kappa_i \; (\nabla\alpha_i \cdot \nabla\alpha_i) \; dv} \tag{2–29}$$

The conductivity and source may also be expressed as

$$\kappa = \kappa^T \underline{\alpha} = \underline{\alpha}^T \kappa$$

$$f = \underline{f}^T \underline{\alpha} = \underline{\alpha}^T \underline{f} \tag{2–30}$$

so that (2–29) is now

$$\phi_i = \frac{\sum_j \int \alpha_i \alpha_j \; dv \; f_j - \sum_j [\sum_k \int (\nabla\alpha_i \cdot \nabla\alpha_j) \alpha_k \; dv \kappa_k] \phi_j}{\sum_k \int (\nabla\alpha_i \cdot \nabla\alpha_i) \alpha_k \; dv \kappa_k} \tag{2–31}$$

As the shape functions are known, the required integrals are pre–calculated into equivalent weighting factor arrays. Thus, (2–31) is simplified to

$$\phi_i = \frac{\sum_j V_{ij} \; f_j - \sum_{j,j \neq i} [\sum_k W_{ijk} \kappa_k] \phi_j}{\sum_k W_{ijk} \kappa_k} \tag{2–32}$$

If the conductivity is defined as constant throughout each element, (2–32) reduces to

$$\phi_i = \frac{\sum_j V_{ij} f_j - \kappa_{ij} \sum_{jj \neq i} W_{ij} \phi_j}{\kappa_i \sum_k W_{ij}} \tag{2–33}$$

With ϕ known, the electric field intensity is given by

$$\mathbf{E} = -\nabla\phi \tag{2–34}$$

Then, the current density distribution can be determined by

$$\mathbf{J} = \kappa\mathbf{E} = -\kappa\nabla\phi \tag{2–35}$$

which is Ohm's Law in point form.

Because the initial guess of the conductivity is unlikely to correspond to what was actually inside the region when measurements were taken, the calculated and measured potentials will disagree. Then, (2–1) is solved again using the measured surface voltages (potentials), i.e. the Dirichlet boundary condition

$$\phi(s) = g(s) \tag{2–36}$$

where g(s) is the boundary potential distribution.

The disagreement in potential distributions throughout the entire region from the Neumann boundary condition and from the Dirichlet boundary condition can be described as

$$\epsilon_W = \sum_x \int_v (\mathbf{J} + \kappa\nabla\phi) \cdot (\mathbf{J} + \kappa\nabla\phi) \; dv \tag{2–37}$$

This is a least–squares residual form, where x refers to current excitations. Taking the inner product

$$\epsilon_W = \sum_x \int_v (\kappa\nabla\phi \cdot \nabla\phi\kappa + 2\kappa\nabla\phi \cdot \mathbf{J} + \mathbf{J} \cdot \mathbf{J}) \; dv \tag{2–38}$$

It shows the difference between the Dirichlet boundary condition solution and the Neumann boundary condition solution.

Substituting (2–30) into (2–38) gives

$$\epsilon_W = \sum_x \int_v (\kappa^T \underline{\alpha} \nabla\phi \cdot \nabla\phi \underline{\alpha}^T \kappa + 2\kappa^T \underline{\alpha} \nabla\phi \cdot \mathbf{J} + \mathbf{J} \cdot \mathbf{J}) \; dv \qquad (2\text{–}39)$$

A new conductivity distribution can be computed by minimizing (2–39) over the region as

$$\kappa_i^{n+1} = -\frac{\sum_x \int_v \mathbf{J} \cdot \nabla\phi \; dv}{\sum_x \int_v \nabla\phi \cdot \nabla\phi \; dv} \qquad (2\text{–}40)$$

that is

$$\frac{\partial \epsilon_W}{\partial \kappa} = 2 \sum_x \int_v (\underline{\alpha} \nabla\phi \cdot \nabla\phi \underline{\alpha}^T \cdot dv\kappa + 2 \sum_x \int_v \underline{\alpha} \nabla\phi \cdot \mathbf{J} dv = 0 \qquad (2\text{–}41)$$

and simplified to

$$\sum_x \int_v (\underline{\alpha} \nabla\phi \cdot \nabla\phi \underline{\alpha}^T \cdot dv \;\; \kappa = -\sum_x \int_v \underline{\alpha} \nabla\phi \cdot \mathbf{J} dv \qquad (2\text{–}42)$$

which again represents a linear system.

Solving (2–42) for the conductivity at the i–th node produces

$$\kappa_i = \frac{\sum_x \int_v \alpha_i \mathbf{J} \cdot \nabla\phi dv - \sum_x \sum_{j,j \neq i} \int_v (\alpha_i \nabla\phi) \cdot (\nabla\phi \alpha_j) dv \;\; \kappa_j}{\sum_x \int_v (\alpha_i \nabla\phi) \cdot (\alpha_i \nabla\phi) dv} \qquad (2\text{–}43)$$

Using (2–30) the x–component of the field gradient becomes

$$\frac{\partial \phi}{\partial x} = \frac{\partial \underline{\alpha}^T}{\partial x} \underline{\phi} = \underline{\phi}^T \frac{\partial \underline{\alpha}}{\partial x} = \sum_m \frac{\partial \alpha_m}{\partial x} \phi_m \qquad (2\text{–}44)$$

The y– and z–components are generated in a similar manner, and thus (2–43) is written as

$$\kappa_i = \frac{-\sum_x [\sum_m \int_v \alpha_i (J_x \frac{\partial \alpha_m}{\partial x} + J_y \frac{\partial \alpha_m}{\partial y} + J_z \frac{\partial \alpha_m}{\partial z}) \; dv\phi\phi_m] - \sum_x \sum_{jj \neq i} [\sum_l \sum_m \int_v \alpha_i \alpha_j (\frac{\partial \alpha_l}{\partial x} \frac{\partial \alpha_m}{\partial x} + \frac{\partial \alpha_l}{\partial y} \frac{\partial \alpha_m}{\partial y} + \frac{\partial \alpha_l}{\partial z} \frac{\partial \alpha_m}{\partial z}) \; dv\phi_l\phi_m] \kappa_j}{\sum_x [\sum_l \sum_m \int_v \alpha_i^2 (\frac{\partial \alpha_l}{\partial x} \frac{\partial \alpha_m}{\partial x} + \frac{\partial \alpha_l}{\partial y} \frac{\partial \alpha_m}{\partial y} + \frac{\partial \alpha_l}{\partial z} \frac{\partial \alpha_m}{\partial z}) \; dv\phi_l\phi_m]} \qquad (2\text{–}45)$$

Since the current density is not known in advance, it must be determined prior to employing (2–45) in a conductivity calculation. Initially, a conductivity distribution is assumed and using (2–30), the x–component of the current density can be expanded as

$$J_x = -\kappa \frac{\partial \phi}{\partial x} = -\sum_j \alpha_j \frac{\partial \phi}{\partial x} \kappa_j = -\sum_j \sum_l \alpha_j \frac{\partial \alpha_l}{\partial x} \phi_l \kappa_j \qquad (2\text{–}46)$$

Performing similar expansions for J_x and J_z allows (2–46) to be written as

$$\kappa_i^{n+1} = \frac{\sum_x [\sum_j [\sum_m \int_v \alpha_i \alpha_j (\frac{\partial \alpha_l}{\partial x}\frac{\partial \alpha_m}{\partial x} + \frac{\partial \alpha_l}{\partial y}\frac{\partial \alpha_m}{\partial y} + \frac{\partial \alpha_l}{\partial z}\frac{\partial \alpha_m}{\partial z})\, dv \phi_m] - \sum_x \sum_{jj \neq i} [\sum_l \sum_m \int_v \alpha_i \alpha_j (\frac{\partial \alpha_l}{\partial x}\frac{\partial \alpha_m}{\partial x} + \frac{\partial \alpha_l}{\partial y}\frac{\partial \alpha_m}{\partial y} + \frac{\partial \alpha_l}{\partial z}\frac{\partial \alpha_m}{\partial z})\, dv \phi_l \phi_m] \kappa_j^{n+1}}{\sum_x [\sum_l \sum_m \int_v \alpha_i^2 (\frac{\partial \alpha_l}{\partial x}\frac{\partial \alpha_m}{\partial x} + \frac{\partial \alpha_l}{\partial y}\frac{\partial \alpha_m}{\partial y} + \frac{\partial \alpha_l}{\partial z}\frac{\partial \alpha_m}{\partial z})\, dv \phi_l \phi_m]} \qquad (2\text{–}47)$$

which, through the use of weighting factors, simplifies to

$$\kappa_i^{n+1} = \frac{\sum_x [\sum_j [\sum_l \sum_m W_{ijlm} \tilde{\phi}_l \phi_m] \kappa_j^n - \sum_{j,j<>i} \sum_l \sum_m W_{ijlm} \phi_l \phi_m \kappa_j^{n+1}]}{\sum_x \sum_l \sum_m W_{lm} \phi_l \phi_m} \qquad (2\text{–}48)$$

Further simplification is possible by employing constant valued conductivity elements. In this case, (2–42) describes a pure diagonal form and (2–48) reduces to

$$\kappa_i^{n+1} = -\frac{\sum_x \sum_j \sum_l \sum_m W_{ijlm} \tilde{\phi}_l \phi_m \kappa_j^n}{\sum_x \sum_l \sum_m W_{lm} \phi_l \phi_m} \qquad (2\text{–}49)$$

The $\tilde{\phi}$ represents a field derived using natural Neumann boundaries while ϕ is derived from either total Dirichlet boundaries or from a combination of Neumann and Dirichlet boundary conditions. (2–48) and (2–49) are the point forms for solving a new conductivity distribution.

The important advantage of this method is that it transfers the difference to the interior, rather than to the boundary as in the Newton–Raphson–like methods. This yields a sparse–matrix for using efficient finite element method schemes, such as the Point–Iterative Point–Accumulative method[33]. In addition, the conjugate gradient method used in this algorithm avoid solving large system matrices. Figure 2.4 shows the flow chart of the Wexler algorithm.

In the Kohn–Vogelius algorithm, the error term is given by

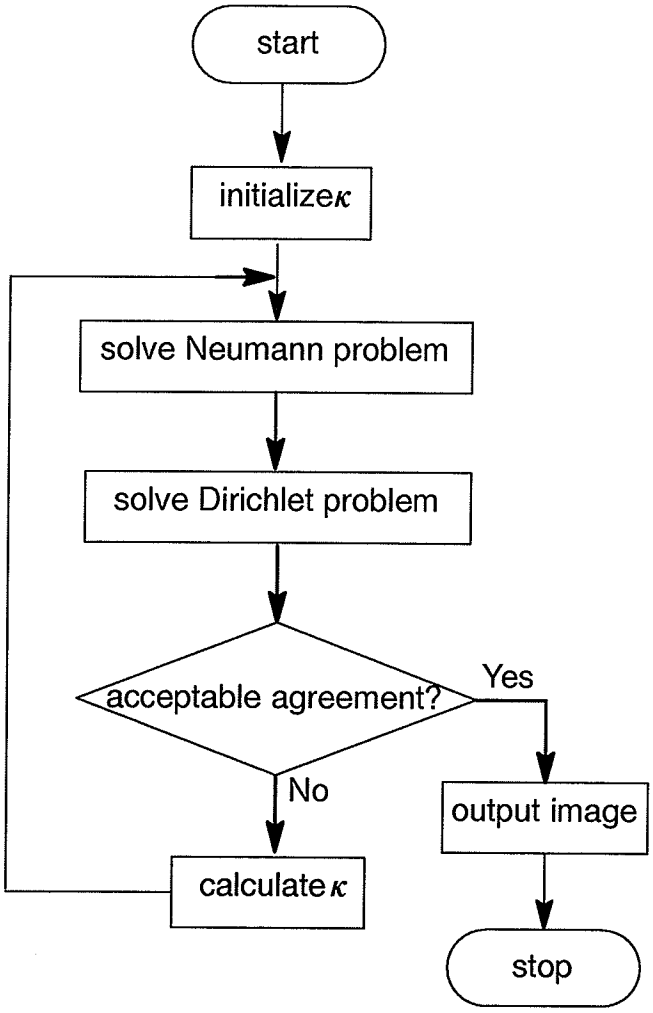

Figure 2.4 Flow chart of the Wexler and Kohn–Vogelius algorithm

$$\epsilon_{KV} = \sum_x \int_v (\kappa^{\frac{1}{2}}\mathbf{J}_i + \kappa^{\frac{1}{2}}\nabla\phi)^2 \, dv \tag{2–50}$$

The conductivity updating procedure is described as

$$\kappa_i^{n+1} = \left(\frac{\sum_x \int_v \mathbf{J}^2 \, dv}{\sum_x \int_v \nabla\phi\nabla\phi \, dv}\right)^{\frac{1}{2}} \tag{2–51}$$

Similarly as in the Wexler algorithm, the formula for updating element conductivity after an iteration step is derived as

$$\kappa_i^{n+1} = \left(\frac{\sum_x \sum_j \sum_l \sum_m W_{ijlm} \tilde{\phi}_l \phi_m}{\sum_x \sum_l \sum_m W_{lm} \phi_l \phi_m}\right)^{\frac{1}{2}} \kappa_j^n \qquad (2\text{–}52)$$

The algorithm iteratively refines the conductivity estimation until acceptable agreement is achieved. At that point, it is assumed that the correct conductivity is known.

2.2.2 Related imaging algorithms[4]

A variant of the Wexler and Kohn–Vogelius algorithms arises by considering the error term as

$$\epsilon_R(a) = \frac{1}{2} \sum_X \int_V (a_i^{\frac{1}{2}} \kappa^{\frac{-1}{2}} \mathbf{J}_i + a_i^{\frac{-1}{2}} \kappa^{\frac{1}{2}} \nabla \phi_{i)}^2 \, dv \qquad (2\text{–}53)$$

where $\mathbf{a}^T = (a_1, a_2, \ldots a_m)$ is an m–vector of constant a_i. The element conductivity updating formula is

$$\kappa_i^{j2} = \frac{\sum_X \int_{V_i} |J_i|^2 \, dv \int \kappa_j \, |\nabla \phi_i|^2 \, dv}{\sum_X \int_{V_i} |\nabla \phi_i|^2 \, dv \int \kappa^{-1} \, |J_i|^2 \, dv} \qquad (2\text{–}54)$$

The major difference between (2–54) and the Wexler and Kohn–Vogelius formula is that κ_i is only *defined implicitly* by (2–54), since the conductivity appears on the right hand side of the equation inside the integrals. Thus, it is an implicit formula for the updated conductivities.

2.3 Matrix inversion algorithms

2.3.1 The transfer impedance algorithm

Most of the previous discussions and comparisons on EICT algorithms leads to matrix inversion algorithms[46] as the next step. In 1985, Murai and Kagawa suggested a Newton–Raphson–like method for EICT, based on network sensitivity and transfer impedance theory[27]. Consider a domain V with conductivity $\kappa(x, y, z)$. The potential $\phi(x, y, z)$ in V is governed by the Laplace equation

$$-\nabla \cdot \kappa \nabla \phi = 0 \tag{2–55}$$

with the boundary condition

$$\kappa(s)\frac{\partial \phi}{\partial n} = \mathbf{J} \tag{2–56}$$

where $\mathbf{J}$ is an electrical current density prescribed at the surface. When the conductivity distribution changes from $\kappa(x,y,z)$ to $\kappa(x,y,z)+\Delta\kappa(x,y,z)$, the transfer impedance change ΔZ for the pair of current and voltage electrodes (A,B) and (C,D) (Figure 2.5) can be given as

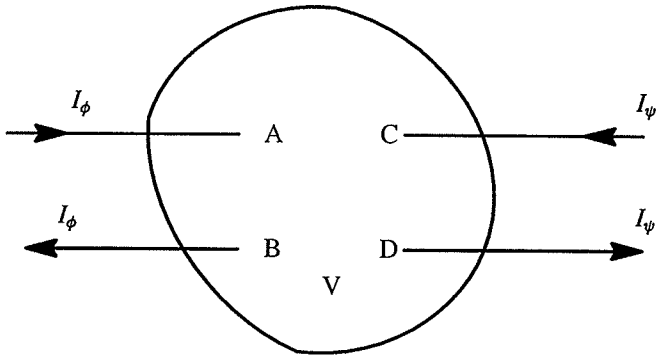

Figure 2.5 Problem description

$$\Delta Z = -\int_V \Delta\kappa \frac{\nabla\phi\ (\kappa)}{I_\phi} \cdot \frac{\nabla\psi\ (\kappa+\Delta\kappa)}{I_\phi} dV \tag{2–57}$$

The problem is to find the conductivity distribution $\kappa(x,y,z)+\Delta\kappa(x,y,z)$ from the measured potential distribution for the applied current distribution over the surface or from the measured impedance Z over the surface. The term $\nabla\psi(\kappa+\Delta\kappa)$ in (2–57) is then expanded with respect to $\Delta\kappa$ and the higher order terms are neglected. (2–57) can be expressed as

$$\Delta Z = -\int_V \Delta\kappa \frac{\nabla\phi\ (\kappa)}{I_\phi} \cdot \frac{\nabla\psi\ (\kappa)}{I_\phi} dV \tag{2–58}$$

Therefore, the iterative procedure is described as follows:

$$\Delta Z^{(n)} = Z^* - Z^{(n)} = -\int_V \Delta\kappa \frac{\nabla\phi\ (\kappa)}{I_\phi} \cdot \frac{\nabla\psi\ (\kappa)}{I_\phi} dV \tag{2–59}$$

where Z^* is the measured transfer impedance and $Z^{(n)}$ is the updated transfer impedance based

on the conductivity distribution $\kappa^{(n)}$ at the n–th iteration. $Z^{(n)}$ can be calculated as $Z^{(n)} = \phi_{CD}/I_\phi$ or $Z^{(n)} = \psi_{AB}/I_\psi$. If the conductivity is constant over each element, we have

$$\Delta Z^{(n)} = Z^* - Z^{(n)} = - \sum_j S_{ij} \Delta \kappa_j^{(n)} \tag{2–60}$$

where

$$S_{ij} = - \int_{V_j} \frac{\nabla \phi \ (\kappa)}{I_\phi} \cdot \frac{\nabla \psi \ (\kappa)}{I_\phi} dV_j \tag{2–61}$$

and it is evaluated by the finite element method.

The algorithm then can be described as follows:

Step (1) Assume an initial conductivity distribution;

Step (2) Calculate $\Delta Z_i^{(n)}$ for each electrode pair (A,B) and (C,D);

Step (3) Calculate the coefficient matrix and solve the small change of conductivity distribution;

Step (4) If the total conductivity change is smaller than a pre–set number, the convergence is achieved and the procedure stops; otherwise, a new conductivity distribution is assumed by $\kappa_j^{(n+1)} = \kappa_j^{(n)} + \Delta \kappa_j^{(n)}$ and then step (2) through step (4) are repeated.

2.3.2 The output least–squares algorithm

The transfer impedance algorithm proposed by Murai and Kagawa needs to calculate the entire finite element mesh with the standard Newton–Raphson method. In 1987, Yorkey, Webster and Tompkins[46] published a modified Newton–Raphson method with an output least–squared approach which tries to minimize the sum of the squares of the difference between measured and predicted data.

Then, errors to be minimized is the output error function. It is

$$\epsilon_Y(\kappa_i) = \frac{1}{2}(\mathbf{f} - \phi_o)^T(\mathbf{f} - \phi_o) \tag{2–62}$$

where ϕ_o is the measured voltage vector, and $\mathbf{f}$ is a function mapping a resistivity distribution r into a set of measured boundary voltages. To minimize (2–62), we differentiate

ϕ with respect to r and set the result equal to zero

$$\epsilon_Y' = [\mathbf{f}']^T[\mathbf{f} - \boldsymbol{\phi}_o] = 0 \qquad (2\text{–}63)$$

By expanding the left hand side of (2–63), and by keeping the linear terms and neglecting higher order terms, we have an approximate matrix form for updating conductivities

$$\Delta r^n = -[[\mathbf{f}'(r^n)]^T\mathbf{f}'(r^n)]^{-1}[\mathbf{f}'(r^n)][\mathbf{f}(r^n) - \boldsymbol{\phi}_o] \qquad (2\text{–}64)$$

(2–64) defines an iterative procedure to find the real resistivity distribution r*. At the n–th iteration, (2–64) is solved and new distribution is estimated by $r_j^{(n+1)} = r_j^{(n)} + \Delta r_j^{(n)}$.

The derivation of the above formulas is known as either the modified Newton–Raphson method, or the Gauss–Newton method. Its convergence performance is well known. When ϕ_o is formed in the presence of additive zero–mean independent noise, the method becomes the nonlinear least–squares estimation.

Similar to the algorithm of Murai and Kagawa, Yorkey's algorithm employs the Laplace equation to describe the resistivity distribution in continuous media and the FEM to calculate the surface potential distributions. To simplify Jacobian matrix computations, associated with the standard Newton–Raphson method, they derived a simple formula to form individual Jacobian matrix entries with network compensation theory[15]. The simulation results show that the algorithm possesses the convergence property of the Newton–Raphson method, but is quite sensitive to measurement noise[15].

2.4 Algorithm Comparisons

The major comparisons in other research work focused on the convergence rate of different algorithms[46]. There are other aspects, which affect the performance of an EICT algorithm, that ought to be thoroughly addressed. In general, error function minimization algorithms deal with sparse matrices and conductivity distribution is updated on a finite element basis; while matrix inversion algorithms generate dense Jacobian matrices and the conductivity distribution is updated according to boundary measurements directly. These important dif-

ferences were neglected in previous work when EICT algorithms are compared. When these factor are considered, convergence speed may not be the only dominant factor when an EICT algorithm is evaluated. The comparisons made in this chapter are brief reviews of previous work. Further investigations will be conducted later and characteristics of error function minimization algorithms will be discussed in Chapter 7 of this thesis.

2.4.1 Convergence speed

Previous comparisons between the two methods discussed above indicate that matrix inversion algorithms have faster convergence speed in terms of iterations[46]. If the norm of the error term is defined as

$$Error = \left(\frac{\sum_i | \kappa_{exact} - \kappa_{cal} |}{\sum_i | \kappa_{exact} |} \right) / M \qquad (2\text{–}47)$$

where M is the total number of elements, the convergence speeds of these two algorithms can be compared in Figure 2.6 (b) by plotting the errors for the example shown in Figure 2.6 (a). The cause of the slow convergence speed of the error function minimization algorithms

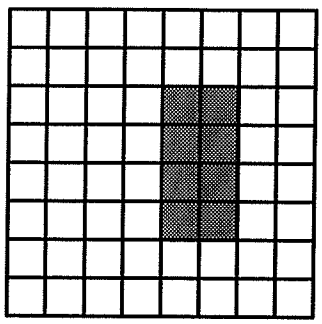

(a) Original image
Contrast: 1:3

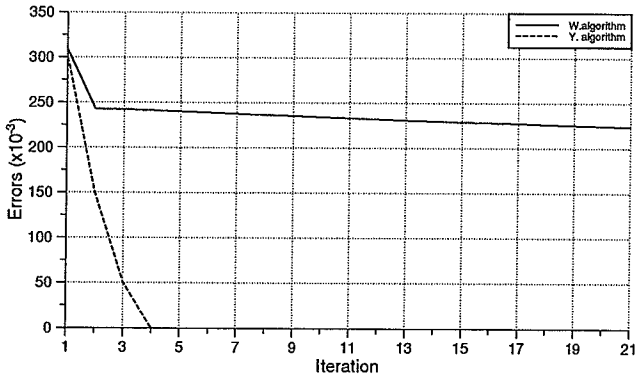

(b) Errors with different algorithms

Figure 2.6 Comparisons on convergence speed with different EICT algorithms

is due to the fact that these algorithms take the difference between Dirichlet and Neumann

boundary condition solutions as the driving force. The difference becomes smaller as the reconstructed image approaches to the true picture. In fact, only in the first iteration do the error function minimization algorithms give a significant improvement in element conductivity, as we can see from Figure 2.6 (b).

2.4.2 Potentials in large system applications

It has been pointed out that matrix inversion scheme results in dense matrix systems[41]. This can be a serious problem in three–dimensional imaging since the inversion of dense matrices results in longer computing times and larger storage space. The conductivity/resistivity updating procedures with evaluations of Jacobian matrix also require pre–setups.

In contrast to matrix inversion algorithms, error function minimization algorithms generate sparse matrices, such as the Wexler algorithm does, and the Point–Iterative and Point–Accumulative algorithm[9] can be used when Dirichlet and Neumann boundary conditions are solved using the FEM at each iteration. The element conductivity updating procedures are all on point forms, i.e. new estimation of conductivity distributions is calculated in scalar basis. Then, algorithms do not have difficulties in processing the large amount of data associated with a three–dimensional system.

2.4.3 Contact and spreading resistance effects

To eliminate contact resistance effects, error function minimization algorithms do not require the use of measured potentials at active current injection sites when the Dirichlet boundary condition problem is solved. Yorkey's algorithm, and similar ones, automatically exclude those potentials when the impedance at active ports are not used.

2.4.4 Algorithm stability and initial conductivity distribution assumption

The first guess for the conductivity distributions affects the final image qualities. The example in Figure 2.7 (a) were shown in Yorkey's work[46] as an example for which the Wexler algorithm did not converge. They suggested that the algorithm tried to image objects in the central areas. In this thesis, simulations with different initial guesses of the conductivity distribution were conducted. When the initial guess is chosen as 1.0 everywhere, error started

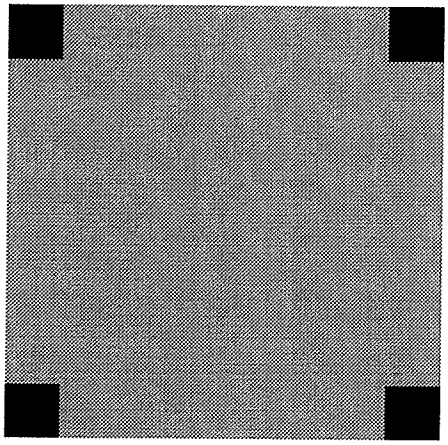

a. Original image
Contrast : 1:3

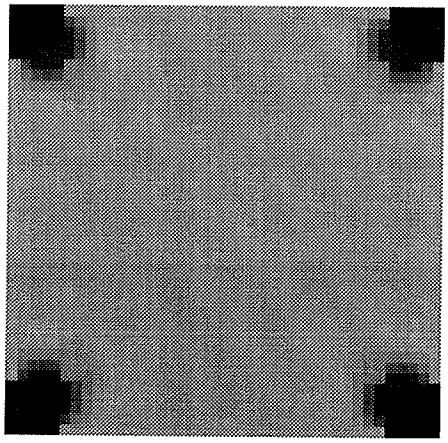

b. First guess = 3.0

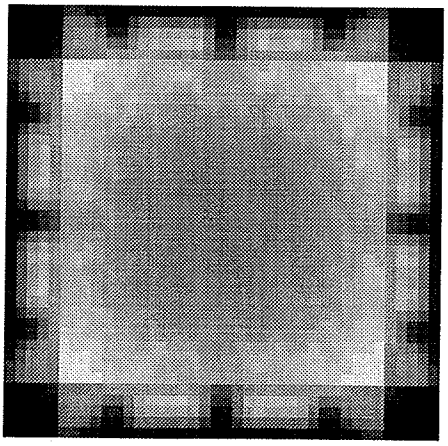

c. First guess = 1.0

Figure 2.7 Comparisons on algorithm stabilities with different initial guess distributions

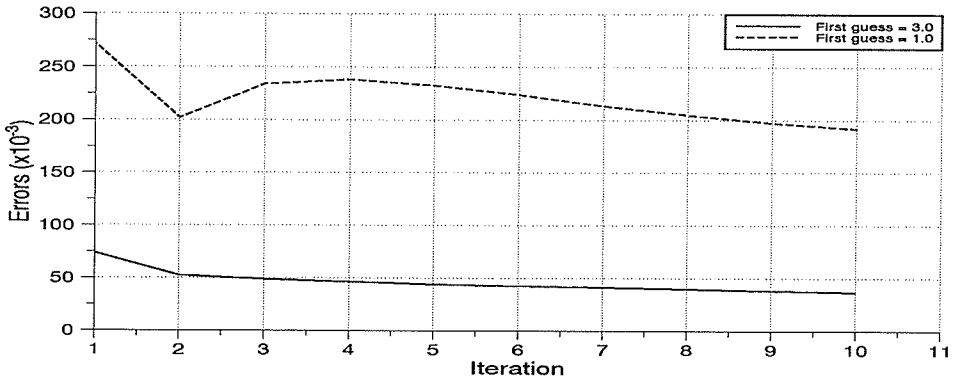

d. Errors with different initial guesses

Figure 2.7 Comparisons on algorithm stabilities with different initial guess distributions

increasing but went down again later (Figure 2.7 (c)). When the initial guess is 3.0, the algorithm converged smoothly (Figure 2.7 (b)). From this example, we can see that error function minimization algorithms do not have a bias to make conductivity distribution improvement only at the central part of a body. Therefore, Yorkey's conclusion appears to be incorrect.

CHAPTER 3

EICT FOR LUMPED NETWORKS

The numerical methods, such as the FEM, for the solution of fields introduce truncation (or discretization) error. In effect, the transformation of a continuum (e.g. field) representation introduces error that is incidental to the image recovery process. In order to demonstrate the imaging procedure, while excluding extraneous truncation error, we consider the inverse problem associated with a network formulation. In doing this, we will use a procedure, parallel to that of the continuum problem, in order to uncover all unknown conductance values. Definitions and terms used later in this thesis will be discussed first in this chapter. Then, a network model for the EICT algorithm is defined. The recovery capability of EICT systems, with error function minimization algorithms and excitation/measurement effects on image quality, are investigated using network methodology. Finally, the possibilities and corresponding schemes for optimal design of excitation patterns in a topological sense are presented.

3.1 Definitions and Terms

3.1.1 Excitation/measurement patterns

An *excitation pattern* in an EICT problem is a set of currents injected into and extracted from the body to be imaged.

A *measurement pattern* in an EICT problem is a set of measured potentials induced by one excitation pattern. The pattern using all measured boundary potentials (including active sites that include the effects of contact and spreading resistances) as a boundary condition for a Dirichlet boundary condition problem is called the *always* pattern; the pattern discarding the potentials at active excitation points but using those points when not active is called as the *sometimes* pattern; and the pattern without using the potentials at all excitation points

is called as the *never* pattern. Figure 3.1 shows two excitation patterns and their correspond-

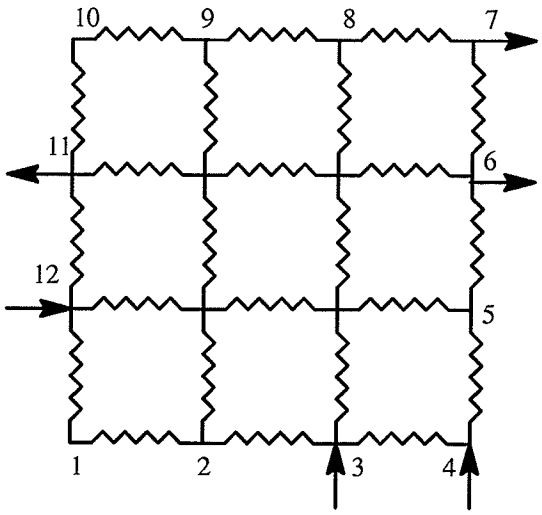

Figure 3.1 Excitation patterns and measurement patterns
Ma, Ms, and Mn are *always*, *sometimes*, and *never* patterns, respectively.

ing measurement patterns applied to a network with 12 available electrode positions.

An *always* pattern will be denoted as M_a, a *sometimes* pattern as M_s, and an *never* pattern as M_n to represent the three measurement patterns correspondingly in the rest of the thesis.

3.1.2 Determinacy of EICT

The *determinacy* of EICT is defined as the ratio of the number of the independent measurements to the number of unknowns.

3.1.3 Determining the maximal number of independent measurements

The number and the location of the electrodes used in each excitation pattern are important to the success of an EICT algorithm. The selections of the numbers and the positions of excitation patterns are a problem dependent and rely on experience[27] to certain extend.

Suppose there are N nodes as measurement nodes (i.e. electrode sites) in a network. When the N nodes are numbered as 1, 2, ..., N, an N–1 port network can be constructed by assigning node N as the reference node and forming port i with node i (i = 1, 2, ..., N–1) and node N, as shown in Figure 3.2 (a). If bipole excitations (each excitation pattern uses two nodes) are used, there are N–1 independent excitation patterns. Table 3.1 also shows the possible com-

Table 3.1
Possible excitation combinations

Injection node	Extraction node
1	2, 3, ..., N–1, N
2	3, 4, ..., N–1, N
⋮	⋮
N–2	N–1, N
N–1	N

binations of injection and extraction nodes. The total number of possible excitation pairs can be calculated as

$$E_p = (N-1+1)(N-1)/2 = N(N-1)/2 \tag{3–1}$$

For each excitation pattern, N–1 independent voltages can be measured. Then, the total possible number of voltage measurements will be

$$M_p = (N-1)E_p = (N-1)N(N-1)/2 \tag{3–2}$$

which is the possible number of measurements an EICT system can provide. Consider the reciprocity and the superimposition of a linear passive multi–port network, there are approximately $N^2/2$ linearly independent measurements that can be used to reconstruct a network[7], if *always* or *sometimes* patterns are used. Table 3.2 shows the total number of independent measurement combinations when the N–port network is constructed in the way we described above. For *always pattern,* we have

$$M_a = N(N-1)/2 \tag{3–3}$$

For *sometimes* patterns

$$M_s = (N-1)(N-2)/2 \tag{3–4}$$

and for *never* patterns

Table 3.2

Total independent measurement combinations

Always patterns		Sometimes patterns	
Excitation node pair	Measurement node pair	Excitation node pair	Measurement node pair
1, N	(1, N), (2,N), ..., (N–1, N)	1, N	(2, N), (3,N), ..., (N–1, N)
2, N	(2, N), (3,N), ..., (N–1, N)	2, N	(3, N), (4,N), ..., (N–1, N)
⋮	⋮	⋮	⋮
N–2, N	(N–2, N), (N–1, N)	N–2, N	(N–1, N)
N–1, N	(N–1, N)	N–1, N	

$$M_n = (N - 1 - 2E_n)E_n \qquad (3\text{–}5)$$

where E_n ($E_n < N-1$) is the number of excitation pairs. It should be noticed that when N–1 excitations are used, M_n is zero.

For any $K < N$ ($K > 0$), the combinations are shown in Table 3.3. The available number

Table 3.3

Measurements with K independent excitation patterns

Always patterns		Sometimes patterns	
Excitation node pair	Measurement node pair	Excitation node pair	Measurement node pair
1, N	(1, N), (2,N), ..., (N–1, N)	1, N	(2, N), (3,N), ..., (N–1, N)
2, N	(2, N), (3,N), ..., (N–1, N)	2, N	(3, N), (4,N), ..., (N–1, N)
⋮	⋮	⋮	⋮
K, N	(K, N), ... (N–1,N)	K, N	(K+1, N), ...(N–1, N)

of independent measurements for the *sometimes* patterns is

$$M_s = \frac{K}{2}(N-2+N-1-K) = \frac{K}{2}(2N-K-3) \qquad (3\text{–}5)$$

It should be pointed out that this number is the maximum that K excitation patterns can provide. If the selection of the reference node changes, M_s could be smaller.

3.1.4 Over–determined and under–determined problems

Assume C to be the number of unknown elements, and M_m belongs to { M_a, M_s, M_n }. If we use D as the determinacy, the problem with the determinacy $D = M_m / C$ greater than 1 is *over–determined*, and the problem with the determinacy $D = M_m / C$ less than 1 is *under–determined*.

3.2 Multi–Port Resistive Network Recovery With EICT Algorithms

3.2.1 Multi–port resistive network as the discretized model to study EICT imaging

There are many possible reasons causing an EICT algorithm to fail in reconstruction of a target image. It is very difficult to isolate specific causes of a such failure when an electric field problem is solved, since numerical methods used to solve the field potentials introduce errors to the imaging procedure as well. For this reason, the network analogy helps to isolate the issues because it is somewhat simpler. We can derive the network recovery formulas in a similar manner.

Consider the multi–port resistive network shown in Figure 3.2. The nodal equation system, with the port current injections as shown, is

$$\mathbf{YV} = \mathbf{J} \qquad (3\text{–}6)$$

where **Y** is the nodal admittance matrix, **V** is the vector of unknown node potentials and **J** is the current source vector. It should be noticed that port currents are applied at a subset of boundary nodes in the network. If port voltages (i.e. node potentials at boundaries) are applied, (3–6) becomes

$$\mathbf{YV} = 0 \qquad (3\text{–}7)$$

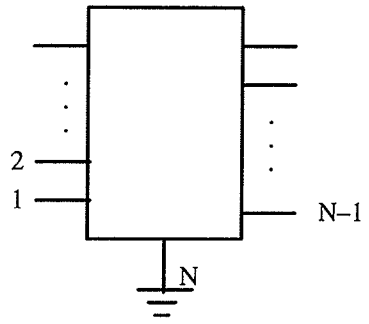

(a) N–1 independent ports of an N–terminal network

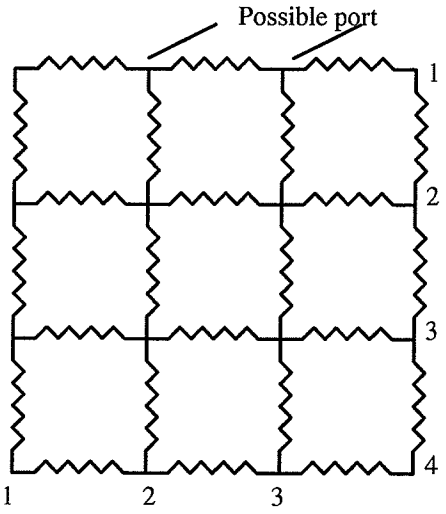

(b) A resistive network model

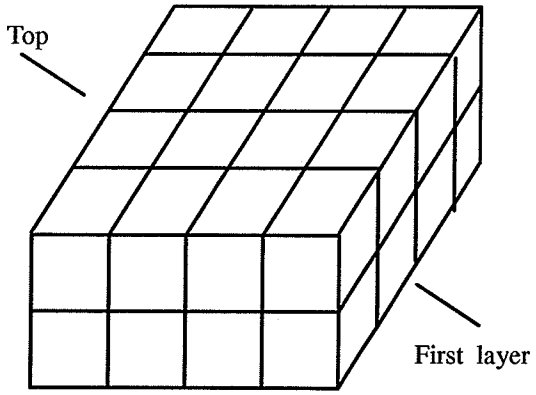

(c) A resistive network model for three–dimensional imaging, each branch containing a conductor

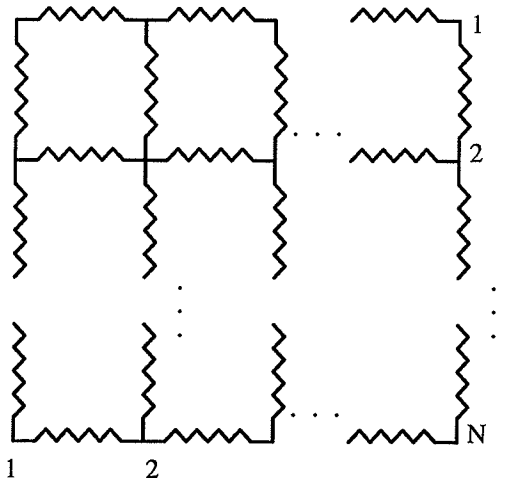

(d) A multi–port resistive network with N nodes on each sides

Figure 3.2 Resistive network models of EICT

V here consists of both known and unknown node potentials.

The problem is to find the branch conductances by applying port currents and measuring port voltages. First, an initial guess at all branch conductances has to be imposed. When a port current is applied, all port voltages can be measured. For each branch from node i to node j (i, j = 1, 2, ...), Ohm's law can be written as

$$g_{ij}(v_i - v_j) = j_{ij} \tag{3–8}$$

where g_{ij} is the branch conductance, v_i and v_j are node voltages of the branch, and j_{ij} is the branch current. For all port excitations, the least–squares residual form is

$$r = \sum_x \sum_{b_{ij}} [g_{ij}(v_i - v_j) - j_{ij}]^2 \tag{3–9}$$

which can be minimized by taking the derivative with respect to branch conductance and setting it to zero

$$\frac{\partial r}{\partial g_{ij}}|_{b_{ij}} = \sum_x 2[g_{ij}(v_i - v_j) - j_{ij}](v_i - v_j) = 0 \tag{3–10}$$

so,

$$\sum_x g_{ij}(v_i - v_j)^2 = \sum_x j_{ij}(v_i - v_j) \tag{3–11}$$

The unknown branch conductance can then be solved by

$$g_{ij} = \frac{\sum_X j_{ij}(v_i - v_j)}{\sum_X (v_i - v_j)^2} \tag{3–12}$$

The branch current is unknown and has to be estimated in advance before (3–12) is employed. It can be obtained by (3–6) with the assumed branch conductances. (3–12) then becomes

$$g_{ij} = \frac{\sum_X (\tilde{v}_i - \tilde{v}_j)\tilde{g}_{ij}(v_i - v_j)}{\sum_X (v_i - v_j)^2} \tag{3–13}$$

where v_i and v_j are derived from an assumed set of network conductance values, $\tilde{g}_{ij}$, under an applied boundary voltage; while $\tilde{v}_i$ and $\tilde{v}_j$ are based on the same network under an applied boundary current.

The procedure described above is based on the Wexler algorithm in a network recovery. Table 3.4 shows the system equation similarities between the conductivity distribution imaging and the branch conductance recovery with this algorithm. It demonstrates that branch

Table 3.4

Comparisons of EICT algorithms between the field case and the network case

	Field case	Network case
System Equation	$S\phi = \underline{b}$	$YV = J$
N. B.C.*	$-\nabla\cdot\kappa\nabla\phi = f \qquad \kappa(s)\frac{\partial\phi}{\partial n} = h(s)$	$YV = J$
D.B.C.*	$-\nabla\cdot\kappa\nabla\phi = f \quad \phi(s) = g(s)$	$YV = 0$
Ohm's law	$J = \kappa\nabla\phi$	$J_{ij} = g_{ij}(v_i - v_j)$
Updating Equations	$\kappa_i = -\frac{\sum_X \int_{v_i} J\cdot\nabla\phi \, dv}{\sum_X \int_{v_i} \nabla\phi\cdot\nabla\phi \, dv}$	$g_{ij} = \frac{\sum_X j_{ij}(v_i - v_j)}{\sum_X (v_i - v_j)^2}$
	$\kappa_i = \left(\frac{\sum_X \int_{v_i} J^2 \, dv}{\sum_X \int_{v_i} \nabla\phi\cdot\nabla\phi \, dv}\right)^{1/2}$	$g_{ij} = \left(\frac{\sum_X j^2}{\sum_X (v_i - v_j)^2}\right)^{1/2}$
Error Norms	$e = \frac{\sum_l (\kappa_e - \kappa_c)^2}{\sum_l \kappa_e^2}$	$e = \frac{\sum_l (g_e - g_c)^2}{\sum_l g_e^2}$

*N.B.C. and D.B.C. represent the Neumann and the Dirichlet boundary conditions, respectively

conductance identification of a linear multi–port resistive network with unknown lumped elements, as shown in Figure 3.2(d), is a parallel procedure to the finite element conductivity recovery. A multi–port resistive network can, therefore, be taken as a discretized model to study EICT imaging problems. To apply an EICT algorithm to the network recovery problem, the structure of the network should be pre–specified. Then, all the branch conductances will be recovered after an initial guess of branch conductances is assigned to each branch. The specification of the equivalent network structure here is the correspondent procedure of designing a finite element mesh in conductivity distribution imaging. By performing an error function minimization algorithm in a network recovery problem, the effects of trunca-

tion errors associated with the field analysis do not exist, since the recovery procedure is not contaminated by discretization.

3.2.2 Network models and their recoveries in simulation

Figure 3.3 shows a resistive network and the recovered one after 500 iterations with 6 speci-

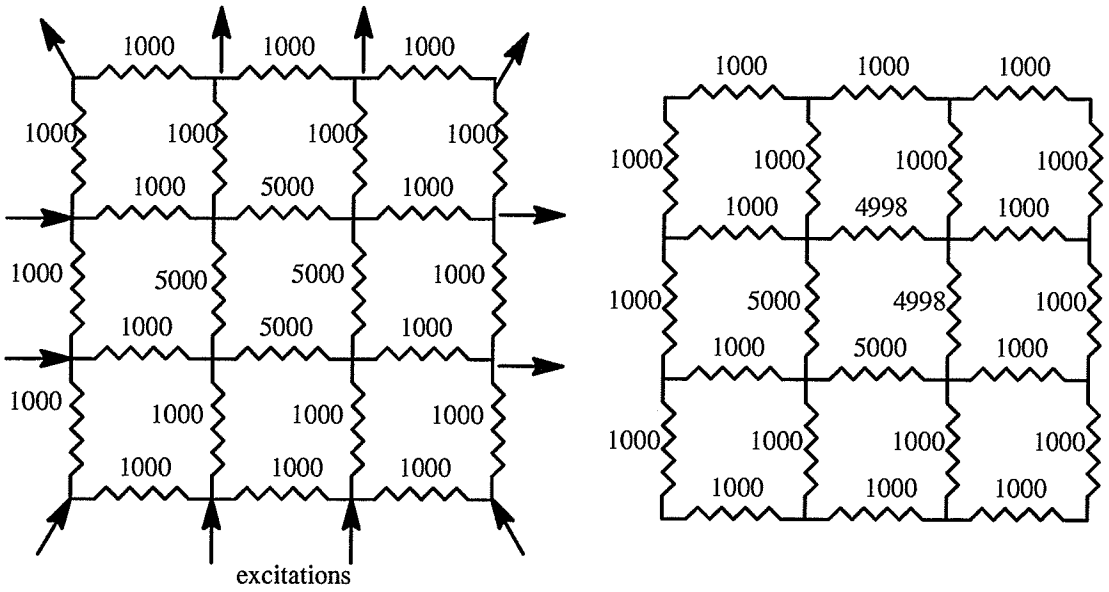

a. Original network with 6 excitation patterns

b. Recovered network after 500 iterations with the Wexler algorithm

Figure 3.3 A network recovery example with EICT method

fied excitation patterns using the Wexler algorithm. There are 24 unknown branch conductances, 12 available voltage measurement nodes (i.e. 12 electrodes can be placed at those port terminals) in the network. The number of independent ports of the network is 11. Therefore, for *always* patterns, the maximum number of independent measurements is $12 \times 11/2 = 66$; for *sometimes* patterns, it is $11 \times 10/2 = 55$. The smallest number of excitations needed to reconstruct this network as an over–determined problem can also be calculated by $E_{min,s}(2 \times 12 - 3 - E_{min,s})/2 \geq 24$ for *sometimes* patterns, which is approximately 3. When 6 excitations are used, K = 6, so $M_s = 6(2 \times 12 - 6 - 3)/2 = 45$ and the determinacy is slightly less than 2. When the excitation patterns used are less than the maximal number of independent excitations, the use of *never* patterns is possible.

If we add more layers with the same configuration to the network, as shown in Figure 3.2(c),

an EICT three–dimensional network model can be built up.

The recovery of a multi–port resistive network shows the problem with the Wexler algorithm in a similar manner: slow speed of convergence in terms of the number of iterations. It also shows that the algorithm converges perfectly to the original network values although many iterations are needed, which verifies the argument of the use of networks to simplify the studies on EICT systems and algorithms.

3.3 Discussing Excitation Pattern Effects on Network Recovery

3.3.1 Recovering capabilities of EICT systems

According to what we have previously calculated, always patterns or sometimes patterns give approximately $N^2/2$ independent voltage measurements for N electrodes if the maximal number of independent excitation patterns are applied. At most $N^2/2$ unknown branch conductances can be recovered with an EICT algorithm. This gives plenty of data to use the least–squares technique to obtain unique solutions[27] and also indicates recovering potentials offered by an EICT system. Determinacy describes such potentials. The question is whether the determinacy is the only factor which determines the recovering capability when a network with C unknown branch conductances is given; or whether an EICT algorithm can recover a network accurately as long as $N^2 / 2 > C$.

Over–determined problems The determinacy here is greater than 1. Figure 3.4 shows two recovered networks with different excitation patterns applied to the same example in Figure 3.3 (a). As the determinacy decreases, the computing time increases. The results indicate that the more excitations used, the fewer the number of iterations required. However, the computing time will increase dramatically as the number of excitation patterns goes up since the forward problem (evaluating the node potentials with updated branch conductances) in an EICT algorithm has to be solved twice for each excitation pattern at every iteration. (See the flow chart in Chapter 2.) In practice, it takes time to make a set of measurements for each excitation pattern. When more excitation patterns are needed, it is difficult to keep the mea-

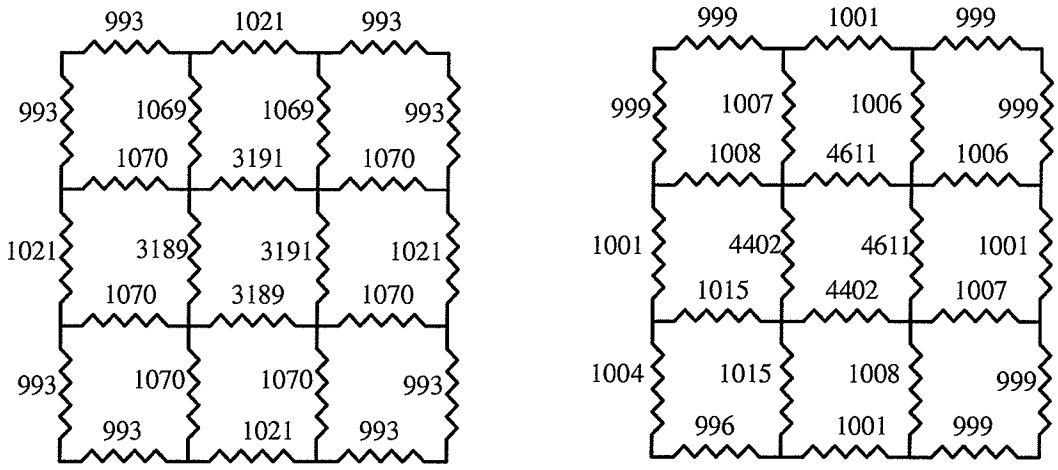

a. 4 excitation patterns after 50 iterations

b. 6 excitation patterns after 50 iterations

Figure 3.4 Number of excitation patterns effects on speed of convergence

surement conditions unchanged, especially in a medical case. The trade–off between the speed of convergence and the number of excitation patterns raises the questions that whether the maximal number of excitation patterns are needed when $C < N^2/2$, and that under what conditions, fewer excitations may be used to reconstruct a network without losing accuracy. If we apply the same number of excitation patterns to the same problem shown in Figure 3.4 again, but all patterns are put on the one side of the network, the whole network cannot be recovered even if the determinacy is kept same as 2. It shows that the positions of excitation patterns are important to the success of EICT algorithms.

Under–determined problems When determinacy is less than 1, the problem becomes under–determined. It has been pointed out that the number of data needed to recover a network with N branches has to be greater than N when matrix inversion algorithms are used[27]. There is no discussion on the issue of under–determined problems in previous work. What we want to see here is whether the error function minimization algorithms behave the same way as the matrix inversion algorithms do. The practical significance of studying the recovering capability in an under–determined problem is that the number or the positions of applicable electrodes might be limited in an EICT system, while the objects to be imaged in a body is relatively small so that finer network with more branches is needed. Therefore, more un-

knowns in a well designed model have to be solved using the EICT system; or that not the complete set of measurement potentials can be used in order to eliminate contact resistance effects.

This problem can be discussed with the network model for three–dimensional imaging. Using the configuration shown in Figure 3.2 (b), an example can be constructed as shown in Figure 3.5. There are top, first and second layers in the network. There are total $24 \times 3 + 16 \times 2 = 104$ unknown branch conductances. Electrodes are all positioned at the top. The 6 excitation patterns as shown in Figure 3.3 (a) with *sometimes* measurement patterns give $6(2 \times 16 - 6 - 3)/2 = 69$ independent measurements.

There are two aspects we can see from this under–determined example. First, the algorithm manages to recover the top and first layer of the network, although there are serious errors at the bottom. This suggests that part of the network can be recovered with higher accuracy in an under–determined problem if such parts are close to the area where the excitation/measurement patterns are arranged, while the entire network is left un–recovered. Second, the total error tends to decrease in the first few iterations, which indicates that a recovered network with lower accuracy can possibly be found in an under–determined problem.

The example reveals an important feature of error function minimization algorithms: they can recover a sub–network in an under–determined problem but leave the rest of the network untouched. It is worth discussing such a feature of the algorithms because, in practical EICT imaging systems, the conductivity distribution can only be represented exactly by an "infinitely fine mesh" which results in most of the problems being under–determined. As a result, when the number and position of electrodes are restricted, the finite excitations and measurements, with error function minimization algorithms, can produce part of the solution which may give enough information for the areas of interest, i.e. focus the total number of excitations/measurements to image the specified areas.

This example shows again that the recovery capability of EICT algorithms in an under–determined problem depends upon the location of the excitation patterns. The question is how

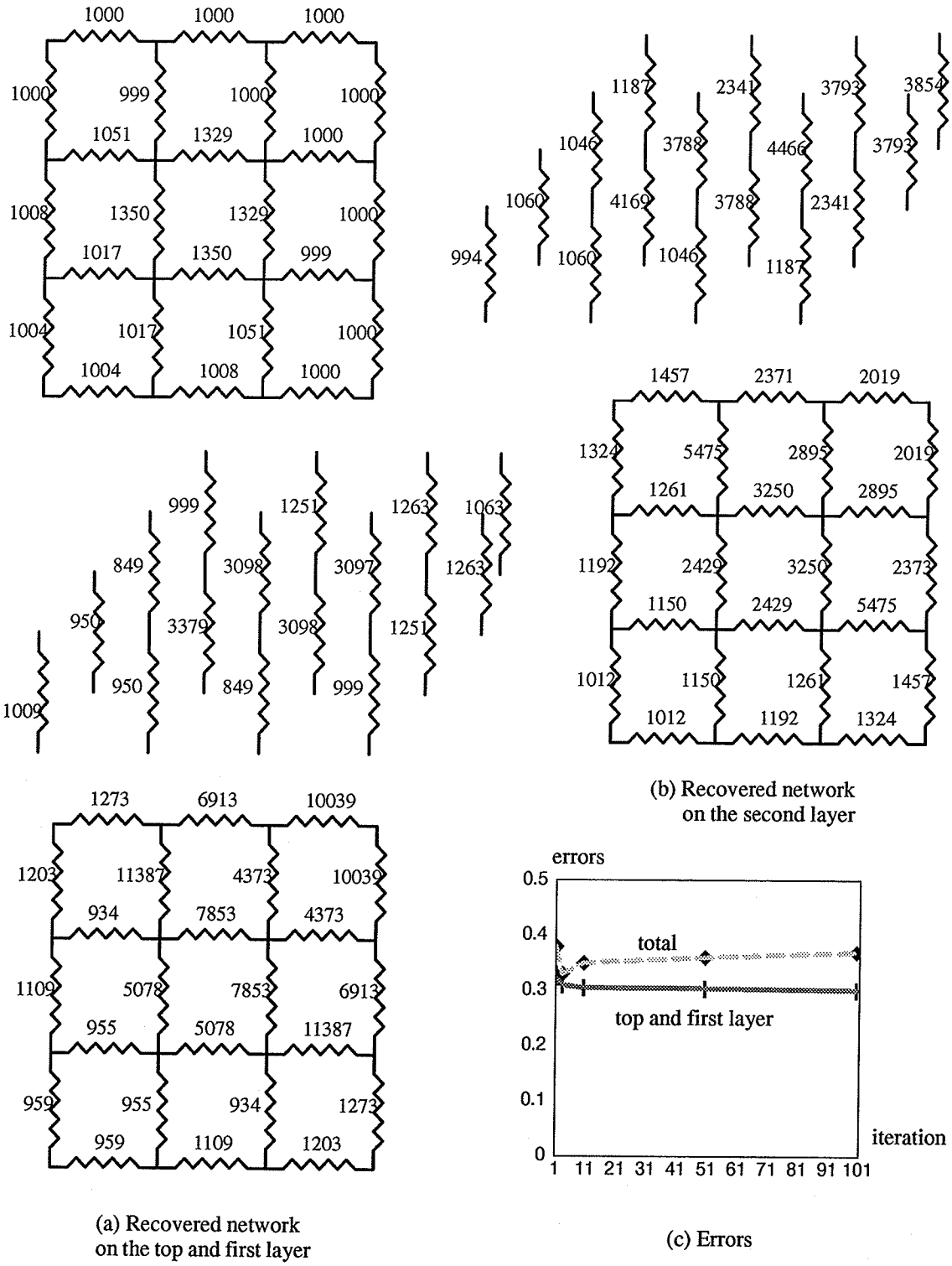

(a) Recovered network on the top and first layer

(b) Recovered network on the second layer

(c) Errors

Figure 3.5 An example of under–determined problem; iteration = 100

the maximal number of independent excitation patterns is arranged.

Measurement pattern effects The measurement pattern effects are mainly on the determinacy and the contact resistances. Sometimes patterns slightly reduces the number of independent measurements if bipolar excitations are used, and *never* patterns can cause an EICT problem to become under–determined when large number of excitations is used. Figure 3.6

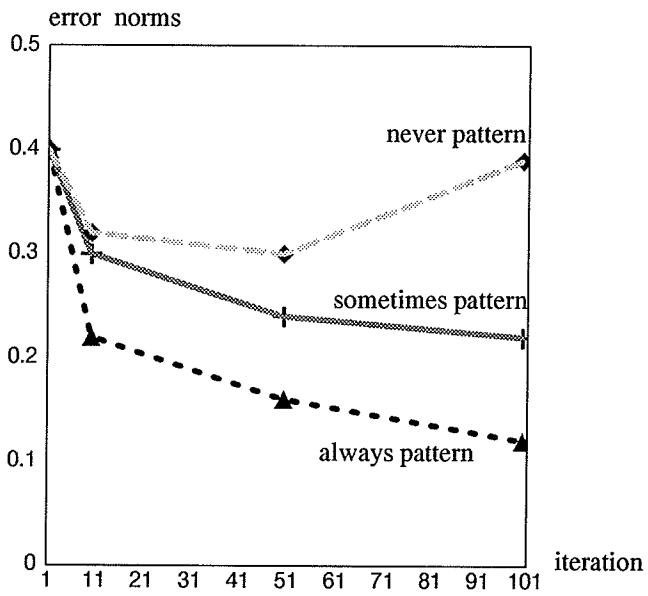

Figure 3.6 Comparisons on recovering errors with different measurement patterns

shows the comparisons on speeds of convergence with different measurement patterns under the same excitation patterns as in the example in Figure 3.3(a).

The relative positions between excitation and measurement sites affect the quality of recovered network as well. Take the example in Figure 3.5. If more layers is added to the network, Figure 3.7 shows errors in each layer. If the measurements are placed on the bottom layer (layer 6), the error plots does not change much, which indicates that such measurements are redundant although it contributes to the increase of the determinacy; but if measurements are placed on the side of the second layer, the recovered network has better quality, which shows the effectiveness of higher determinacy.

To eliminate the contact resistance problem, *sometimes* patterns are the better choice for an EICT problem since such patterns give almost the same number of maximal independent

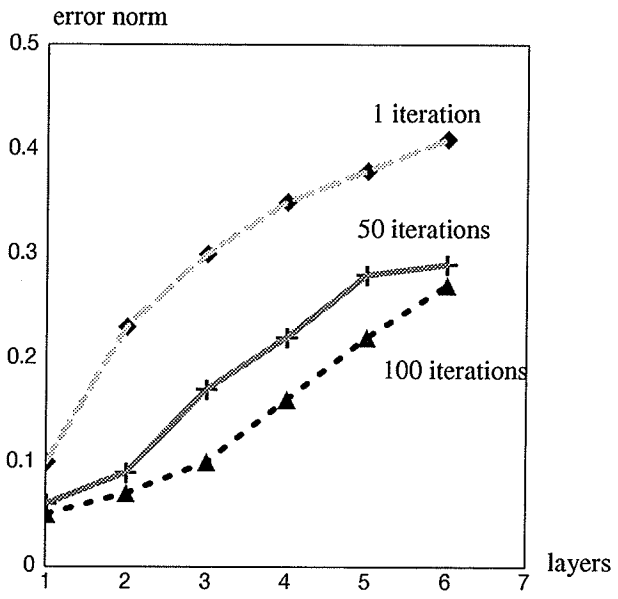

Figure 3.7 Errors for different layers in a 6 x 6 x 6 network
determinacy = 2 top excitations/measurements

measurements as *always* patterns do.

3.3.2 Sensitivity analysis of EICT

Measured potentials from each pair of injection and extraction electrodes represent a "view" in a particular "angle" to the network. The position of an excitation pattern decides the part of the region that can be "seen". Since the number of measured potentials provided by each excitation pattern is fixed, the number of excitation patterns results in over–determined or under–determined problems, and the positions of excitation patterns decide if they are effective to all port measurements.

From the previous examples, we have seen that under the same determinacy, different combinations of excitation patterns give images with varying qualities. For each excitation pattern, the measurements should only be taken from the positions where the information provided by the excitation pattern can be "felt". On the other hand, when the total excitations are not well arranged to make all measurements sensitive, the network may not be recovered properly even if the determinacy is greater than1. It suggests that after the number and posi-

tions of electrodes are decided in an EICT system, the arrangement of excitation patterns should cover two aspects: (a) make the problem over–determined; and (b) make each port measurement sensitive to at least one of the excitations.

If the first condition cannot be satisfied, the total excitation patterns have to be able to provide a sub–region where the network can be recovered reliably, i.e. to make the problem over–determined in the sub–region. Sensitivity analysis can help to decide such regions.

Sensitivity analysis relates to one of the important issues in an inverse problem, which is how much changes of internal parameters (branch conductances) of a network can be measured at ports of a network using devices with finite precision. These changes decide how much detail can be recovered in a reconstructed network. This problem depends upon the parameters and structures of the network to be recovered. For the example in Figure 3.8, the mea-

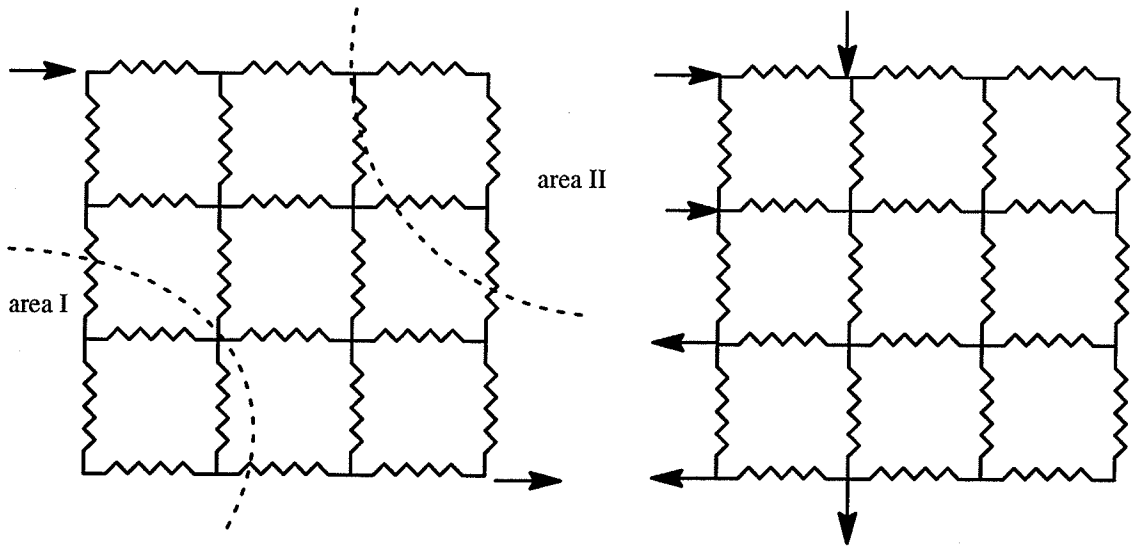

(a) Example 1 (b) Example 2

Figure 3.8 Examples of measurement sensitivity

surements made in area I may not reflect any change induced by the branch conductances in area II, or vise versa. While in the case shown in Figure 3.8 (b), it may not be possible to recover a network at all with the excitations arranged on one side of the network even if the determinacy is higher than 1, but the network could be recovered if other excitation/measurement arrangements with even lower determinacy.

Strictly speaking, sensitivity analysis is performed in a network with known parameters. However, the parameters of a network is the solution in EICT problems. What will be shown later is how sensitivity analysis can be used to determine a reliable region in EICT problems.

Definition of relative sensitivity Consider a network function T(N)[7]. The relative sensitivity, or simply the sensitivity, of T with respect to a parameter x in the network is defined as

$$S_T^x = \frac{\partial T}{\partial x}\frac{x}{T} \tag{3–14}$$

For the multi–port resistive network discussed here, the network function T is the transfer impedance Zij, which represents the ratio of the voltage at port j induced by the current at port i (i,j = 1, 2, ...), i.e.

$$T_{ij} = \frac{V_j}{I_i} \tag{3–15}$$

If the excitation current at port i is unchanged but a voltage change at port j is measured due to the parameter changes inside the network,

$$\Delta T = \frac{\Delta V_j}{I_i} = \Delta V_j \tag{3–16}$$

when $I_i = 1A$ at all ports. Then, the total change of port voltage induced by all possible changes of branch conductances is

$$\Delta V_j = \frac{\partial T}{\partial g_1}\Delta g_1 + \frac{\partial T}{\partial g_2}\Delta g_2 + \ldots + \frac{\partial T}{\partial g_n}\Delta g_n = \sum_i \frac{\partial V}{\partial g_i}\Delta g_i \tag{3–17}$$

where g_i is branch conductance. If we only give branch k a disturbance Δg_k, then

$$\Delta V_j = \frac{\partial T}{\partial g_k}\Delta g_k \tag{3–18}$$

If the precision of the voltage measurement is δ,

$$\Delta V_j = \frac{\partial T}{\partial g_k}\Delta g_k \geq \delta \tag{3–19}$$

has to be satisfied for a single branch conductance if the conductivity change is expected to

be measured. (3–19) also gives a way to estimate the relative sensitivity for each individual branch under a particular excitation pair, i.e.

$$\frac{\partial T}{\partial g_k} = \frac{\Delta V_j}{\Delta g_k} \tag{3–20}$$

Incremental network method in sensitivity calculation Sensitivities of the network parameters to a specified network function can be found by the incremental network approach[7]. Following the rules to construct an incremental network[7], we can obtain the corresponding incremental network for the network model of Figure 3.8 (b), as shown in Figure 3.9 . The analysis result of the incremental network can be used to determine the partial

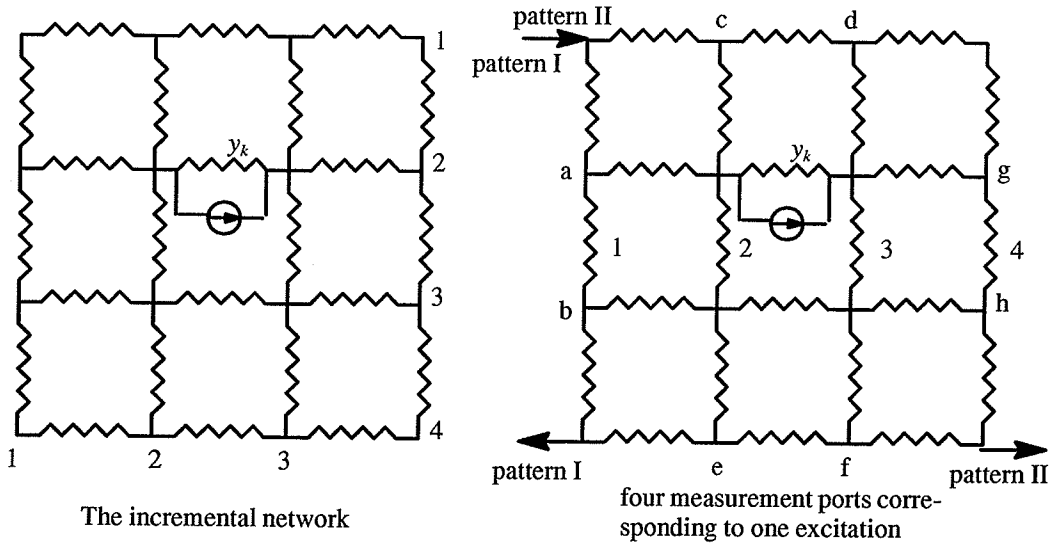

Figure 3.9 Construction of incremental network

derivatives.

When the background conductances and the structure of the network are known, partial derivatives of each branch conductance at every port under a particular excitation pattern can be simulated by giving branch conductance a small displacement.

Determination of excitation patterns with sensitivity theory With the approaches above, one can find the regions where sensitivities are higher than a threshold. The significance of knowing this can be addressed as follows:

(a) For a particular excitation pattern, how many branches can be affected by the injected

current; and

(b) For a network with fixed topological structure, design the excitation/measurement patterns to make most of the branches sensitive to at least one pair of port measurements. Assume the minimal measurable voltage change at a port is δ. It could be induced by a single branch close to the port, or by a group of branches far from the port. Only the region where the result is reliable to a specific excitation pattern can be determined. Figure 3.10

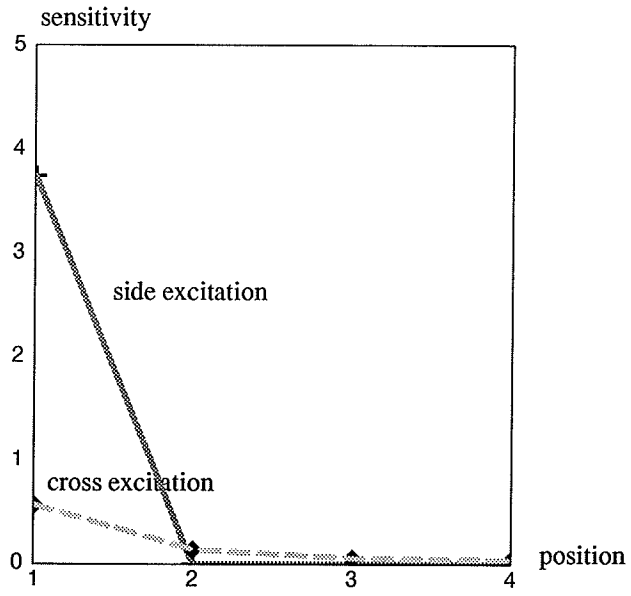

Figure 3.10 Sensitivities for branch 1 to 4 under 2 excitations

shows the sensitivity changes at the port a and b with branch 1 to 4 under the excitation pattern I (side excitation) and the pattern II (cross excitation). The sensitivities decrease rapidly as the position of a single branch goes away from the measurement port for side excitation; while for cross excitation, the change is less steep. It suggests that the cross excitation tends to reveal more information in the central part of the network.

To check if all excitations selected are effective, one can calculate the weakest sensitivity of the network for all excitations. They should make the weakest sensitivity felt by measurement, i.e.

$$\Delta V_j = \Delta y_i \sum_x \frac{\partial T}{\partial y_i} \geq \delta \qquad (3\text{–}21)$$

The entire region where port measurements are sensitive to the branch changes for this example is shown in Figure 3.11. This is the largest region that side excitation patterns can pro-

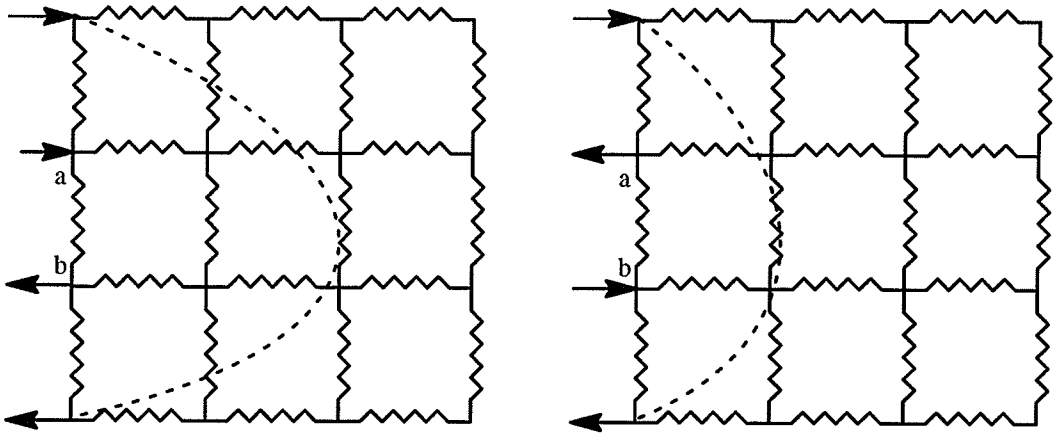

Figure 3.11 Reliable region with side excitations

vide. This diagram explains why only the top two layers can be recovered with reasonable accuracy in the three–dimensional network model example. Interpreting of the above diagram can be explained as that if there is only one branch conductance which is different from the rest of branches with one unit, the furthest branch value can be "felt" by the one measurement. This is corresponding to the weakest sensitivity of the network for all excitation patterns which determine the limit of one design of the excitation patterns.

We can draw some preliminary conclusions from the sensitivity analysis in EICT problems.

1. Determinacy is not the only factor which determines the recovery capability of an EICT system. The reliable region produced by the arrangements of excitation patterns is more important.

2. The maximal number of recoverable branches depend on the positions of excitation patterns, which can be designed with sensitivity analysis. The patterns, using the electrodes close to each other, recover branches near to ports, while patterns using more separated elec-

trodes reflect more information away from the measurement ports.

3. In an under–determined problem, a sub–network can be reconstructed if all excitations are arranged to generate a reliable region.

4. Not all the excitations are needed for all EICT problems. The patterns only reflecting information on the branches close to ports may generate redundant measurements. The patterns whose effective regions are covered by others can be thrown away.

5. Although fewer excitation patterns may slow down the speed of convergence, it may still save computing time in an imaging procedure, specially if we consider the large time consumed for every excitation in the forward problem at each iteration.

3.3.3 Accessibility of EICT

In the sensitivity discussions, we have shown that it is possible to arrange excitation patterns with a pre–designed network. In this section, an alternative approach with graph theory is shown to achieve the similar result.

From the previous examples, we know that the determinacy is not the only factor controlling convergence speed and image quality. As a solvability problem, the network parameter recovery is not only determined by possible measurements applied to a network, but also by its topological structure. To describe the topological solvable feature, we now introduce the *accessibility* to the EICT in network recovery. First, we define that a node of a network is called *accessible* if that node can be taken as a measuring point.

Theorem 1 Let g_0 be a conductance between two nodes 1 and 2 in a network N. Suppose that certain nodes in N are accessible and certain others are not. The cut sets of 1 or 2 not including any accessible nodes of N do not exist. Then measurement of g_0 is possible if and only if all paths (except the g_0 branch) from 1 to 2 contains at least one accessible node in N[7].

Figure 3.12 shows an example of this theorem. It is clear from the theorem 1 that there is a minimal number of nodes needed to make one branch measurable. Mayeda etc. [21] gave two algorithms (we call them component accessible algorithms) to find such nodes. The fun-

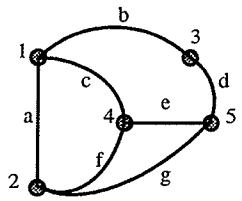

All paths	Cover nodes
(c,f)	4
(b,d,g)	4 5
(c,e,g)	3 5
(b,d,e,f)	3 4 5

If a is accessible, the nodes (4,3) or (4,5) have to be accessible

Figure 3.12 Example of accessibility theorem

damental concept of these algorithms is to find a set of nodes such that, to each path including a particular branch, there is at least one node in this set belonging to the path. The example in Figure 3.12 gives the minimal number of nodes which is needed to determine the branch a.

An algorithm to select the minimal number of nodes for the certain measurements to access all branches in a network can be described as follows:

Algorithm 1

Step 1 Set an incremental node set A;

Step 2 Select a tree T in the network N;

Step 3 Select a branch and record its two connecting nodes i and j;

Step 4 Find a new set B, which contains the minimal number of accessible nodes for i and j using a component accessible algorithm;

Step 5 Perform A = A **U** B (OR operation);

Step 6 Repeat Step 3 to 5 till all the branches of N have been examined. Then, set A contains the minimal number of accessible nodes of N for all branches.

If a set of accessible nodes are already known, the following algorithm can examine if all the branches in the network are measurable.

Algorithm 2

Step 1 Set the known accessible node set N_a;

Step 2 Examine every branch in the network N to get its minimal number of accessible node set N_b using a component accessible algorithm;

Step 3 If the branch examined is measurable, save it in set B_m; otherwise, save it in set B_u;

Step 4 Repeat Step 2 and 3 till all the branches of N have been examined;

Step 5 If B_u is empty, all branches can be measured with this particular accessible node set; otherwise, only the branches in set B_m are measurable.

Using Algorithm 2, one can easily prove that, for the excitation/measurement patterns applied only on the top in the example of Figure 3.5, some of the measurements are redundant, and the branches on the third layer or below are not measurable (Figure 3.9). This is

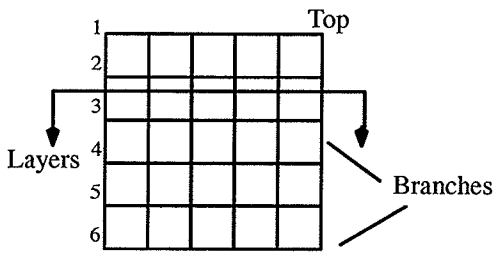

Figure 3.13 Branches not accessible in the three–dimensional network model

a similar result to what obtained with the sensitivity analysis. To make all branches measurable and to obtain faster speed of convergence, side excitations and measurements have to be added into the network about every two layers.

In practice, the accessible node set may be extendable. In this case, the Algorithm 2 can be performed first, then, by comparing the accessible node set N_a and the node set of non–measurable branches, new nodes can be added into N_a to make some branches measurable which we believe important.

3.3.4 Optimal excitation patterns in topological sense

By applying the graph theory, selection of minimal number of nodes can also be used to decide "optimal excitation patterns" which make the number of measurable branches maximal. This can be realized by performing the Algorithm 1 first to find the set of minimum number

of accessible nodes, then deleting the nodes not available from measurements. This "optimal" pattern is in the topological structure sense, which can be decided before the EICT procedure starts. Using the algorithm mentioned here, the excitation patterns and the positions of measurements can be easily arranged without increasing the determinacy.

By sensitivity analysis, a better set of excitation patterns can be pre–designed before an EICT algorithm starts.

3.4 Discussion

In this chapter, multi–port networks are used as discretized models to discuss the features of EICT algorithms and excitation/measurement pattern effects on recovery ability of EICT systems. The use of such models eliminates the truncation errors introduced by numerical methods in field calculations, simplifies the discussions on EICT algorithms, and clearly describes the excitation/measurement relationships based on the network and graph theory. Important contributions of this chapter can be summarized as follows:

1. The error function minimization algorithm can deal with both over– and under–determined problems, which the matrix inversion algorithms cannot do.

2. By applying sensitivity and accessibility analyses to a network with pre–designed structure, two approaches are presented to find a reasonable set of excitation patterns before an algorithm starts that either recovers an over–determined problem economically, or recovers a sub–network in an under–determined problem, which sub–network includes most of the information interested. In general, the EICT recovery problem is under–determined and the goal of this technique is to find a sub–network (sub–region) that includes information to be interested.

Considering the similarity between finite element discretization and the lumped element of networks, the approaches of designing excitation patterns can be easily extended to the two– and three–dimensional imaging. It is new to use sensitivity and graph theories in the EICT imaging. There are further issues open for discussions. More research is needed in future

to investigate the relationship between quality of image and the arrangement of excitation patterns.

CHAPTER 4

IMPROVEMENTS TO ERROR FUNCTION MINIMIZATION ALGORITHMS

Existing error function minimization algorithms are considered as slowly convergent algorithms in terms of number of iterations[46]. A long flat "tail" in the error norm plot, as shown in Figure 2.2 (b), can often be seen, especially in cases where objects are far from boundaries. It is difficult to judge from such convergence performance if the algorithms will actually converge or not. Slow convergence not only requires more computational resources, but also creates more chances for measurement errors to spread out in the entire region and to contaminate a recovered image. In this chapter, the relatively long image recovery process with the Wexler algorithm will be first demonstrated, then the causes of the slow convergent rate of error function minimization algorithms will be discussed. Finally, a modification scheme with an adaptively–controlled acceleration factor to speed up convergence with the Wexler algorithm will be introduced. The scheme predicts new element conductivities based on previous conductivity changes, and corrects the prediction with the minimization technique. The improvement is a general procedure which can be implemented in different error function minimization algorithms, and discuss both successful and failed simulation examples.

4.1 An Example Using the Wexler Algorithm

Figure 4.1 shows a sequence of images recovered using the Wexler algorithm in the example shown in Figure 2.2(a) after 50, 100, and 200 iterations, respectively . There are 64 squared quadratic elements in the mesh, and 9 Gauss points in each element. It is at these Gauss points that functions are sampled in order to evaluate the required integrals. 16 electrodes are arranged around the mesh boundary, and 8 pairs of current injections/extractions are applied. The measured potentials at the active injection/extraction electrodes are not used

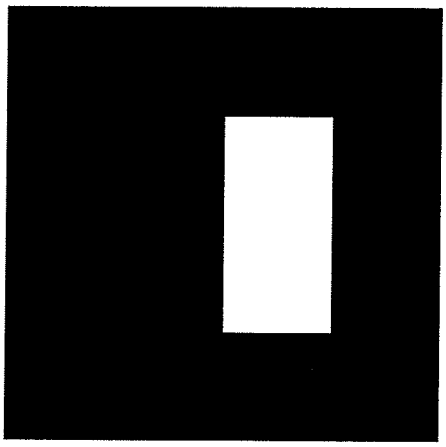

a. Original image
Contrast : 1:3

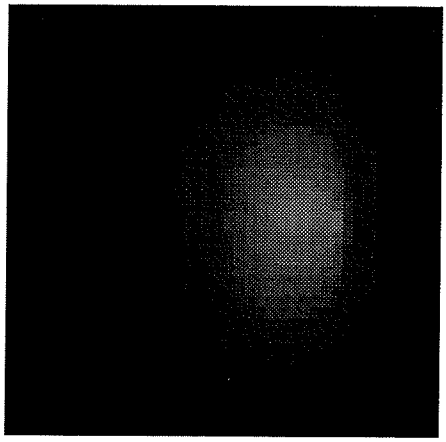

b. Recovered image
after 50 iterations

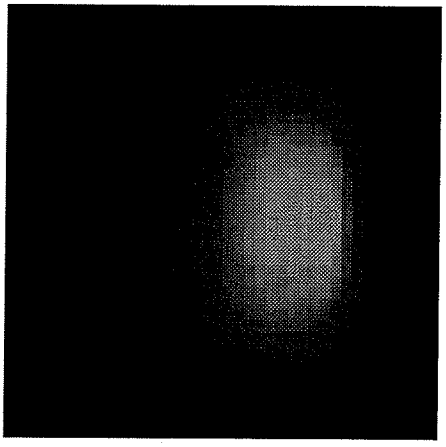

c. Recovered image
after 100 iterations

Figure 4.1 An example with the Wexler algorithm

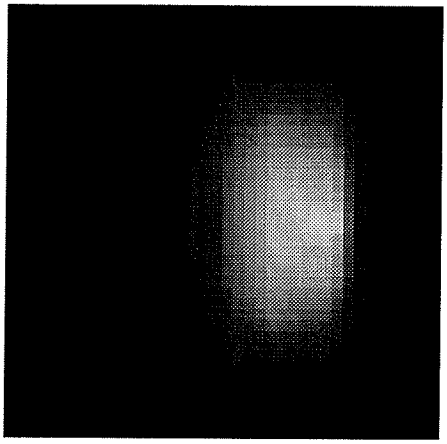

d. Recovered image
after 200 iterations

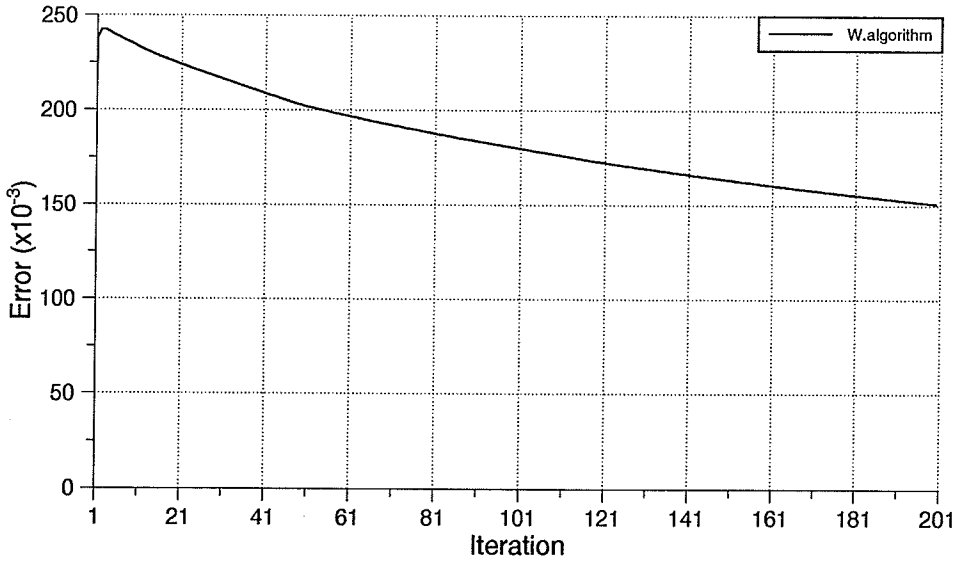

e. Error after 200 iterations

Figure 4.1 An example with the Wexler algorithm

to eliminate contact resistance effects when the Dirichlet boundary condition problem is solved. According to the formula derived in Chapter 3, there are 64 unknowns and 84 independent measurements corresponding to the 8 excitation patterns. Figure 4.1 shows that element conductivities are improved slowly but correctly towards their true values during the imaging procedure. The error norm reduces significantly only at the early stage of the procedure and thereafter at a very slow pace (Figure 4.1(e)).

4.2 Improvements on Error Function Minimization Algorithms

4.2.1. Error function minimization effects on convergence speed

Error function minimization algorithms minimize the total error for all applied excitation patterns at each iteration. Equation (2–31) shows the new element conductivity calculation formula based on the previous element conductivity and the calculated and measured potentials. From the equations in Chapter 2, it is clear that after the first several iterations the "driving forces" (the difference between calculated potentials and measured and the difference between the true conductivity distribution and the predicted) become smaller and smaller as the solutions approach to the true image. If the errors are in an acceptable range, this method is complete in recovering an image. Unfortunately, the recovered image at such an early stage is normally far from acceptable. In addition, the elements in the central part of the region "sense" even weaker "driving forces". The long flat "tail" in the error norm plot reflects the growing difficulties of determining the correct conductivity values of the elements far from boundaries.

4.2.2. General improvements in error function minimization algorithms

According to the discussions above, disturbance is needed after the error rate starts decreasing to make the "driving forces" stronger for the purpose of fast convergence. As the elements far from boundaries are not sensitive to the "driving forces", the modification should impose fast improvements on conductivity to the elements far from boundaries, not to those close to boundaries.

The fundamental idea here is to use the element conductivity changing rate given by the first several iterations as the maximal changing rate to predict the new element conductivity for every successive element in imaging procedure. The algorithm starts in its original way, and the conductivity changes for each element in the first several iterations are restored. Then, at each following iteration, compare the element conductivity change at the previous step with that currently given by the error function. When the two changes have the same sign, which means that the new change is along the same direction towards the true conductivity value, the previous conductivity change of this element is taken as the conductivity improvement at this step, but not the one calculated from (2–31). When they have different signs, which means that the previous change brings in more errors and is not suitable for the prediction at the next step, the new conductivity value is taken from error function minimization procedure ((2–31) in the Wexler algorithm). This happens when the previous change is too large and tends to go in the wrong direction, therefore, the error function minimization is needed to correct the convergence direction. The reason for us possibly to do this is that very likely, the iterations at early stage provide a rough solution and correct convergence directions for most of the element conductivities. Future changes of most element conductivities are possibly along the same direction as well.

With this improvement, the error function minimization guarantees the convergence direction by the least squared technique, while the use of the conductivity changes from the previous iterations gives the maximally possible conductivity change rates to speed up the convergence. Figure 4.2 demonstrates the error behaviour when the above improvement is applied to the example shown in Figure 4.1. In the first 10 iterations, the original Wexler algorithm is conducted. The improvement starts affecting from the 11–th iteration, and the error is reduced significantly. However, when the modification is more than enough aggressively, more errors are introduced. Then, the error minimization function starts working and tries to bring the algorithm back to the right convergency direction.

If we rewrite element conductivity at each iteration as

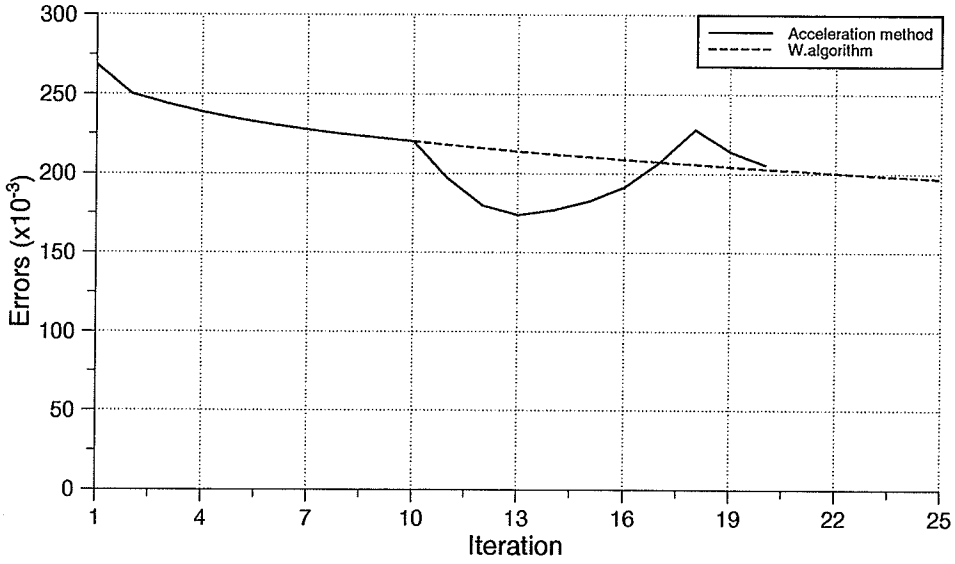

Figure 4.2 A demonstration of the improvement on error function minimization algorithms

$$\kappa_i^{n+1} = \kappa_i^n + \Delta\kappa_i^{n+1} \tag{4–1}$$

where κ_i^{n+1} is

$$\kappa_i^{n+1} = -\frac{\sum_X \int_{V_i} \mathbf{J} \cdot \nabla\phi \; dv}{\sum_X \int_{V_i} \nabla\phi \cdot \nabla\phi \; dv} \tag{4–2}$$

i.e.

$$\kappa_i^{n+1} = -\frac{\sum_x \sum_j \sum_l \sum_m W_{ijlm}\phi_l\phi_m\kappa_j^n}{\sum_x \sum_l \sum_m W_{lm}\phi_l\phi_m} \tag{4–3}$$

so, $\Delta\kappa_i^{n+1}$ equals to

$$\Delta\kappa_i^{n+1} = -\frac{\sum_x \sum_j \sum_l \sum_m W_{ijlm}\phi_l\phi_m\kappa_j^n}{\sum_x \sum_l \sum_m W_{lm}\phi_l\phi_m} - \kappa_i^n \tag{4–4}$$

By storing $\Delta\kappa_i^n$ after n–th iteration (i = 1, 2,...), we can compare $\Delta\kappa_i^{n+1}$ with $\Delta\kappa_i^n$ according to (4–4). If we call $\Delta\kappa_i^{n+1}$ from (4–4) as $(\Delta\kappa_i^{n+1})'$, then, the algorithm becomes:

If $\Delta\kappa_i^{n+1}$ and $(\Delta\kappa_i^{n+1})'$ have different signs, then $\Delta\kappa_i^{n+1} = (\Delta\kappa_i^{n+1})'$;

otherwise, $\Delta\kappa_i^{n+1} = \Delta\kappa_i^n$.

After the modification discussed above is implemented, new element conductivity is not always determined by error function minimization, but instead, by previous changes in element conductivity to obtain larger error minimization rate. Such replacement will be continuously performed till a disturbance is induced for the error function. At this point, there is more strength for the error function minimization, therefore, a new element conductivity is predicted again by the updating formula based on error function minimization.

To make the improvement work more effectively, an acceleration factor ω $(\omega > 1)$ can be introduced to the element conductivity change at each iteration, i.e. change (4–1) into

$$\kappa_i^{n+1} = \kappa_i^n + \omega\Delta\kappa_i^{n+1} \tag{4–5}$$

and the updating formula now is

$$\kappa_i^{n+1} = \kappa_i^n + \omega \left(-\frac{\sum_X \int_{V_i} \mathbf{J}\cdot\nabla\phi \; dv}{\sum_X \int_{V_i} \nabla\phi\cdot\nabla\phi \; dv} - \kappa_i^n \right) \tag{4–6}$$

Combine this with the previously discussed scheme, the complete modification of the algorithm is:

If $\Delta\kappa_i^{n+1}$ and $(\Delta\kappa_i^{n+1})'$ have different signs, then $\Delta\kappa_i^{n+1} = \omega\ (\Delta\kappa_i^{n+1})'$;

otherwise, $\Delta\kappa_i^{n+1} = \Delta\kappa_i^n$.

We call the improvement the *acceleration* scheme. Figure 4.3 gives the new flow chart of the improved Wexler algorithm.

At some point, increasing ω will cause the recovered image to converge to the true picture in an oscillatory fashion similar to what is shown in Figure 4.2. To make the factor perform more effectively, its value should be changeable during image recovery. At the beginning of the algorithm, the factor can be set larger to force the algorithm to converge in the correct

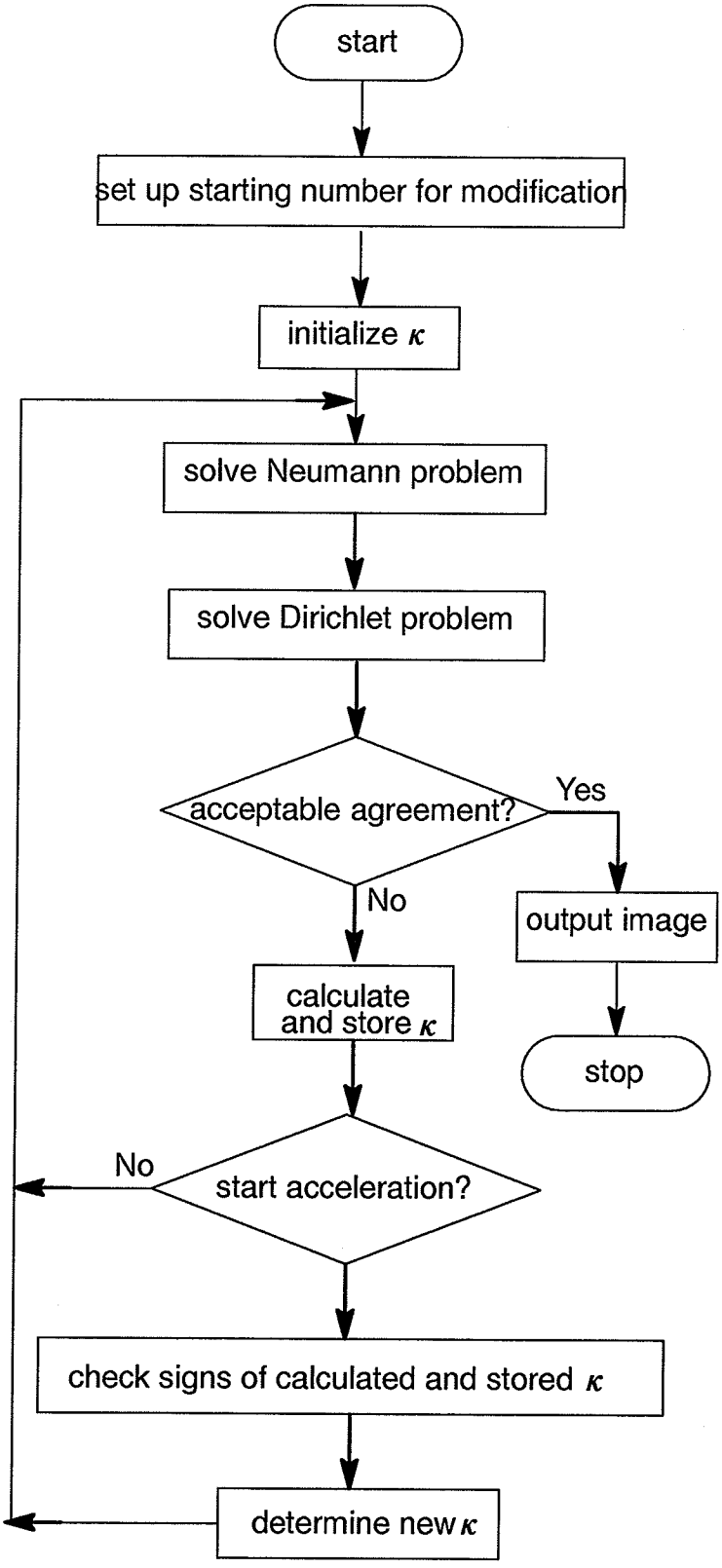

Figure 4.3 Flow chart of the improved Wexler algorithm

direction. Later on, as the recovered images are close to the true picture, large changes in element conductivity might cause large error for an error minimization function to correct. For this purpose, an adapted control scheme is implemented, which automatically adjusts the acceleration factor based on the potential differences between the Dirichlet boundary condition solution and Neumann boundary condition solution.

It is noticeable that ω can also be smaller than 1. In this case, the convergence procedure is more stable because it makes the element conductivity change more conservatively. Then, of course, the speed of convergence becomes even slower.

Figure 4.4 shows three error plots with different ω values.

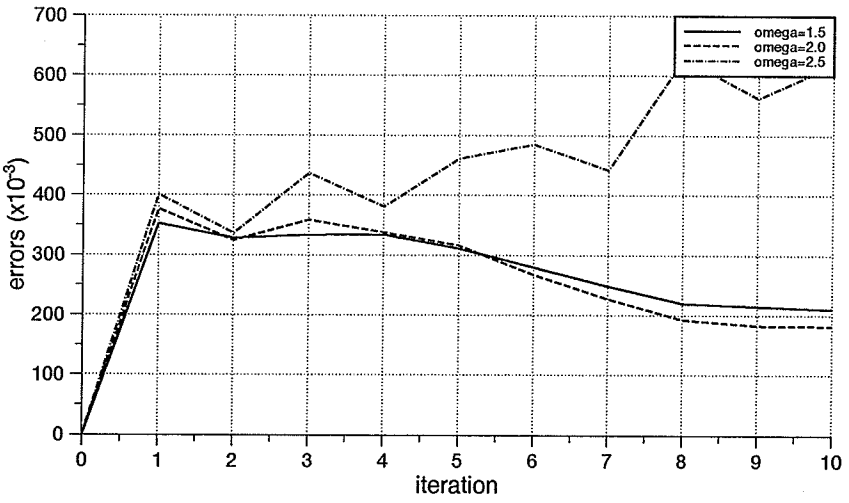

Figure 4.4 Acceleration effects on the convergence speed

The choice of the starting point for the acceleration scheme (i.e. the number of iterations needed to switch on the scheme) and its effectiveness are problem dependent. One suggestion is to pre–set up a number before the algorithm starts (there could be other principles). If the potential difference between the Dirichlet boundary condition problem and the Neumann boundary condition problem for the elements which are close to the boundaries increases right after the scheme is switched on, the pre–set up number is probably too small.

The algorithm can be designed to automatically switch off the scheme and re–set the starting point. In general, if the objects are far from boundaries and if there are larger contrasts between the objects and the background, the method is more useful. In the case that the objects are close to the boundaries, the scheme may not even be needed because the positions of the objects have already decided that the algorithm can converge quickly. With the improvements proposed here, the example in Figure 4.1 is tested again. The acceleration scheme starts to be effective after the 5–th iteration. Figure 4.5 shows the recovered image of the

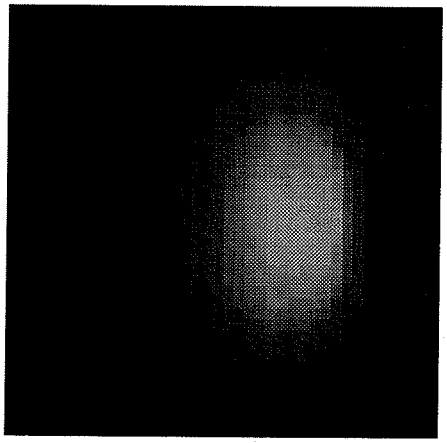

Figure 4.5 Improved convergence behaviour
with the algorithm modification

example in Figure 4.1 using the Wexler algorithms with the improvements after 20 iterations. It has almost the same quality as the one after 100 iterations with the original algorithm. From the derivation of the improvement, it is clear that the improvement is in fact a general modification to error function minimization algorithms. Similar modifications can be easily introduced into other error function minimization algorithms to achieve what we have shown here.

The significance of the combination of the error function minimization and the acceleration factor scheme is to speed up a class of EICT algorithms which have attractive potentials in three–dimensional EICT applications. The method used here applies the error function

minimization and acceleration scheme alternatively. They work together and constrain each other to keep the image recovering procedure proceeding efficiently in the right direction. Therefore, the acceleration scheme can be taken as a predictor for the algorithm, while the error function minimization is a corrector for the acceleration at different iterations. The method is different from the Equipotential Line method[46] in which the correction made to obtain a final image is conducted by matrix inversions and the imaging recovering procedure stops after one iteration with an image which may, very likely, include unacceptable errors.

The problem with the acceleration scheme is the difficulty to decide where the scheme should be applied, i.e. to separate the element conductivities which need to be improved greatly and which need not. The checking on the elements close to the boundaries cannot provide enough information to prevent this problem. When the contrast between the objects and the background are relatively low, or for the elements not too far from the boundaries, the wrong convergence direction could be picked up and exaggerated. In this case, it takes even longer time for the error minimization function to get rid of the errors.

CHAPTER 5

A PEAK DETECTION METHOD FOR ERROR FUNCTION MINIMIZATION ALGORITHMS IN EICT

The speed of error function minimization algorithms can be accelerated by predicting some of the element conductivities according to differences obtained in the early stages of an image recovery procedure. The problem associated this approach is the difficulty of determining exactly where the prediction should be applied, a determination that is crucial to the success of the algorithm with the improvement. In this chapter, an image processing technique based method, the peak detection method, is proposed to solve this problem. Similarly to the previous improvement methods, the method is initially "trained" by an approximate solution given soon after an algorithm starts. Instead of checking conductivity changes for each element, this method takes the entire body as a whole and finds the areas where objects most likely to exist. Simulation results show great improvements in the speed of convergence and quality of images, especially in the cases where significant contrasts between the background and objects exist. The improvements demonstrate how an image processing technique can be combined with a minimization approach in an inverse problem.

5.1 Possible Use of Image Processing Techniques in EICT Algorithms

As we have seen before, error function minimization algorithms cannot give an acceptable image with sharp edges in a reasonable time period. What they can produce is the image with "hills" of conductivity corresponding to the location of objects. How close the "heights of hills" come to their true values depends on the unknown conductivity distribution. The "hills" appear regardless of whether the computation is completed for several iterations or for several hundred iterations[23], i.e. the conductivity improvement directions for each in-

dividual element are given at a very early stage of computation. If one takes the image with "hills" generated in the first several iterations as a "trainer" for an algorithm, detecting the "peaks" of "hills" will tell the algorithm "hill" areas, which very likely, include objects with different conductivity distributions from the background. Picking the local maximum (or minimum) element conductivity values in every "hill" area detects the peaks accordingly. Then, the algorithm can modify the element conductivities with the acceleration scheme introduced in Chapter 4 in the neighborhood of each peak.

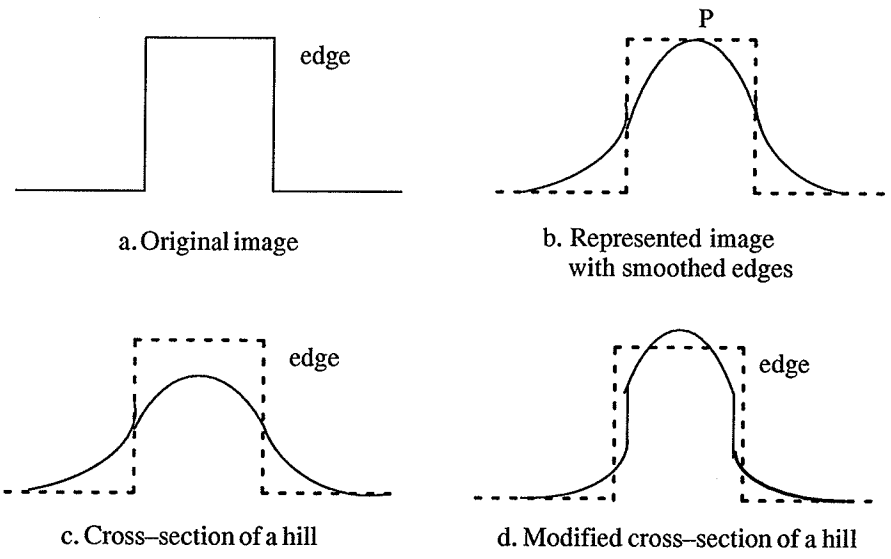

Figure 5.1 Image with sharp edges

Now, the neighborhoods have to be defined, where the modifications can be applied. In Figure 5.1, an image with sharp edges in (a) is normally represented by an image with smoothed edges as shown in (b). Various image restoration methods can be used to restore the image in (b) to an image very similar to that in (a). However, it is difficult to do so in the case of (c), especially when the "hill" is quite "flat". The smoothed image is actually the cross–section (Figure 5.1 c.) of one particular "hill" produced by an error function minimization algorithm at the i–th iteration. According to this feature, the neighborhood corresponding to a specific peak (point P in Figure 5.1 b.) can be determined as follows:

Assume the element conductivity at P to be κ_p and the background conductivity as κ_B , then

for the elements κ_n , if

$$\frac{\kappa_P - \kappa_n}{\kappa_P - \kappa_B} <= 0.5 \tag{5–1}$$

i.e.

$$\Delta\kappa_P - \Delta\kappa_n \leq 0.5\Delta\kappa_P \tag{5–2}$$

then κ_n will be replaced by

$$\kappa_n = \kappa_n + \omega \ \Delta\kappa_n \tag{5–3}$$

for the i–th iteration, where ω is the acceleration factor as defined in Chapter 4. Then, the image obtained after i–th iterations is shown in Figure 5.1 d. The sharp edge is then brought into the image but the size of the object is smaller than the original one with center element conductivity values higher. The image in (c) is much closer to the true solution in (a), therefore, image restoration techniques can restore the original image much easier and more clearly with this image. This detection–modification can be repeated every several iterations, depending on the errors introduced by the modification. If the errors keep decreasing, the modification can be applied at every iteration. Otherwise it is switched off and the improved element conductivities are calculated by the original error function minimization algorithm to bring the solution back to the correct direction.

In practice, a body to be studied may have several regions with different local maximal conductivities. The peaks corresponding to the regions including higher conductivity contrasts to the background, or with larger areas; or corresponding to the regions close to the boundaries, will appear earlier as an algorithm goes on. Therefore, the peak detection should be applied in every iteration, but only the areas with detected peaks, are modified at one iteration. In general, the modification is applied in different regions at different iterations according to the sensitivities of individual elements to the boundary measurements. The conditions to apply the peak detection and modification should finally be decided by sensitivity analysis.

5.2 The Peak Detection Method in EICT

The method now can be described as follows:

Step 1 Start an error function minimization algorithm with its conductivity updating scheme;

Step 2 After the element conductivities are updated, with the error function minimization algorithm at the i–th iteration, save the element conductivity change $\Delta\kappa$ with respect to the background for every element;

Step 3 Peaks inside the whole region are detected by finding the local maximal conductivity changes. To avoid detecting the maximal values induced by numerical errors, filtering technique should be applied before the peak detection. In the areas where the peak conductivity changes $\Delta\kappa_p$ exceeds a pre–set number (which can be some percentage of the background conductivity value), the modification described in (5–1) through (5–3) is applied; otherwise, the element conductivity keeps the value calculated from the error function minimization scheme. If the average potential difference between in the neighborhood of the local peak calculated and measured increases after last modification, the modification is not applied, which means that the previous modifications have made the conductivity values close to their true ones in this particular local area;

Step 4 If a peak conductivity detected cannot satisfy the condition in Step 3 after a certain number of iterations, it is probably that peak is corresponding to an object not sensitive to the boundary measurements. The modification can be applied continuously, starting from this iteration and stopping when the average potential difference between the calculated and measured increases.

Step 5 Repeat Step 2 to Step 4 until an acceptable error is achieved.

5.3 Simulation Results

Figure 5.2 and 5.3 show results from two examples with the peak detection method. The error function minimization algorithm used to test this method is the Wexler algorithm. The finite element mesh used in these examples is a 16 x 16 mesh with squared element. The

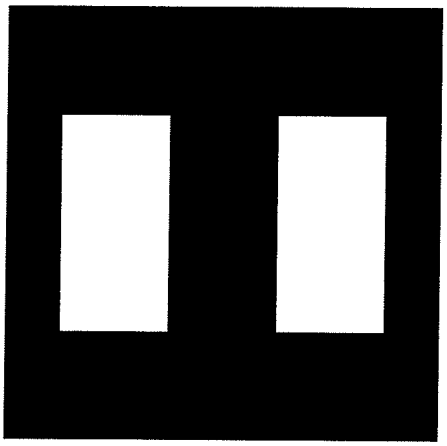

(a) Original image
Contrast : 1:5

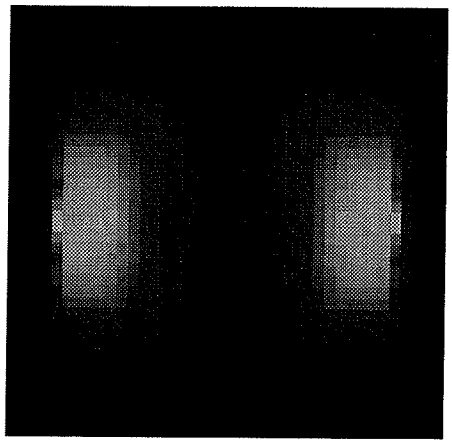

(b) Recovered image
with the Wexler
algorithm
after 20 iterations

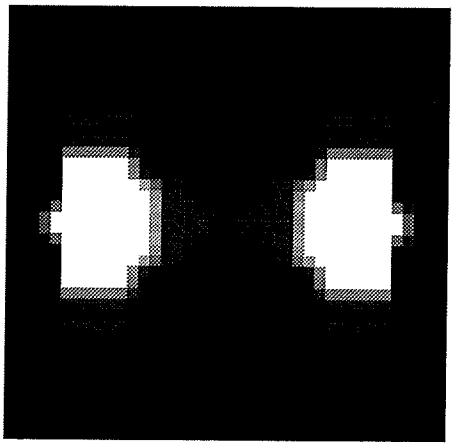

(c) Recovered image
with the peak
detection method
after 5 iterations

Figure 5.2 An example with peak detection algorithm — objects close to the boundaries

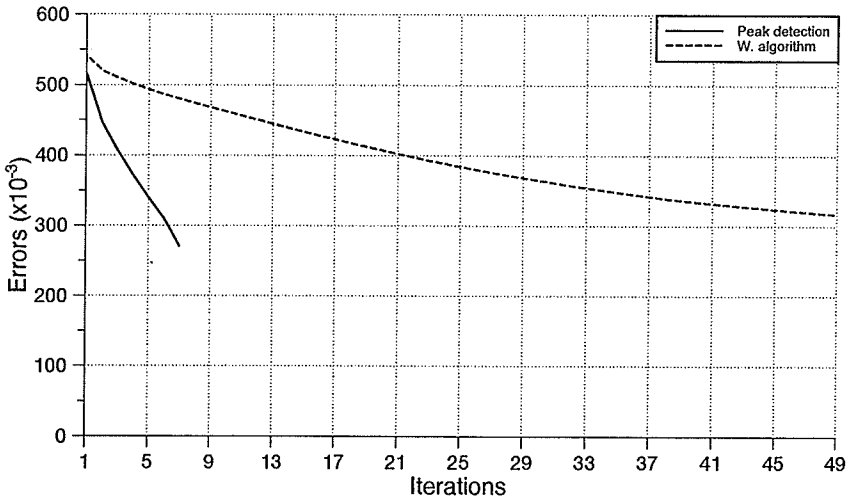

(f) Error comparisons

Figure 5.2 An example with peak detection algorithm — objects close to the boundaries

recovered images have much better qualities than those obtained without using the peak detection method. The computing time is also significantly reduced. From the error norm plots in the second example, we can see clearly that when the method is in its "training" duration, the error keeps the same as the original methods; when the modification is applied based on what it has "learnt", the error is reduced. Also, we can see that the modification on the element conductivity of the two objects with higher contrast(1:5) is applied after the first iteration and is turned off after the 5–th iteration; while the modification on the element conductivity of the object with lower contrast(1:3) appears after the 5–th iteration.

It is possible to run the simulations with a finer finite element mesh now since the peak detection method greatly reduces the number of iterations. This also makes it possible to recognize smaller objects, or objects with complicated boundaries, inside a body because of the relatively smaller element sizes used. We have tested the algorithm with the original image as shown in Figure 5.4 (a) with different contrasts. With the Wexler's algorithm, the image reconstructed after 20 iterations (Figure 5.4 (b)) does not tell anything, while the peak detec-

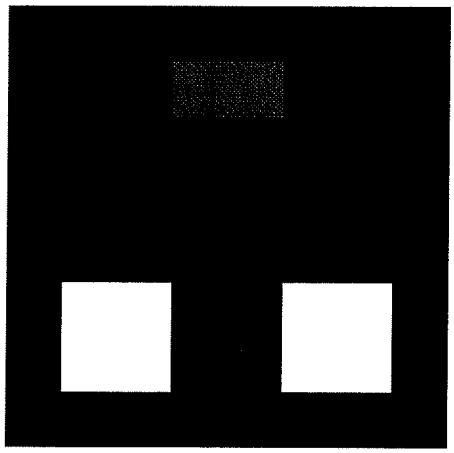

(a) Original image
Contrast : 1:2:5

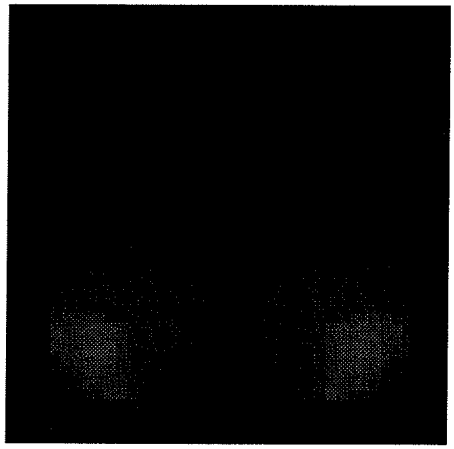

(b) Recovered image
with the Wexler
algorithm
after 20 iterations

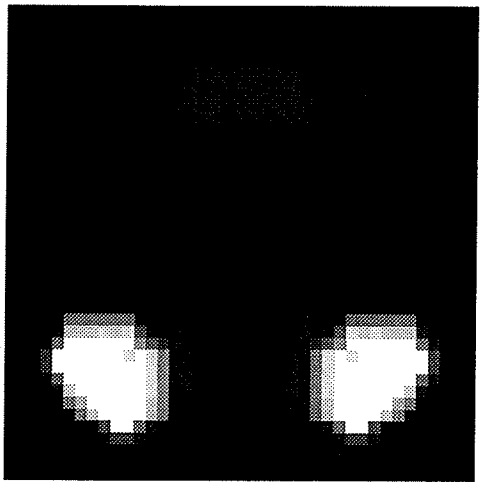

(c) Recovered image
with the peak
detection method
after 5 iterations

Figure 5.3 An example with the peak detection method — objects with different contrasts and sizes

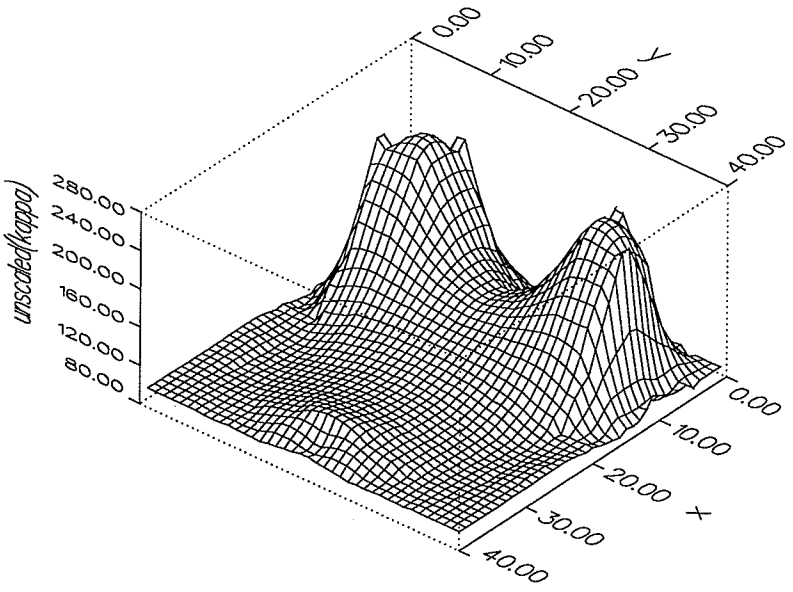

(d) Conductivity distribution of (b)

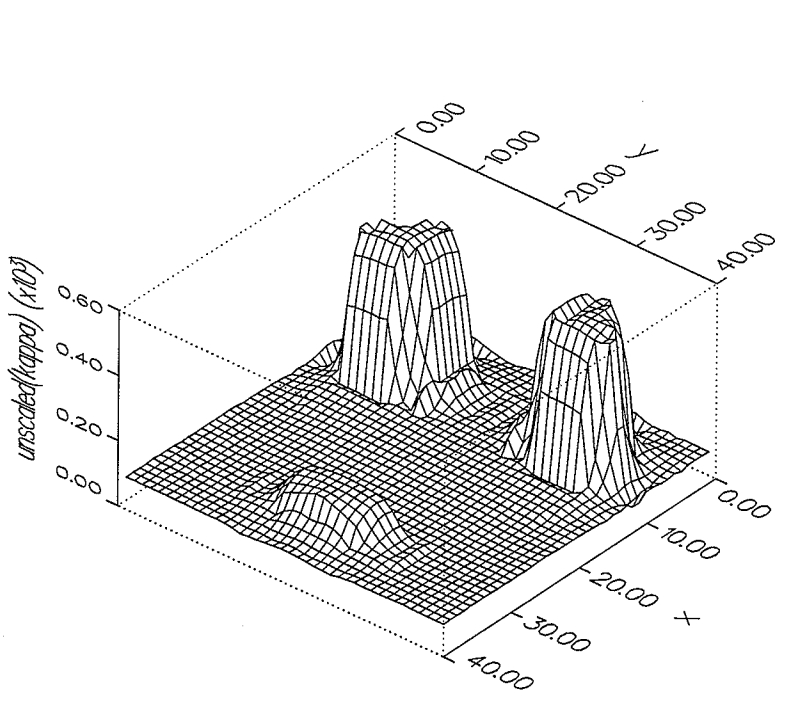

(e) Conductivity distribution of (c)

Figure 5.3 An example with the peak detection method — objects with different contrasts and sizes

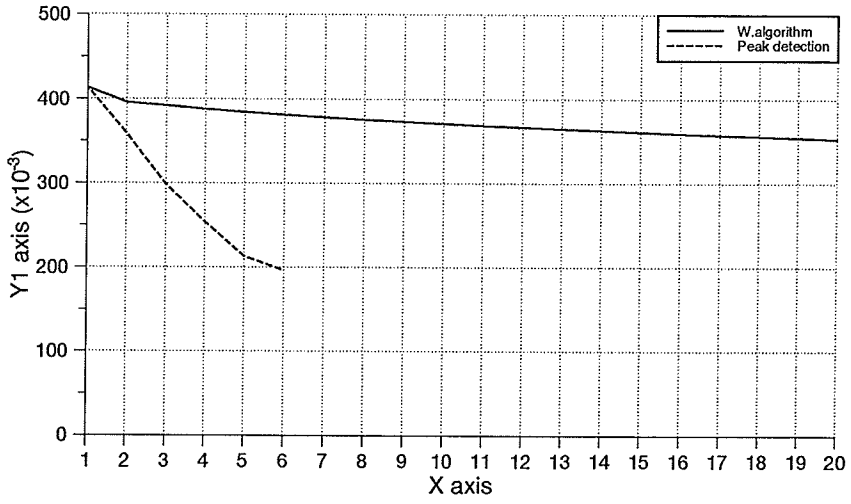

(f) Error comparisons

Figure 5.3 An example with the peak detection method — objects with different contrasts and sizes

tion method enhances the image (Figure 5.4 (c)) which is very close to the original picture.

5.4 Discussion on The Peak Detection Method

Ten years have passed since the first error function minimization algorithm, the Wexler's algorithm, was published[41]. The slow convergence rate that this type of algorithm suffers has prevented wider applications of EICT systems for three–dimensional imaging. The cause of the slower convergence rate in error function minimization algorithms is that the least squared technique only tries to minimize the errors but not necessarily make the error become zero. In the problem where sharp edges of objects have to be recovered, algorithms based on this technique cannot produce satisfactory images.

An image processing technique based method is proposed here to improve the convergence speed and image quality. With this method, we are able, for the first time, to recover sharp edges of objects using an error function minimization algorithm. For the recovery problem

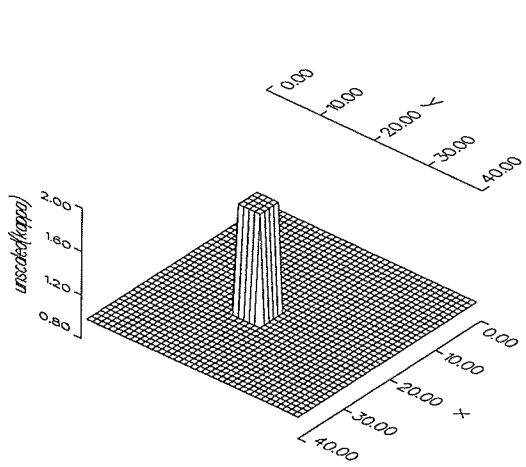

(a) Original image
Contrast : 1:2

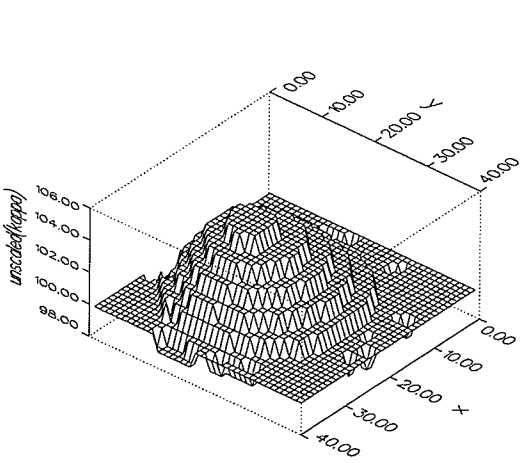

(b) Recovered image
with the Wexler
algorithm
after 20 iterations

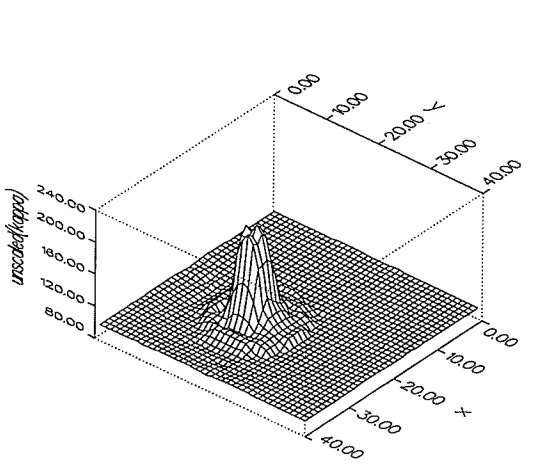

(c) Recovered image
with the peak
detection method
after 20 iterations

Figure 5.4 An example with peak detection algorithm
— small object far from boundaries

that needs more details, this method allows to use finer finite element meshes without experiencing the unbearably long computing time. Thus, it helps increase the resolution ability with this type of EICT algorithms. The success of using such a method in an EICT problem shows the possibilities of introducing artificial intelligence or image processing techniques into an inverse problem. The distinguishability of this method initially depends on the distinguishability of an error function minimization algorithm. It works as long as peaks can be detected from a "dirty" image generated by an error function minimization algorithm. This feature is more important when smaller(insensitive) objects are detected.

The peak detection and the associated modification schemes in the method are only executed once in each iteration in the conductivity updating procedure. They do not introduce too much extra computing time in the image recovery procedure. There might be a misunderstanding that the peak detection method is similar to the edge detection technique in image processing, but it is not. An edge detection technique needs a known threshold for the original image which is impossible to know prior to an EICT algorithm before it completes the computation. In addition, the edge detection does not give correct grey level values (which corresponds to the element conductivity here). As a result, the peak detection method is actually a combination of the least squared technique and an edge detection strategy.

This method requires the measurements around most of the boundaries in an EICT system; otherwise, faulty detections can occur in areas which are far from effective measurement sites. This problem will be discussed in detail later in EICT applications in three–dimensional imaging.

There are some open issues related to the application of this method in EICT systems. One important topic associated with the algorithm is the evaluation of resolution ability. Several methods, such as the point spreading method, are available to compare the resolution of images reconstructed with or without the peak detection method. More research should be done to give a complete conclusion on the resolution improvement. The example in Figure 5.4 demonstrates a simple way for such research. When a unit conductivity change from

the background is given to one single element, the image reconstructed by an EICT algorithm can be taken as the "response" to such change. A complicated distribution is the superimposition of single changes. The image corresponding to the complicated distribution is then the superimposition of the "responses". By comparing the "responses" from different algorithms, improved resolution ability can be evaluated.

Other interesting topics for further research are suggested as follows. The criteria used for peak detection can be defined more precisely so that the convergence procedure can be optimized for individual problems. The criteria to stop modification can also be different from what is suggested here, especially when some prior knowledge on the conductivity range in a practical problem are available before an EICT algorithm starts. Sensitivity and distinguishability with this method need more thorough discussions.

CHAPTER 6

FINITE ELEMENT MESH EFFECTS ON IMAGE QUALITY AND ALGORITHM CONVERGENCE

The limited number of electrodes is proven to restrict the resolution of images. One of the important features of error function minimization algorithms is that, with the Point Iterative Point Accumulative method, one mesh can be used in the forward problem and another in the conductivity updating procedure. By implementing two meshes in these algorithms, image quality can be improved efficiently under the same measurement conditions.

The image quality and convergence speed of an EICT algorithm are greatly influenced by two factors: how the algorithm starts and how a finite element mesh is designed[15, 46]. However, the initial distribution that controls how an algorithm starts, and a perfect finite element mesh to represent the detailed distribution, are not known in advance. Instead of starting an algorithm with a fine mesh, which may be redundant for a particular problem, we describe a procedure, in this chapter, that starts with a coarse mesh and ends with a proper mesh to obtain an image with expected accuracy. Compared with the direct use of fine meshes, this procedure greatly reduces computing time. We will also discuss the effects of finite element mesh designs on EICT images. This problem has been noted[4], but methods of dealing with it have not been suggested.

6.1 The Finite Element Mesh Effects on EICT Imaging

A finite element mesh affects image quality and convergence speed mainly in two ways.

6.1.1 Mesh effects on solution uniqueness

When the FEM is used to evaluate a potential distribution in EICT, it is desirable to have finer mesh to make the final image include more details of the original conductivity distribution. However, small element size in a fine mesh results in large number of unknown element con-

ductivities, which increases the computing time and requires large storage space. In addition, the number of independent measurements in a practical EICT system is limited by the number of applicable electrodes. If an over–determined problem is expected, therefore, small element size in a finite element mesh may not be allowed. This limits the recognition capabilities of the EICT technique.

It could happen with a relatively coarse mesh in an over–determined problem that an EICT algorithm fails to produce a unique image no matter how excitation patterns are arranged. In the example shown in Figure 6.1 (a), the edges of the recovered image can possibly be

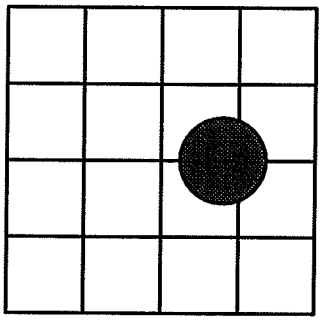

(a) An original image with a 4 x 4 mesh

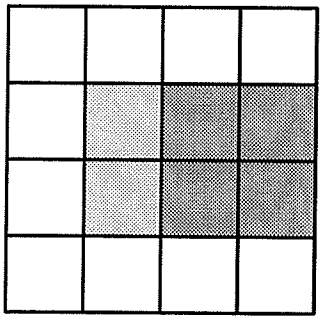

(b) A recovered image of (a)

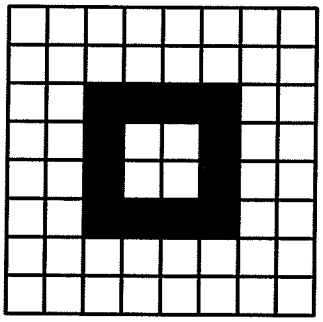

(c) An original image with an 8 x 8 mesh
Another example of "Ghost"

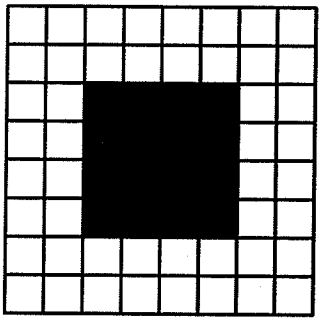

(d) A recovered image of (c)

Figure 6.1 Examples of "Ghost"

blurred in the four neighboring elements for any combination of excitation patterns. This is the so called "Ghost" phenomenon in EICT problem[4]. Such phenomenon can also be caused by objects insulated inside a region as in Figure 6.1 (c) . In these cases, an algorithm may still converge, but to a wrong solution as shown in the Figure 6.1 (d). It should be pointed out that the "Ghost" phenomenon is different from an under–determined problem. In an under–determined problem, images far from satisfactory are due to the lack of "views", provided that the finite element mesh is good enough to describe the true image with reasonable accuracy; but here, the unacceptable result is caused by the wrong design of a mesh which cannot describe enough details to represent the image. It is related to modelling issues.

6.1.2 Mesh effects on algorithm convergence

Although a coarse mesh may not guarantee the uniqueness of solutions, it saves recovery efforts greatly. Figure 6.2 shows three finite element meshes with different element sizes.

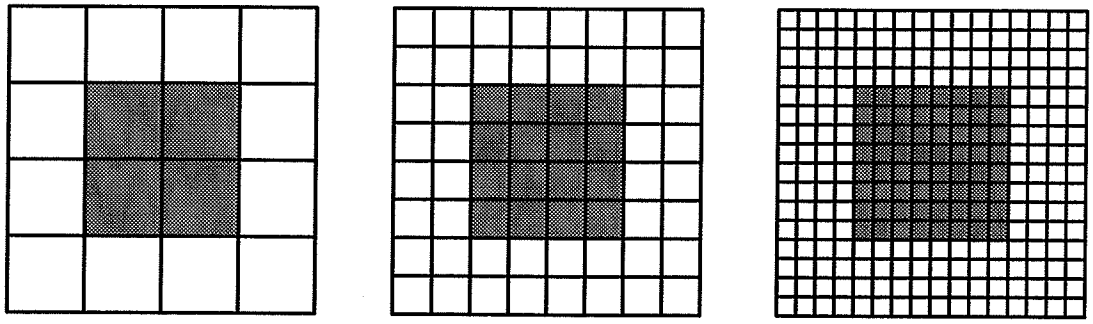

(a) a 4 x 4 mesh (b) an 8 x 8 mesh (c) a 16 x 16 mesh

Figure 6.2 Examples with different meshes

When the same image is recovered using these three meshes, an algorithm converges more quickly with the coarser mesh (4 elements on each side) than it does with a finer mesh (8 or 16 elements on each side). This is due to the fewer number of unknowns and the shorter path between objects and boundaries (as we discussed the accessibility before) in a coarser mesh.

The three examples in Figure 6.2 were conducted with the Wexler algorithm on a Sun Sparc 2 computer. The coarsest mesh (Figure 6.2 (a)) generates the best image (almost the same as the original image) in the shortest time, while the densest mesh (Figure 6.2 (c)) produces the worst image in terms of quality (Figure 6.3 (c)) in the longest time if the determinacy was kept the same. Figure 6.4 shows the CPU times used when an image is recovered with one of the three meshes in 50 iterations. As may be seen, the simulation time increases dramatically as the elements become smaller.

In the example of Figure 6.2, the coarsest mesh actually provides the best picture, because of the assumption of congruency between the object and the finite element mesh. If the congruency cannot be satisfied (it is impossible to have such congruency in practical situations), as shown in Figure 6.1 (a), the 4 x 4 mesh cannot work as well as it does here. Even though, the coarser mesh still tries to converge towards the true image at the early stage as shown in Figure 6.3 (d). The reason for the finer meshes' not working well in this case can be explained as the "redundancy". It reflects another problem: a finer mesh is not the best choice at all times. When an image can be described by a coarse mesh instead of a fine one, the use of fine mesh means to synthesize a simple system with a complicated model.

6.2 Image Quality Improvement by Conductivity Interpolations

Ideally, the smallest object that an EICT system would be able to recognize is in or greater than the average finite element size that an algorithm uses. The compromise has been demonstrated in image quality and convergence speed between meshes with different fineness. Using an non–unique mesh to save the computing effort is not realistic because the positions of objects are not known. Then, is it possible for a relatively coarser mesh to produce finer image without increasing determinacy (i.e. the number of excitations/measurements is kept unchanged)?

The potential distributions in the forward problem of an EICT algorithm are evaluated by the FEM. More accurate results can be achieved by using higher order elements with more

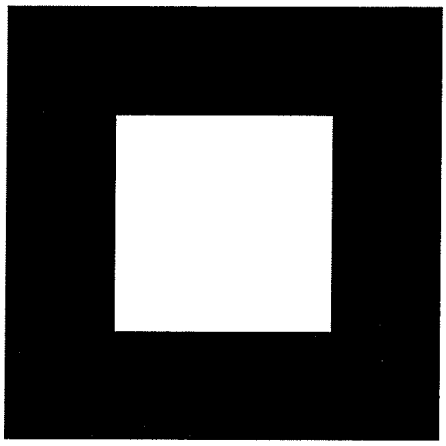

a. Original image
Contrast : 1:5

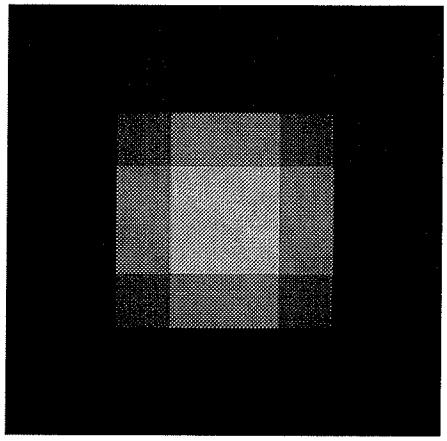

b. Recovered image
with 8 x 8 mesh
after 150 iterations

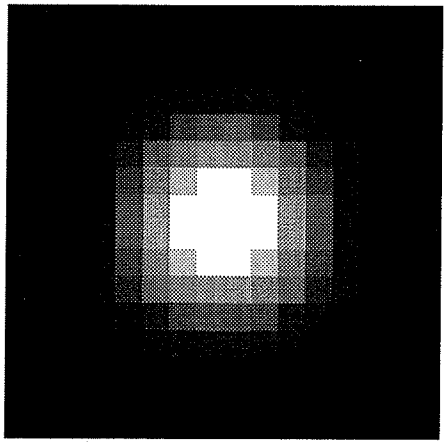

c. Recovered image
with 16 x 16 mesh
after 400 iterations

Figure 6.3 Simulation results of the example in Figure 6.2 (a)

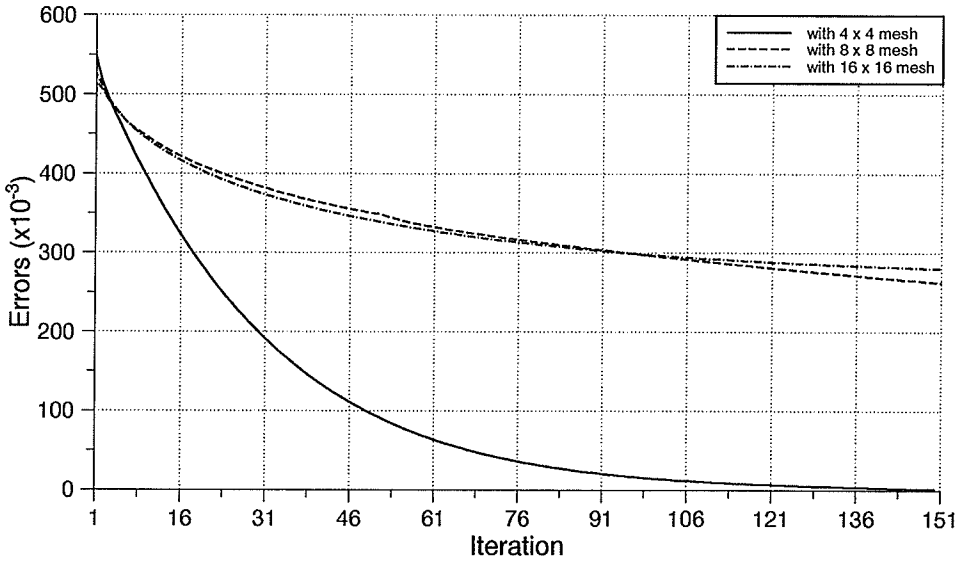

d. Error comparisons with different meshes

Figure 6.3 Simulation results of the example in Figure 6.2 (a)

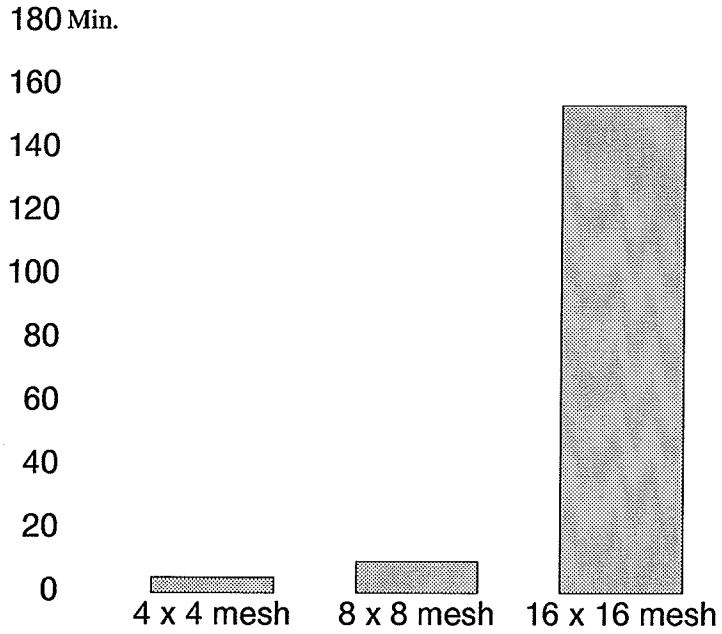

Figure 6.4 CPU time used for the three mesh cases in 50 iterations

Gauss points even larger size of elements have to be used. It is at these points that the integrals are evaluated. Therefore, the limited number of electrodes will not affect the accuracy of field calculations. It is the element conductivity (or image quality) that is affected the most by the element size of a finite element mesh.

Examine the error function minimization algorithms more closely, one can see that

(a) A finite element mesh is only used in evaluating the potential distributions. The evaluation procedure is independent of the conductivity updating procedure;

(b) The element conductivity updating formula is actually in the point form, as (2–43) represents. Conductivity at any point of the region can be interpolated by node potentials. The assumption of a constant conductivity distribution within an element is the case of using the conductivity at the central point of an element to represent the conductivity distribution in the rest of an element.

(c) The potential at any point inside an finite element can be calculated based on the node potentials and shape functions.

These analyses tell us that a finite element mesh used to solve the field problem does not have to be the same as the mesh used to update element conductivities. A "finer mesh" is naturally allowed in the element conductivity updating procedure if an error function minimization algorithm is employed. Then, it is possible to improve image quality without increasing determinacy and computing effort.

If we call the element used for calculating the potential distributions the "potential element", while the element used for updating the conductivity distributions the "conductivity element", we can represent a potential element with any number of conductivity elements to improve the accuracy. For example, if a potential element is represented with four smaller conductivity elements, the central point of the potential element can be used and the potential at that point can be calculated (Figure 6.5). Then, the mesh has been refined for the conductivity updating procedure. Four instead of one conductivities (κ_{ij} , j = 1, 2, 3, 4) representing the conductivity distribution will be computed with (2–9) in every potential element. In this

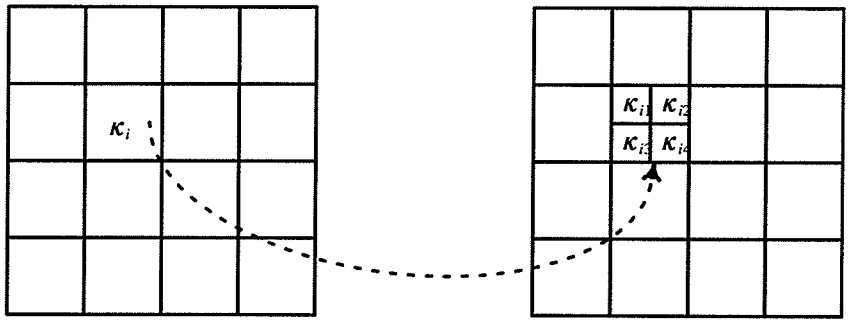

Figure 6.5 Meshes used in potential distribution evaluation and conductivity updating procedures

case, the accuracy is doubled approximately.

The scheme to choose the element mesh is not unique. The numbers and the positions of κ_{ij} for each potential element i (i = 1, 2, ...) can vary in different problems. A simple scheme is to make the new conductivity points in the refined mesh the same as those representing a higher order potential element since node potentials at such points are calculated anyway. Gauss points of higher order potential element are a natural choice for this purpose. Then, the conductivity updating formula becomes (2–46).

With this approach, coarser mesh with higher order elements are used to solve the potential distributions according to the measured boundary potentials and injected currents, while element conductivity is updated at each Gauss point inside every element. In a two–dimensional problem, if the quadratic element with 9 Gauss points is used to perform the integration, the Gauss points are available to update an element conductivity, i.e. each element conductivity can be represented by 9 different values. At each iteration, better evaluation of conductivity distribution is achieved, and therefore, the potential distribution calculated in the next iteration will be closer to the true solution. The accuracy is then increased up to 2 or 3 times. It is almost equivalent to the use of a finite element mesh with half the size of the original mesh.

By applying this conductivity mesh interpolating scheme, with almost the same accuracy,

one can solve a problem with 64 unknown using an 8 x 8 element mesh, instead of solving a problem with 256 unknown using a 16 x 16 element mesh in both the potentials evaluation and conductivity updating procedures. The updating procedure with mesh refinery is only performed once at each iteration. It does not cost anything compared with increasing the fineness of a finite element mesh. The algorithm therefore is more efficient in producing images with sharp edges, and more reliable in the cases that there is no congruency between the objects and the finite element mesh.

Figure 6.6 shows an example that compares the images reconstructed with/without the interpolation. The image quality is greatly improved with the interpolation scheme.

In conclusion, the element conductivity mesh interpolation method produces images of higher quality with a given number of available independent measurements. The savings in computing time and storage space are significant. For matrix inversion algorithms, it would be difficult to apply this scheme because the updating procedures in these algorithms cannot be separated from the potential calculation procedure.

The realization of this scheme using different meshes shows another good feature of the error function minimization algorithms. It works equally efficiently whether there are sharp edges in an image or not.

In the equation derivation, the interpolation ignores the coupling effect from the neighboring Gauss points, but will not affect the applications of the peak detection and modification method.

6.3 Find Better Initial Distributions with Coarser Finite Element Meshes

It has been known that a mesh with proper fineness is important for an EICT algorithm to recover an image of good quality. The question here is how to obtain a suitable mesh for a particular problem.

6.3.1 Initial guess effect

It has been shown that a better initial guess on conductivity distribution normally gives an

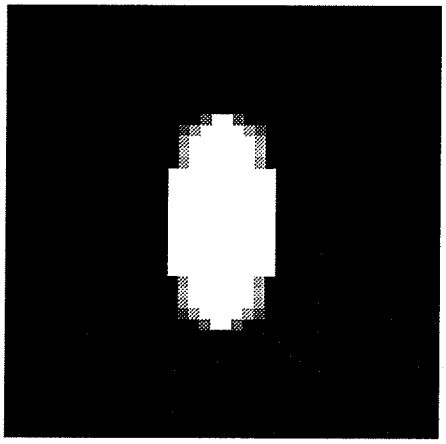

a. Original image Contrast 1:4

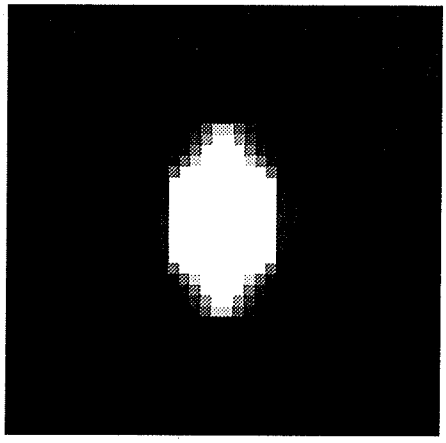

b. Recovered image with interpolation using the peak detection method

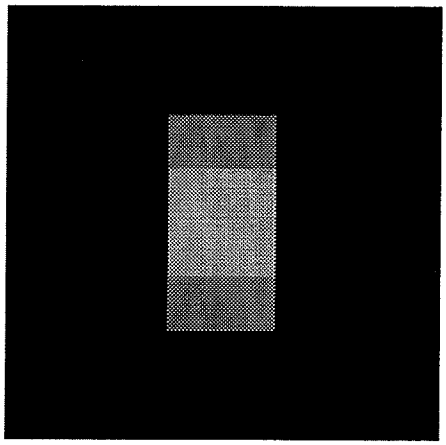

c. Recovered image without interpolation using the peak detection method

Figure 6.6 Comparisons on image quality with conductivity mesh interpolation

e2.intkap

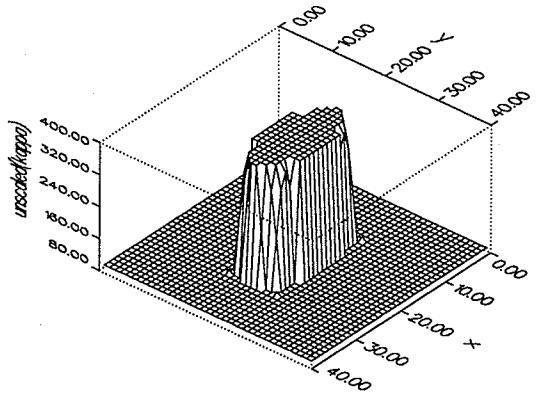

c. Original image in relieved form

e2.postkap

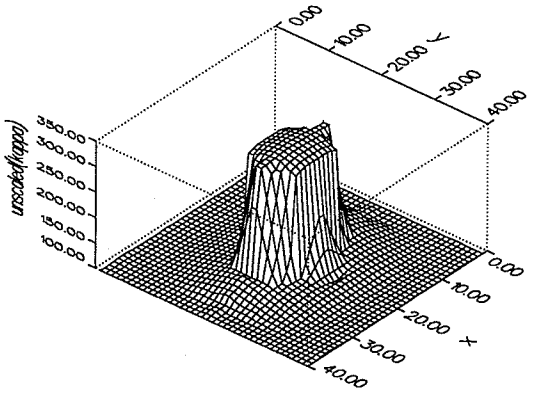

d. Recovered image in relieved form with interpolation

e2.postkap

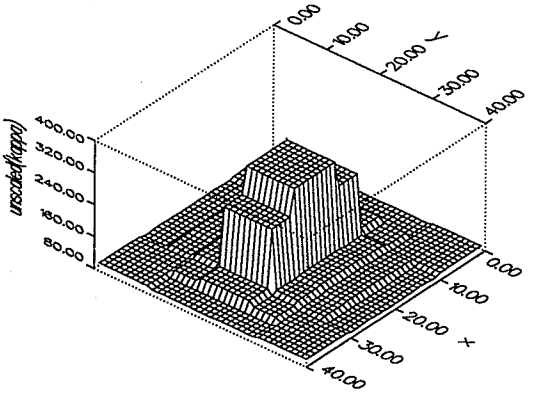

e. Recovered image in relieved form without interpolation

Figure 6.6 Comparisons on image quality with conductivity mesh interpolation

image with better quality[15]. However, a "better initial guess" cannot be known before the algorithm starts since it is actually a solution not far from the true one. Previous work on the mesh designs always employs a fixed finite element mesh through the entire image recovery procedure. In fact, more than one finite element meshes can be used to fit into the set of data obtained from the electrodes. During the imaging procedure, the image produced first by a former mesh becomes an initial guess for the successive mesh.

In general, the constant conductivity distribution assumed at the beginning of an EICT algorithm may not be a good one. A bad initial guess affects the solution of an EICT algorithm in three ways: (a) makes the imaging procedure diverge; (b) slows down the speed of convergence; (c) gives an unclear picture.

The convergence period will be greatly reduced if a coarse mesh is used first to obtain an approximate solution, then a finer mesh is used to reach the true image, provided the coarse mesh makes an algorithm try to converge towards the true solution when the meshes are switched.

From the examples shown in Figure 6.1, we can see that the first guess brings the maximal error (maximal potential difference) after an algorithm starts. Even a very coarse mesh gives a correct convergence direction[25] although such mesh cannot represent an image with great details. In the cases that edges of objects are not too different from the element sides, or there is no sharp edge changes, a relatively coarse mesh will generate an image with acceptable errors. If we use a coarser mesh to start imaging with part of the excitation/measurement patterns, the algorithm will try to converge towards the true image at least in the first several iterations. Images generated by coarser meshes after the first several iterations may not be good enough as a final solution, but will be certainly good enough as an educated initial guess for a finer mesh. This indicates that the image generated by a coarser mesh can be taken as an initial guess for the desired finite element mesh. There should be no doubt that such initial guess is also better than the constant initial guess because it is the image recovered from the measured information related to the particular problem.

6.3.2 Generating a better initial guess with coarser mesh

The convergence of an EICT algorithm can be faster if the algorithm starts with a relatively coarser mesh to obtain a better initial guess for the finer mesh. In the example shown in Figure 6.1 (a), the algorithm starts with the 4 x 4 mesh. During the first several iterations, the algorithm tries to converge to the true image. When the potential difference between the measured and calculated distributions increases, the coarse mesh is switched to the expected 8 x 8 mesh. The element conductivity of the new finite element mesh is assigned by interpolating the conductivity distribution obtained from the coarse mesh elements. More excitations/measurements are also added in to prevent the determinacy from being affected. The image from the coarser mesh is now the initial distribution for the 8 x 8 mesh. The computation time for each iteration is longer because of the increased number of unknown excitations. Such procedure can be repeated by switching into an even finer mesh, say a 16 x 16 mesh. Whenever switching occurs, there will be an average potential difference induced because of the errors between a coarser mesh and a finer mesh. Therefore, this scheme induces the potential difference to strengthen the driving force and to make the algorithm converge in the correct direction. The improvement on the convergence speed and the image quality is significant when a coarser mesh is used at the beginning. When the algorithm used the 4 x 4 mesh for 200 iterations and 10 and 5 iterations with the 8 x 8 and 16 x 16 meshes respectively, the total computer time is $14 + 5 + 22 = 41$ minutes, while it takes 150 minutes to run the algorithm with a 16 x 16 mesh only for 50 iterations. The computer time saved is about 90% to obtain images with similar qualities.

The scheme of obtaining better initial guess for a finer mesh

Step 1 Apply excitation patterns and make measurements using the mesh that an EICT system desires to use, or even a mesh finer than the one the system expects to use;

Step 2 Use part of the excitation patterns and the corresponding measurements to start an EICT algorithm with a coarser mesh whose nodes are the subset of the nodes of the designed

mesh, as shown in Figure 6.7. The initial guess on the conductivity distribution can be set

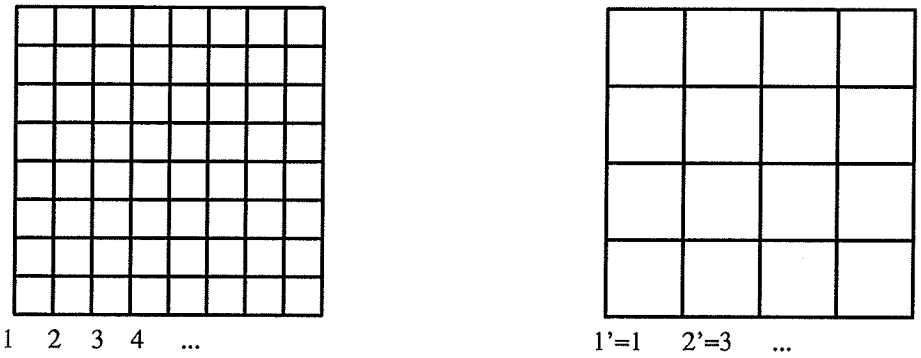

(a) The expected mesh with applicable electrodes

(b) A coarser mesh using part of excitations/ measurements

Figure 6.7 Using part of excitations/measurements with coarser mesh

as constant;

Step 3 When the potential difference between solutions with Dirichlet boundary condition and Neumann boundary condition is smaller than a previously set number (or the difference begins to increase), take the present conductivity distribution as the educated initial guess for the proper mesh (finer mesh) to be expected.

Step 4 Add the rest of the excitation/measurement patterns into the excitation/measurement sets, and start the algorithm with the finer mesh again till a reasonable solution is achieved.

Before an EICT algorithm begins, the mesh with proper element size is unknown. Therefore, in Step 3, the condition for an algorithm to switch from a coarser mesh to a finer one does not have to be satisfied in all problems because the coarser mesh may be already good enough for an algorithm to generate a good image. In this case, the coarser mesh is the suitable mesh for the particular problem and the result generated by this mesh is the final image the system can provide. The strategy to use this method is to keep using the coarser mesh as long as possible since the computing time consumed with a coarser mesh is much less than that with a finer mesh.

This method is independent of algorithms used in an EICT system. It produces more accu-

rate result in fewer iterations. When an algorithm with this scheme finishes, the suitable mesh for one particular EICT problem is found.

The way this method induces the potential differences is different from that the optimal current excitation pattern method does[10]. In the optimal current excitation pattern method, the pattern has to be updated as the imaging recovering procedure proceeds because the best pattern depends on the true conductivity distribution. The method finding an educated initial guess on the conductivity distribution does not try to find a better set of excitation patterns, but to make use of the errors among different meshes. When a different mesh is used, the number of excitations might be changed to provide enough number of independent measurements. This can be done before an image procedure begins.

CHAPTER 7

EICT IN TWO– AND THREE–DIMENSIONAL IMAGING

The final goal of a practical EICT imaging system is to recover a reliable final image inside a three–dimensional body using limited surface measurements. As pointed out in Chapter 1, most of the reported simulations and experiments with different EICT algorithms dealt with the reconstruction of images in two–dimensional slices using two–dimensional finite element models. In some cases, such models can describe a three–dimensional problem properly; but they cannot fully represent the behaviour of a complicated three–dimensional system in most medical/industrial applications.

In general, there are two aspects of three dimensional imaging which cannot be discussed thoroughly in two–dimensional modelling. First, there are fewer choices in element shapes to form finite element meshes in three–dimensional imaging. The large number of unknowns in a three–dimensional system restricts element complexity when computing time is considered. Second, a complete set of boundary measurements is not possible in many practical problems. The proper arrangement of excitation patterns is more critical for images with good quality.

In this chapter, the effects of excitation pattern and boundary measurement on image quality in two–dimensional imaging will be first demonstrated. A simulation example for a medical application is presented to show the flexibility of error function minimization algorithms. Then, finite element models in three–dimensional imaging is discussed. And finally, three–dimensional image quality under particular excitation pattern arrangements is specially addressed.

7.1 EICT in Two–Dimensional Imaging

The finite element mesh we use here is shown in Figure 7.1. The square mesh has eight sec-

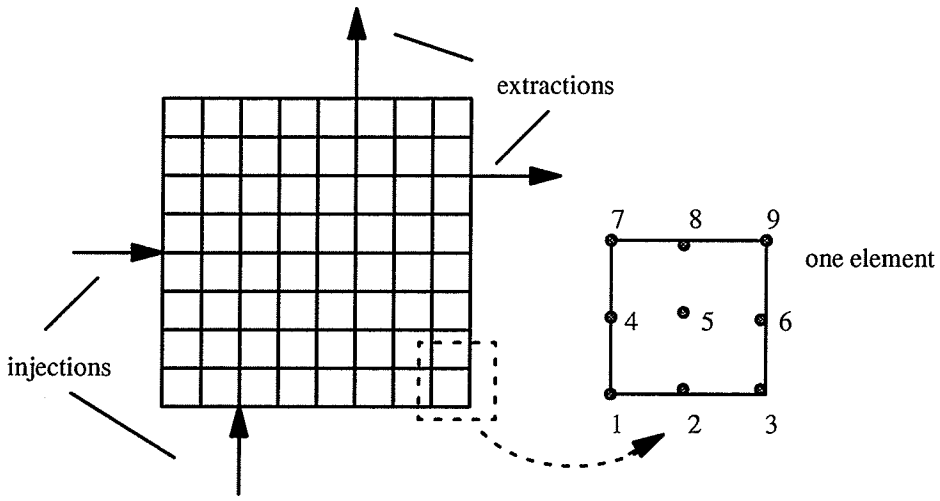

Figure 7.1 A finite element mesh

ond–order quadratic elements on each side. There are total 289 potential nodes and 64 elements in the mesh. 32 electrodes are placed around the boundary and 8 excitation patterns are applied.

7.1.1 Excitation pattern designs

We discussed this topic with sensitivity and accessibility in Chapter 3. An adaptive current injection scheme[10], which modifies the distribution of injected current on the boundary at each iteration, can be used to achieve an optimal excitation pattern to distinguish objects from the background under a certain measurement accuracy requirement. As the recovered image approaches the true solution, the optimal excitation pattern for that particular problem can finally be determined.

Two problems with this pattern should be addressed. One is that the excitation patterns might be changed during the imaging procedure, which requires fast data processing ability from the EICT system. The other is the optimization results in a current injection distribution around the boundaries, i.e. there are more active sites for each excitation pattern. The potentials at those active nodes have to be discarded for the purpose of eliminating the contact resistance effects. As the number of active potential nodes increases, the remaining un–active potential nodes may not be able to provide enough independent measurements. It could ruin the results improved by applying the optimal excitation patterns. Further more, the use of

optimal excitation patterns improves the convergence behaviour only in the first few iterations but not as well afterwards[15]. In a practical EICT system, the speed of the devices might be restricted, and the contact resistance effect is more significant. Therefore, it may not be realistic to search for and to implement optimal excitation patterns while an image is under recovery.

As studied in Chapter 3, it is impossible to choose efficient parameter–related excitation patterns before an EICT algorithm starts because proper excitation patterns depend on the unknown conductivity distributions. However, based on sensitivity or accessibility analysis according to the similarities between the network conductance recovery and the conductivity distribution imaging, the excitation patterns can be pre–defined after a finite element mesh is specified.

Assume the finite element mesh as shown in Figure 7.1. Sensitivity at port AB corresponding to excitations can be calculated. If we use the horizontal axis for the positions of elements of the central line, and the vertical axis for the sensitivity measured from the specified excitation pattern, Figure 7.2 shows similar features that we found in a resistive network recovery. Then, the excitation patterns should be arranged in this way to find sensitivity related reliable regions in the sense of sensitivity: a. more cross patterns (every two rows / columns / layers) because more details would be revealed from measurements induced by such patterns and less measurement noise would be involved; and b. some corner patterns.

If we represent each element of a finite element mesh with the network model shown in Figure 1.1 (a), the mesh is changed into a network with one element covering several branches. Although the equivalent network for a finite element mesh is not unique, but it uses the same potential nodes, where the field is evaluated. After the conversion, the accessibility discussion in a field case becomes a measurable problem of a network. Then, the theory developed for network recovery can be directly applied to obtain similar conclusions. The previous proposed algorithms for determining accessibility can also be employed. When branch conductances, corresponding to some element conductivities, in the entire mesh are accessible, the

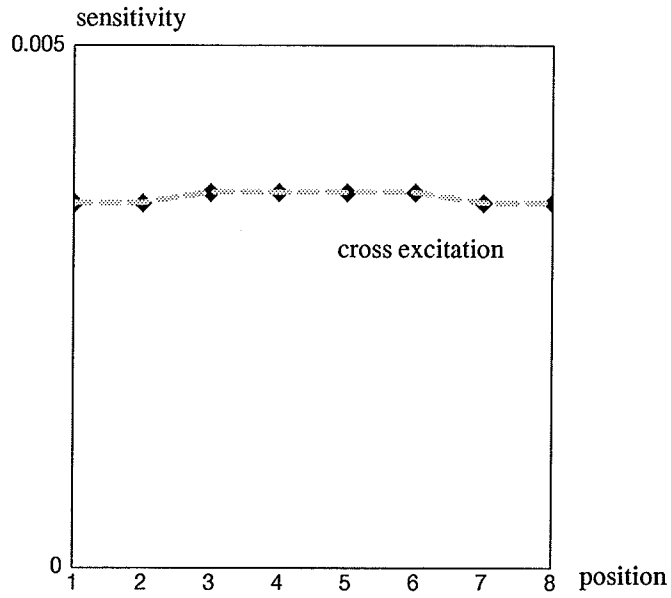

a. Sensitivities for chosen elements and excitations

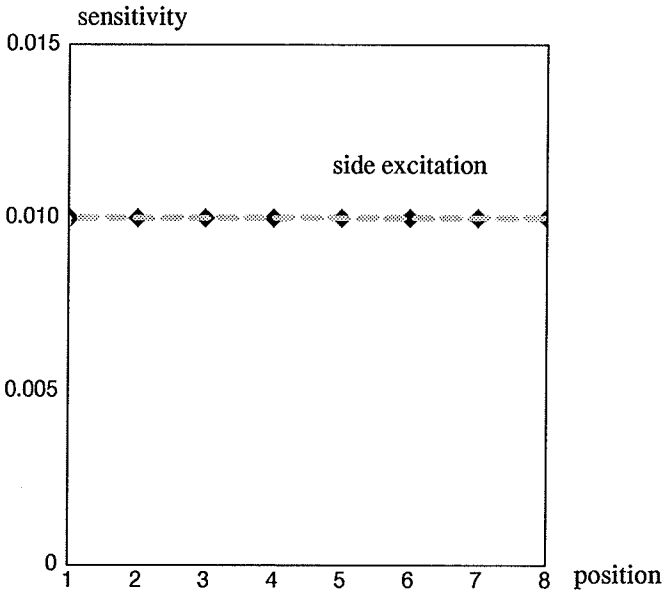

b. Sensitivities for chosen elements and excitations

Figure 7.2 Sensitivities for chosen elements and excitations

algorithm gives the fastest convergence speed. When the maximal number of independent measurements is limited by the number and positions of electrodes, optimal excitation patterns in the topological (or sensitivity) sense can be pre–designed. The reason for designing excitation patterns with sensitivity or accessibility theory is that better patterns are determined in advance so that the contact resistance elimination will not be affected.

7.1.2 Boundary measurement effects

Measurement error effects introduced by boundary distortion In a practical medical case, electrode positions for measured potentials on the surface might be displaced by the body movement. Most of EICT algorithms will fail to produce any image in this case[46]. We discuss this effect in detail with an example using the peak detection method. The simulation is designed by assuming that the "measured data" on the stretched sides are taken from the potentials at inner nodes calculated from the exact solution. The original image is the one shown in Figure 6.1 with the contrast of 1:5. When two sides along the Y–axis are stretched for 1/16 of the total length of one side of the boundary (half length of one element side), the recovered image is stretched in the same direction and about the same ratio as shown in Figure 7.3 (b). Some conclusions from the simulation results can then be drawn:

(1) If the stretching becomes more significant, the stretched image loses its original shape completely.

(2) When different measurement patterns are applied, the image obtained by applying always patterns is most seriously affected. This is due to the maximal potential changes at active excitation sites. When stretching takes place, the potentials used at active excitation sites introduce the largest difference between the correct values and those affected by the stretching.

(3) The part of image which is closest to the stretched boundary is distorted the most, while the parts which are far from the stretched boundary remains un–affected (see the two sides in the image along the X–axis).

This example demonstrates the insensitivity of error function minimization algorithms to

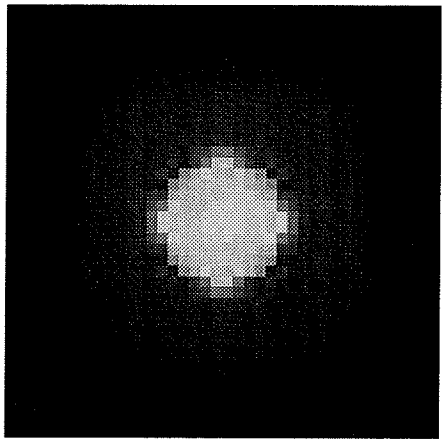

a. Recovered image without distortion

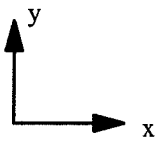

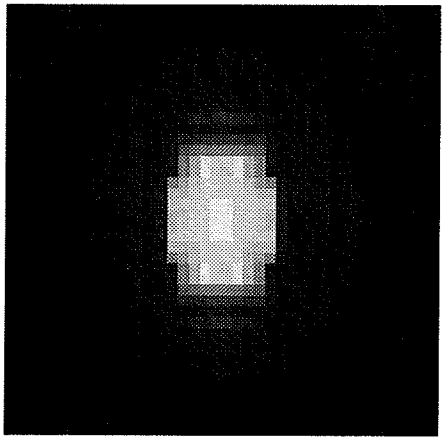

b. Recovered image
with two sides distorted

Figure 7.3 Measurement error effects introduced by boundary distortion

boundary measurement errors. It shows that error minimization algorithms are relatively robust to boundary displacements. When the boundary of a body to be examined is slightly stretched, algorithms can still manage to generate an image not too different from the true solution. In clinical situations, if the stretching made by body movement is known in advance, the distorted image can be restored more easily.

Measurement error effects introduced by device precision Matrix inversion algorithms are known to be sensitive to measurement noises[27]. It can be a very ill–conditioned problem in a practical EICT system, especially when the objects inside the body are far from the

boundary. Now, we will see how error function minimization algorithms behave when measurement errors, due to device precision are introduced. A uniquely distributed random noise is added to the calculated boundary potentials from the true solution to model the measurement errors in a real system. Suppose the exact boundary potential at node p to be V_p. The actual boundary potential V_p' with measurement error at this node then becomes

$$V_p' = V_p(1 + X(p)) \qquad (7\text{–}1)$$

where X(p) is a unique distributed random variable in $[-\delta, \delta]$ ($\delta > 0$). If an original image is as shown in Figure 7.4 (a), we add errors to measurements by changing δ from 0 to 0.1. Figure 7.4 (c) to (f) give two recovered images with different δ . Simulations show:

(1) The algorithm manages to converge to the true image when $\delta < 0.1$;

(2) Distortions occur when measurement errors are introduced;

(3) Always patterns is a better choice to eliminate measurement errors;

(4) Measurement errors have more sever effects on images when an algorithm runs for a long time because the errors spread out gradually from boundary to the entire region. Algorithm acceleration by any means, such as the peak detection method, will help reduce the damage. This problem deserves being discussed more thoroughly. It is not only related to the signal–noise ratio, but also to the contrast of the image and the true conductivity distribution. The conclusion at this stage is that the error minimization algorithms are more robust to the measurement errors than matrix inversion algorithms.

Measurement device designs for boundaries in irregular shapes In practical situations, boundaries of a body to be examined are normally in irregular shapes. Instead of modelling the irregular boundary with different shapes of finite elements, we can apply the EICT algorithms in a larger region with boundaries in regular shapes and include the boundaries in irregular shapes as part of the image. Figure 7.5 shows an example for this proposal.

Relations between efficiency and image quality We use the Wexler and the Yorkey algorithms to discuss this problem briefly. The main difference between these two algorithms is that the Yorkey algorithm minimizes the errors between the calculated potentials and mea-

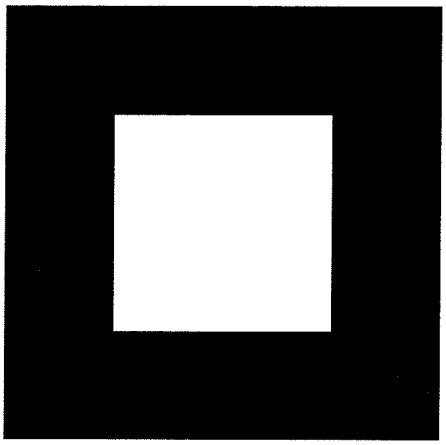

(a) Original image
Contrast: 1:5

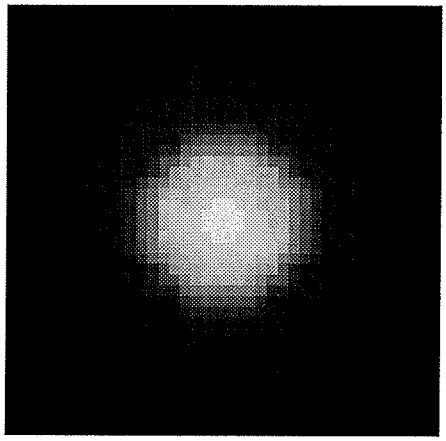

(b) Recovered image with
$\delta = 0.0$
iteration = 10
with the peak detection

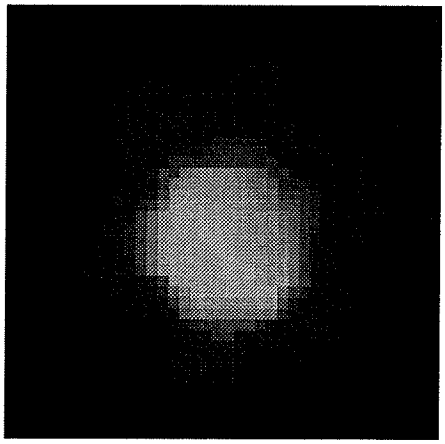

(c) Recovered image with
$\delta = 0.005$
iteration = 20
with the peak detection

Figure 7.4 Effects of measurement precision on image quality

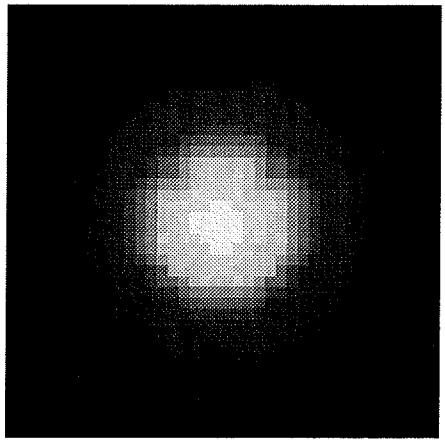

(d) Recovered image with
δ = 0.01
iteration = 20
with the peak detection

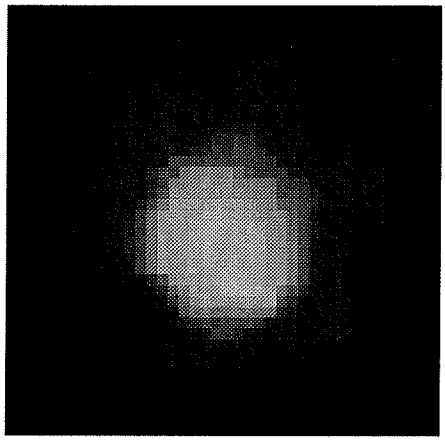

(e) Recovered image with
δ = 0.05
iteration = 20
with the peak detection

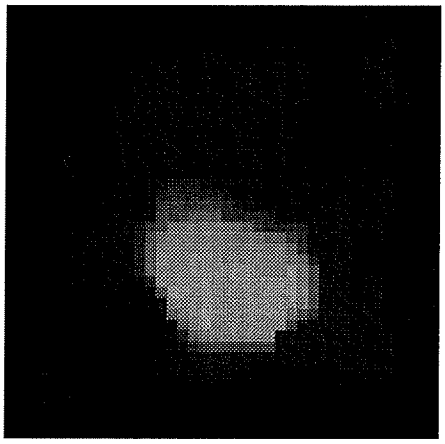

(f) Recovered image with
δ = 0.1
iteration = 20
with the peak detection

Figure 7.4 Effects of measurement precision on image quality

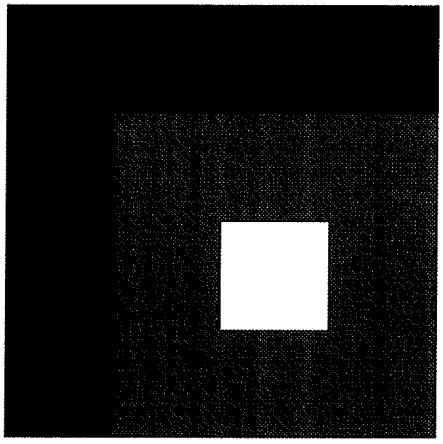

a. Original image
Contrast: 1:5

original body

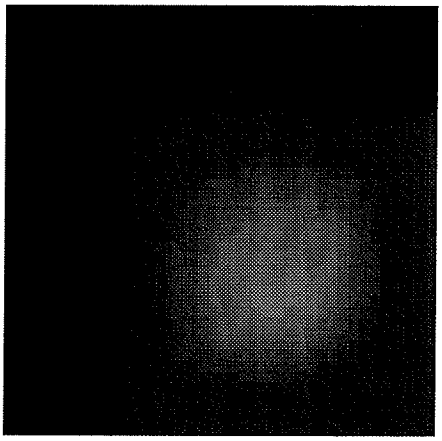

b. Recovered image
with the Wexler algorithm
iteration = 50

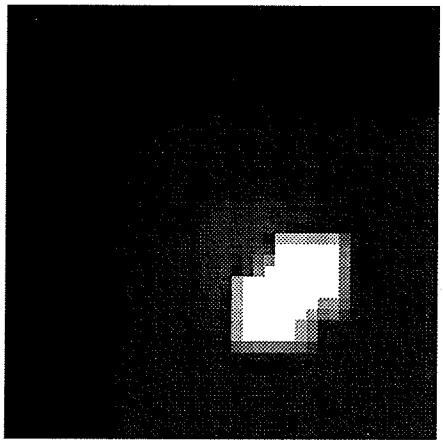

c. Recovered image
with the peak detection method;
iteration = 50
modification is effective at
iteration = 20 and iteration = 30,
respectively

Figure 7.5 Example of irregular shape processing in EICT

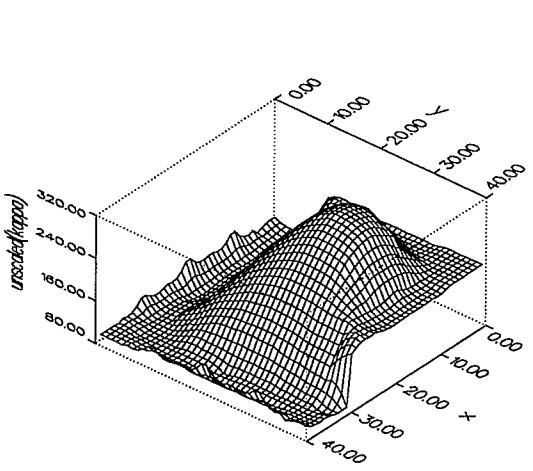

d. Recovered image with the Wexler algorithm
iteration = 50

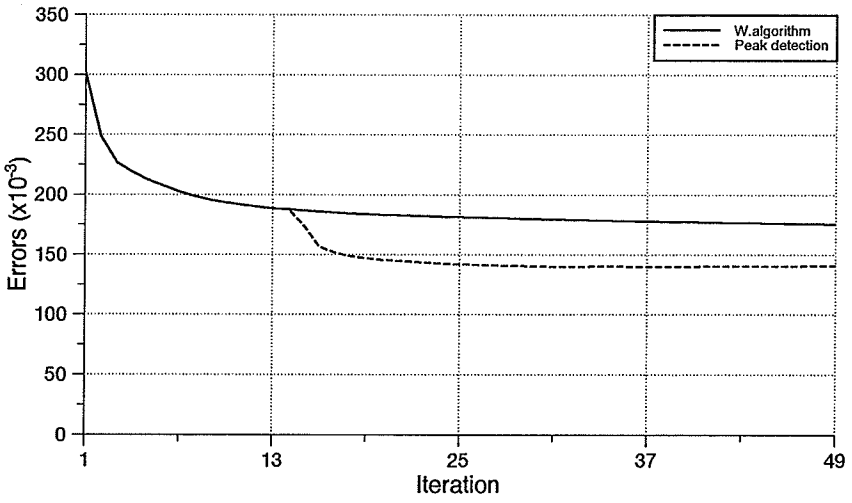

e. Errors from two methods

Figure 7.5 Example of irregular shape processing in EICT

sured potentials on the boundaries, while the Wexler algorithm minimizes the errors between those potentials at individual elements. For the former algorithm, the inner element conductivity information has to be mapped into the output minimization function correctly, so that the algorithm deals with smaller sizes of excitation/measurement sets, and the recovering

procedure can be faster. From the system identification (or network synthesis) point of view, the availability of mapping information into the output measurements requires all element conductivities in a mesh to be "measurable". If this cannot be satisfied (i.e. the mesh is not "measurable"), the solution from the Yorkey algorithm may not be unique. The Wexler algorithm does not need to map the inner element conductivity information into the boundary measurements. It is, in theory, able to identify all element conductivities whether the whole mesh is "measurable" or not. Such algorithms, of course, require more efforts (i.e. long convergent period) to generate an image.

7.1.3 Simulation results of thorax in two–dimensional EICT imaging

The finite element mesh used in an EICT system does not have to be congruent with objects inside the body. In fact, it is impossible to make it congruent in a real system. Previous work used the finite element mesh shown in Figure 7.6 (a)to solve the thorax problem. In this section, we demonstrate how error function minimization algorithms solve this problem with different recovering finite element meshes. Three finite element meshes, with 90,120, and 160 elements, respectively, are used to recover the image. Figure 7.6 (b) gives a sample of the mesh used in the simulation. There is no congruency between the mesh and the objects in the body with any one of these meshes. The boundary of the chest is irregular. 32 electrodes are placed around the chest to collect measurement data. 8 pairs of excitation patterns are applied. The sometimes patterns are used to eliminate the contact resistance effects. All the meshes give similar images of the examined chest (Figure 7.7 (a)–(c))). We can see clearly the positions of lungs, heart, and back bone. The total errors are less than 5%. The largest error of element conductivities is 20% of the original values. Figure 7.7 (d) and (e) give the plot of the conductivity comparisons at two cross–sections of the thorax. If an even finer mesh is used, the image quality does not improve significantly. Only are smoother boundaries of objects achieved. This is the numerical manifestation of the physical measurement limitations. The imaging procedure stops when the difference of boundary potentials between the measured and the calculated is smaller than a pre–set number. Further improve-

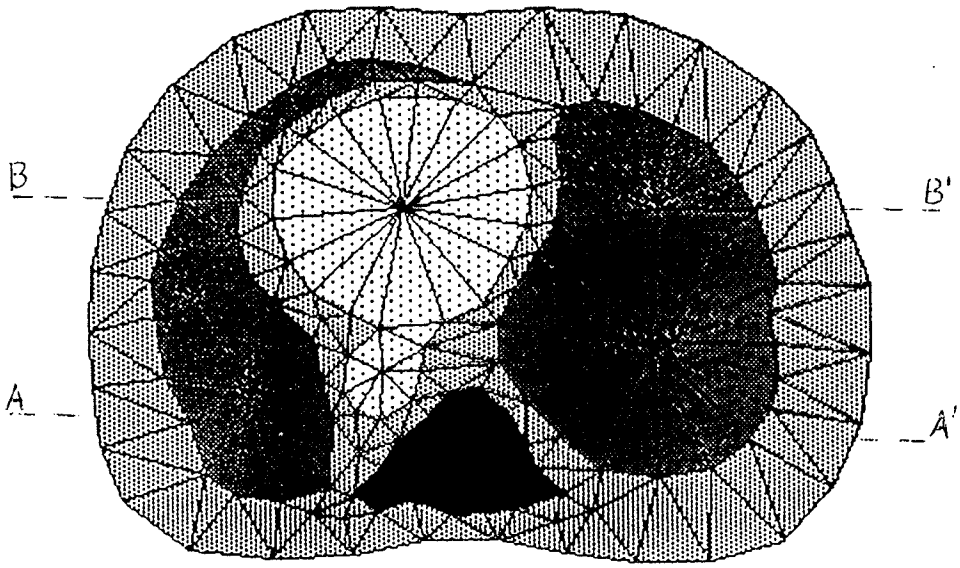

(a) Finite element mesh for thorax image problem used in previous work

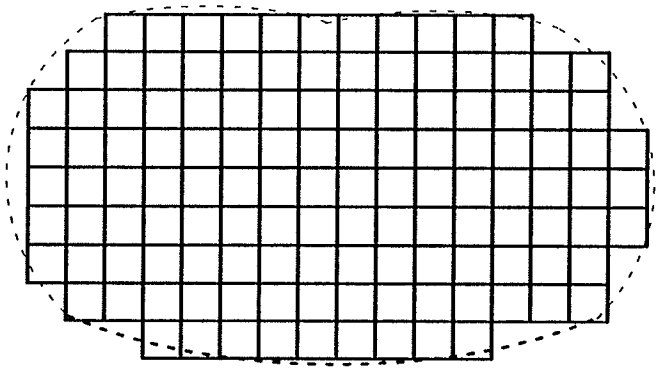

(b) A sample of finite element mesh used for the thorax simulation

Figure 7.6 Finite element models of thorax

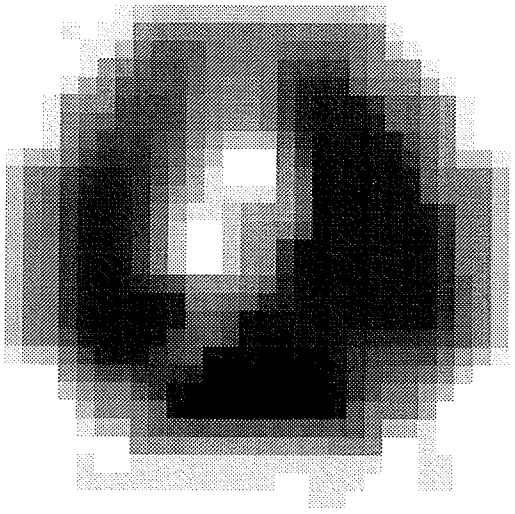

(a) Recovered image with coarse mesh

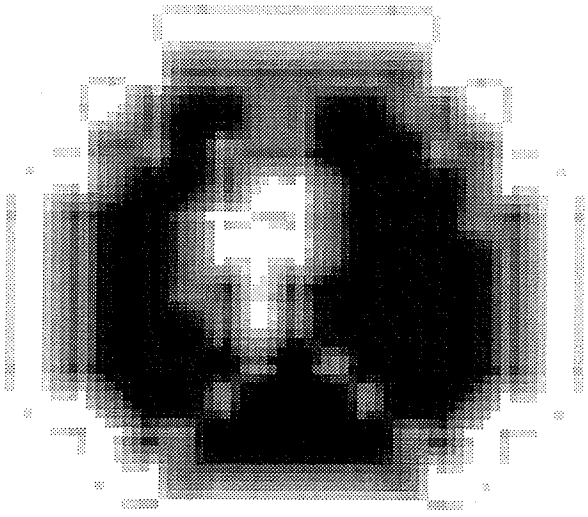

(b) Recovered image with finer mesh

Figure 7.7 Simulation results of thorax

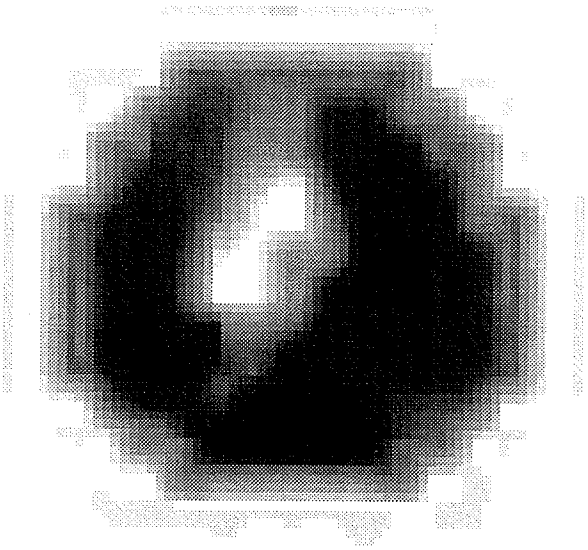

(c) Recovered image with finest mesh

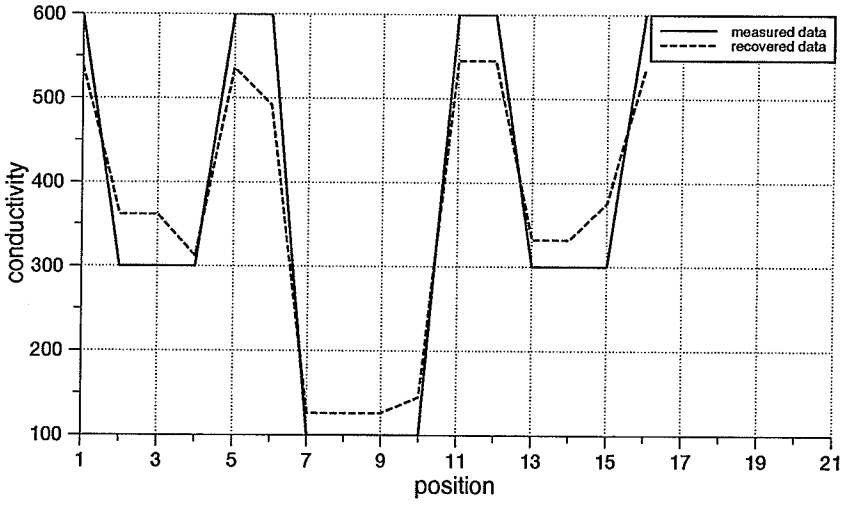

(d) Conductivity comparison on cross–section AA'

Figure 7.7 Simulation results of thorax

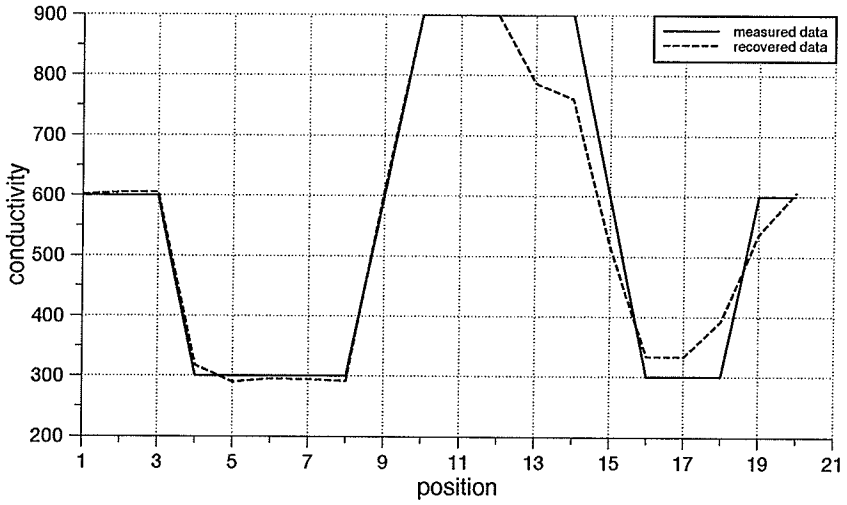

(e) Conductivity comparison on cross–section BB'

Figure 7.7 Simulation results of thorax

ments on image quality may be made by image restoration techniques and other image processing methods.

7.2 Finite Element Models Used in Three–Dimensional Simulations

7.2.1 Solid FEM model with linear elements

One way to create a finite element mesh for three–dimensional EICT imaging is to form a three–dimensional mesh with linear elements. A linear element has the simplest shape and least number of nodes. It is, therefore, easier to obtain an over–determined problem with such elements under the limited number of independent measurements and to save computing time as well as storage space for the large amount of data to be processed. Figure 7.8 shows the three–dimensional model we use in this thesis. The six sides of the body V to be examined are called top, bottom, left, right, front, and rear, respectively. There is an 8 x 8 square mesh at each layer of the body. The number of layers used in a particular problem

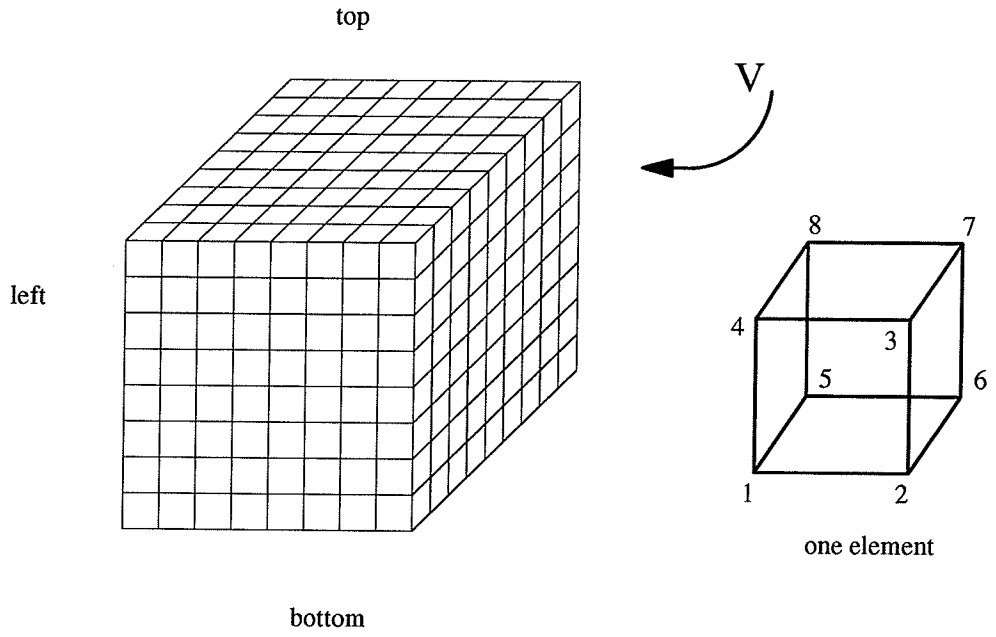

Figure 7.8 Finite element mesh with linear element in EICT three dimensional imaging

can vary.

7.2.2 Solid FEM model with higher–order elements

It is possible to use higher–order elements to design a three–dimensional finite element mesh. More computing power is needed to process the complicated mesh and large amount of data. This thesis will not discuss this problem. We believe that the principles and conclusions established by the mesh with linear elements will be applicable to the mesh with higher–order elements.

7.3 Effects of Excitations/Measurements on Three–Dimensional Imaging

Normally, a complete set of boundary measurements are available in two–dimensional EICT imaging. In three–dimensional EICT imaging, it is not always possible to have such a complete set because the measurements on some sides of a body cannot be made. The main issue associated with this feature in three–dimensional imaging is the reduced determinacy and the lower effectiveness of excitations/measurements placed on some of the six sides. There are more chances in three–dimensional imaging to deal with an under–determined problem.

7.3.1 Electrodes on top only

This is the most difficult case in three–dimensional imaging since the system with such excitation arrangements provides the least number of independent measurements. It often results in an under–determined problem. The mine detection problem belongs to this case. Figure 7.9 shows an example with the excitation/measurement patterns applied only on the top.

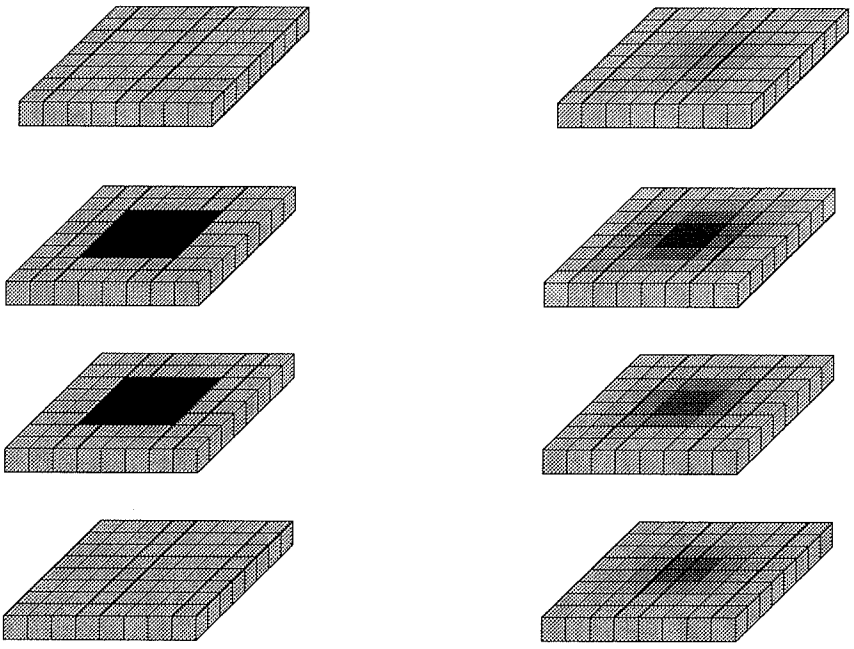

(a) Original image
Contrast 1:5

(b) Recovered image after 500 iterations

Figure 7.9 Three–dimensional imaging with top only excitations/measurements available

Four layers are used and the total number of unknown element conductivities is 256. If 8 excitations on the top layer is applied and sometimes measurement patterns are taken, there are $8 \times (81 - 2) = 632$ possible independent measurements, and $8 \times (32 - 2) = 240 < 256$

independent measurements used to recover the image. The problem is under–determined. The algorithm used is the Wexler algorithm without improvements. Figure 7.10 shows the

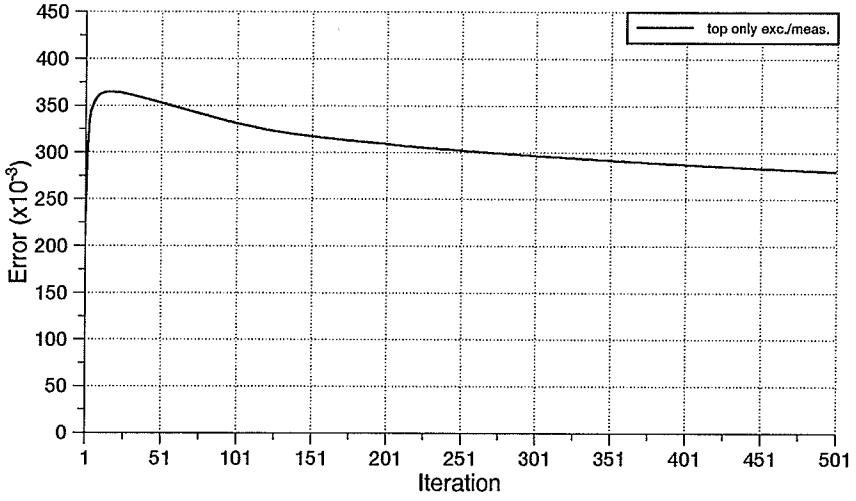

Figure 7.10 Error of the example in Figure 7.9

errors of the example in Figure 7.9.

The main effect of such arrangement is the low sensitivities of elements in deeper layers. As demonstrated in previous chapters, no matter how many excitation patterns is applied and how many measurements are obtained, only layers close to the top can be recovered reliably. First, only can objects in the shallow layers (close to the top layer where excitation/measurement patterns are applied) be recovered with reasonable accuracy. Secondly, errors in different layers are quite different, i.e. errors in shallow layers decrease while those in deeper layers increase. Thirdly, the total error starts increasing after a certain number of iterations. We have seen a very similar case in network recovery. This reflects the insensitivity of conductivity distributions in deeper layers to the far positioned excitation/measurement patterns.

If objects inside the body exist in even deeper layers, the top only excitations/measurements

cannot detect anything at all. If some electrodes are applied on the boundary every two layers, the images in deeper layers can be of much better quality.

The reason for not using the improvements developed in Chapter 4 and Chapter 5 in three–dimensional simulations is that the higher possibility of faulty detection in the layers which are not sensitive to the measurements. The significant errors in deeper layers with the top only excitations/measurements make it meaningless to apply the peak detection method and acceleration factor in those layers. One way to get rid of the faulty detection in deeper layers is to apply the peak detection method layer by layer and modifications are only made in those layers which can be controlled by the applied excitations/measurements, i.e. which are sensitive to the measurements.

7.3.2 Electrodes on four sides

This kind of problem has higher determinacy. When EICT is used to monitor the thorax of a human body, electrodes can be placed on the four sides, front, rear, left, and right, surrounding the body. Figure 7.11 and Figure 7.12 show the imaging results and error norm plots with four side excitations/measurements applied. There are three objects inside the body, which represent the two lungs and the heart, respectively. 8 layers are used in the three–dimensional model. 24 excitation pairs are placed around the body between the second and the third, the fourth and the fifth, and the sixth and the seventh layers, respectively. There are 24 x (32 – 2) = 720 independent measurements versus 64 x 8 = 512 unknowns. It is an over–determined problem. The images in middle layers are recovered with reasonable accuracy. Compared with what we have seen in Figure 7.10(b), the middle layer images have better quality, while the images on the top and at the bottom are recovered poorly since there is less information available from these two layers.

7.3.3 Electrodes on five sides

The reason that this case is discussed is that the detection of breast cancer with EICT is a similar case. As shown in Figure 7.13, only the measurements on the bottom are not possible. Considering the shape complexity and variations of a breast (in the case of chest imaging,

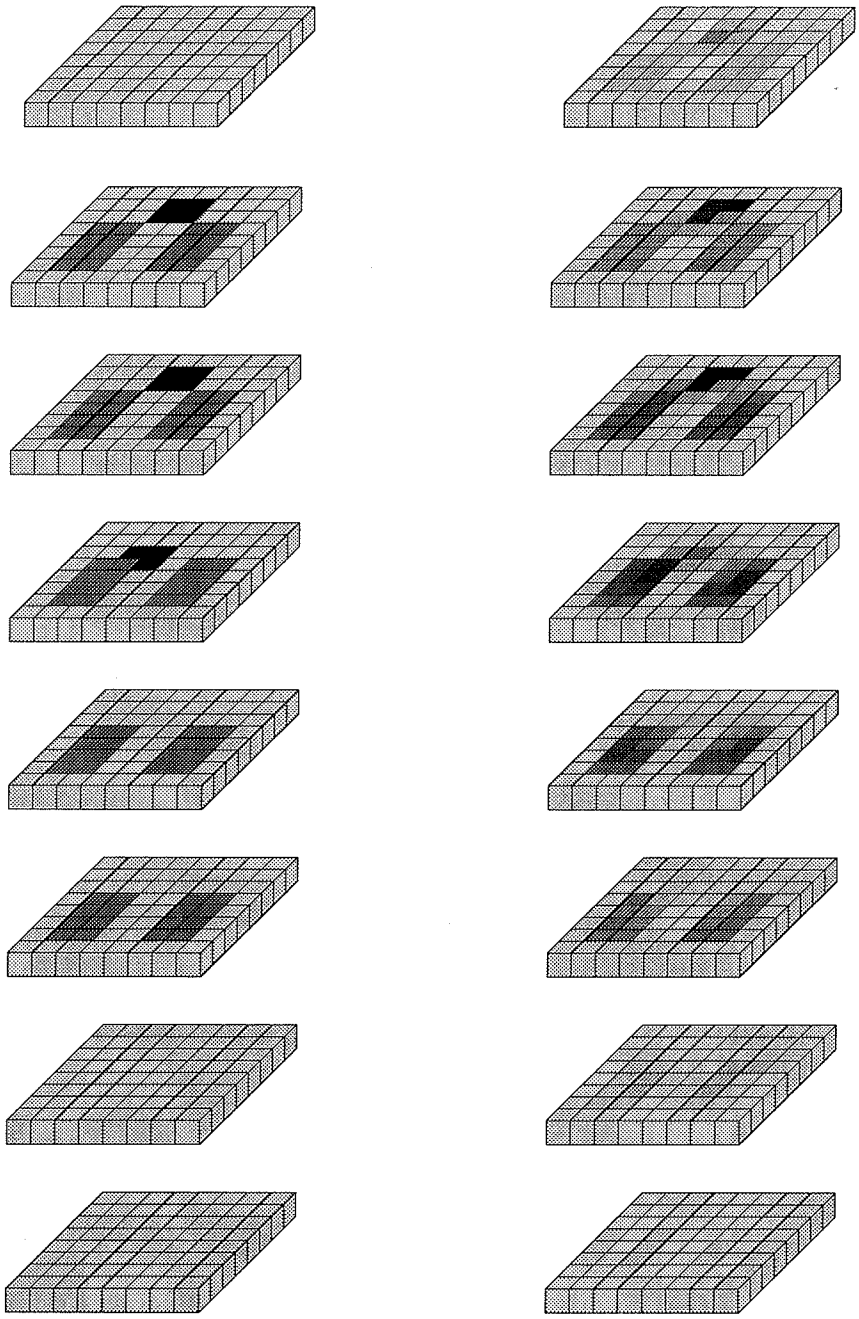

(a) Original image
Contrast 1:5:9

(b) Recovered image after 300 iterations

Figure 7.11 Three–dimensional imaging with four side excitations/measurements available

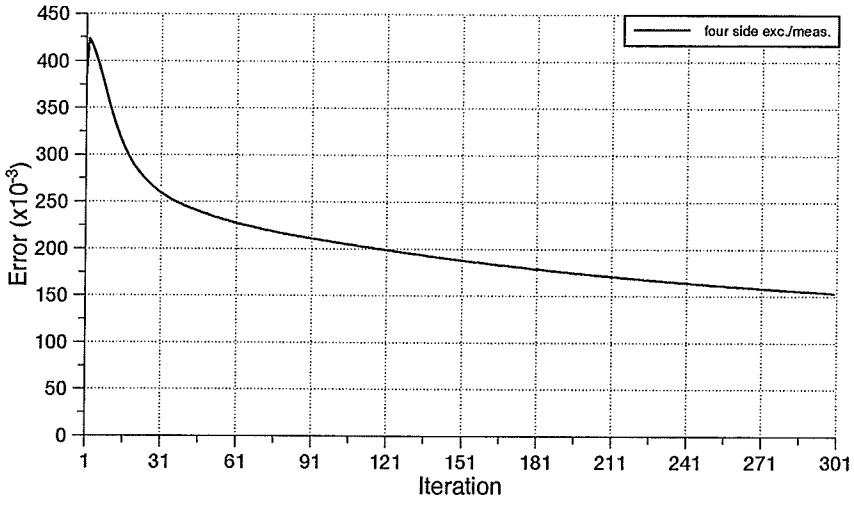

Figure 7.12 Error of the example in Figure 7.11

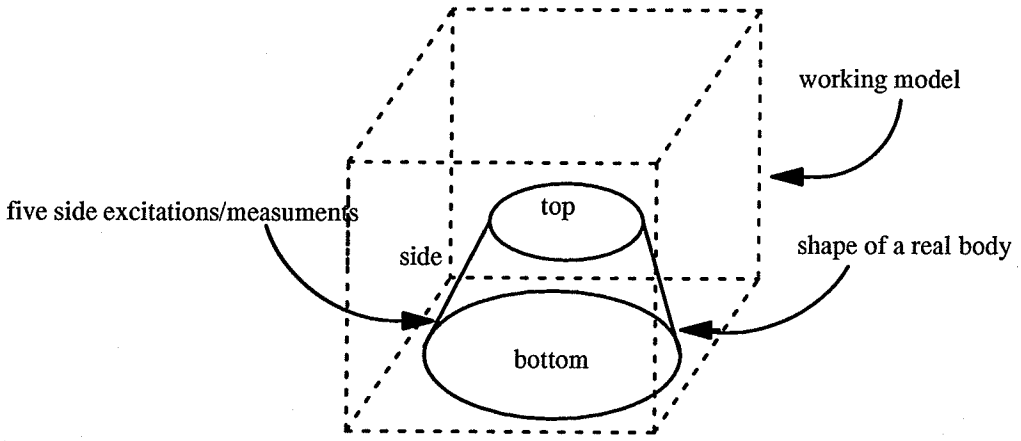

Figure 7.13 Working model design

the shape of the chest is close to rectangular), modelling a breast in three–dimensional imaging would be too costly. Therefore, we suggest, as we have discussed in the previous section, to build a device which has simpler shape for the electrode placement, and filled with some homogeneous materials with known conductivity (salty water, for example) between the boundaries of the real body and the device. Such device is then taken as the working model for EICT imaging.

Following the discussions on the four side excitations/measurements, we know that images with better quality can be obtained when the five side patterns are available. The problem is normally over–determined. Figure 7.14 gives an example with a smaller object inside a body, while excitations/measurements on top, left, right, front, and rear are applied.

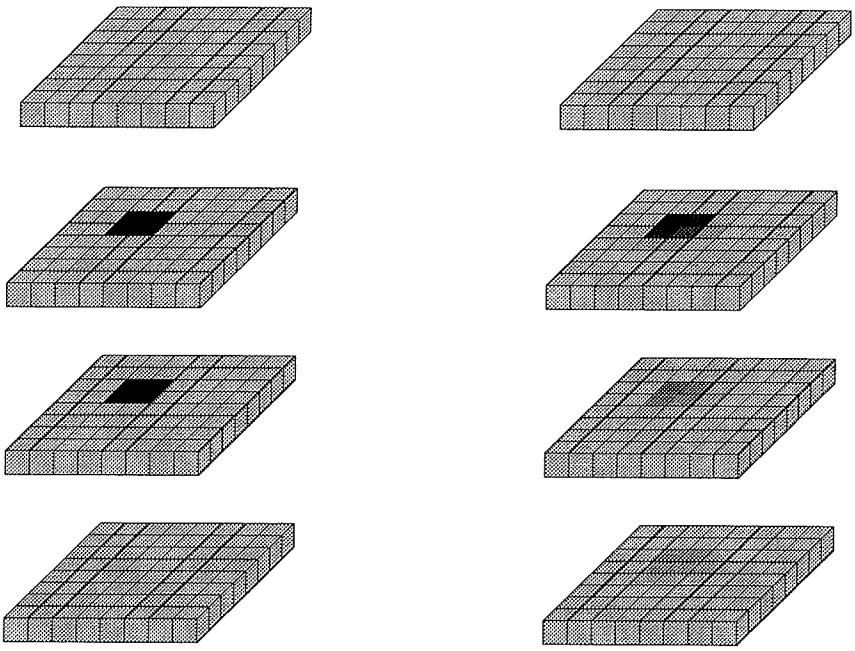

(a) Original image
Contrast 1:5

(b) Recovered image after 500 iterations

Figure 7.14 Three–dimensional imaging with five side excitations/measurements

CHAPTER 8

EICT SYSTEM DESIGN AND APPLICATIONS

Previous studies of algorithm improvements, mesh effects, and excitation designs show that a workable EICT system with error function minimization algorithms is possible. In this chapter, the fundamental principles that can be used to build an EICT system with error function minimization algorithms are first presented based on the results obtained from previous chapters. Then, as a practical example, a nuclear waste monitoring system currently under testing at Atomic Energy Canada Ltd is described.

8.1 Design Principles For EICT Systems

A set of principles to realize an EICT system for industrial purposes is proposed as follows.

8.1.1 Problem descriptions

In general, an EICT system with an error function minimization algorithm may be designed for a particular image problem, for example, mine detection and breast cancer diagnosis. The geometry and boundaries of the body and the number of applicable electrodes are known in advance. Some additional parameters are also available, such as background conductivity values, possible maximal (minimal) conductivity values, and the approximate positions of some objects in the body. The problem then is to decide whether a two– or three–dimensional model should be used.

8.1.2 Designing an EICT system

Step 1 Designing the working model for the system

Since the geometry of a body to be examined could be very complicated, it is sometimes easier to build a working model for the system to perform the EICT imaging by actually applying excitation/measurement patterns on the boundaries of the working model. A working model has simple shapes with low conductivity material filling between the boundaries of the mod-

el and the body. The reconstruction region then becomes larger and the filling material is part of the image. If the shape of the body is simple enough to model, the working model is not necessary.

Step 2 Designing the finite element meshes

Design two finite element meshes according to possible electrode positions. One is coarse, while the other fine. The sizes of individual elements should be determined based on the expected distinguishing accuracy. As we have discussed, the use of sometimes measurement patterns is good at eliminating the contact resistance. The approximate number of independent measurements for this pattern with N electrodes is about $N^2/2$. Then, for a cubic mesh as shown in Figure 7.7, if the length of each side of the mesh is L and the length of each side of one element is l, the expected element size can be calculated as $l > L / (N^{2/3} / 2)$.

Step 3 Designing excitation/measurement patterns

Assume an arrangement of electrodes and perform the sensitivity analysis with the pre–designed mesh. It is suggested to arrange electrodes as evenly as possible surrounding the boundaries of the working model. Since the change of excitation pattern arrangement is not practical in most of the cases, it is better to make as many measurements as possible unless the system restricts one to do so. Two types of excitation patterns are recommended for a two–dimensional problem according to the accessibility theory. First, each excitation pattern uses a pair of electrodes which are right across, as shown in Figure 8.1 (a). Secondly, each excitation pattern uses a pair of electrodes which covers a "corner" of the entire region, as shown in Figure 8.1 (b). Such patterns can approximately make most of the elements accessible at least for a coarser mesh. Then, the combination of these different excitations can be used to obtain a set of "semi–optimal" current patterns for the problem in topological sense. In the case that objects have relatively fixed sizes and positions, a standard set of excitation patterns can be set up after a series of trial cases is performed.

Step 4 Performing EICT imaging with the coarse mesh

The coarse mesh is first used to generate a trial image. If the average potential difference

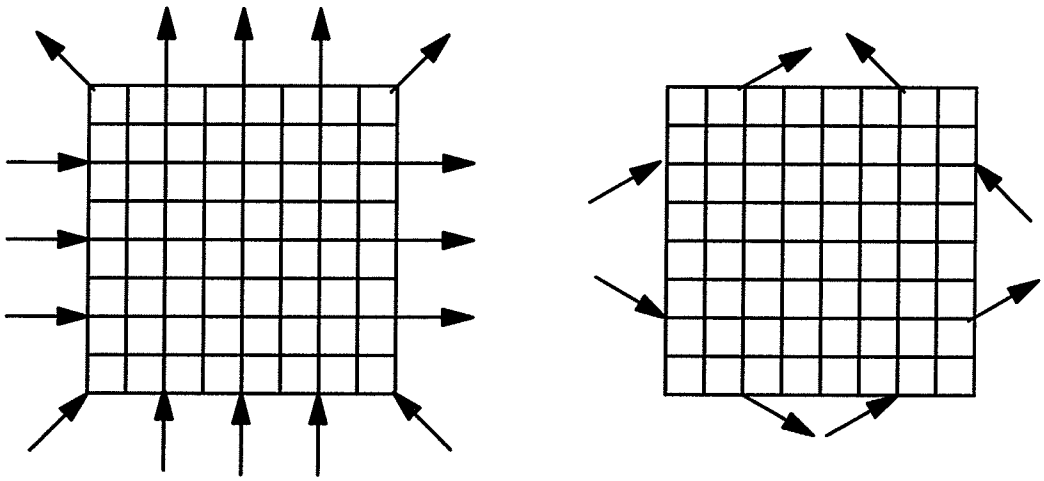

(a) Excitation pattern with each pair across (b) Excitation pattern with each pair covers a corner

Figure 8.1 Recommended excitation patterns

keeps going down as the iteration procedure proceeds, the mesh is the one which is suitable for this problem, and the trial image is the final one. If the average potential difference starts going up after a certain number of iterations, the mesh cannot represent the problem properly. Then, stop the imaging procedure and store the result.

Step 5 Performing imaging with finer mesh

A finer mesh is then switched on to continue the procedure. The stored result from the coarse mesh now becomes the initial guess of the conductivity distribution for the finer mesh. It would be better if this new mesh can be modified with elements of different sizes when the previous coarse mesh has given a blurred picture. In this case, smaller elements can be placed around the area where the object boundaries might be. Add more excitation patterns in and start the imaging procedure again. Repeat Step 4 and Step 5.

Step 6 Solving the under–determined problem

If the finer mesh still cannot provide a satisfactory image in Step 5, the problem can be treated as being under–determined. In the case that more electrodes can be added in, go to Step 2 and repeat the previous procedure. Otherwise, re–arrange the electrodes according to the method we discussed in Chapter 3 and Chapter 7 to make part of the region over–determined,

then go to Step 2.

8.1.3 Software recommendations

It is difficult to solve a three–dimensional EICT problem in a body with arbitrary shapes. The body with complicated geometry requires powerful software to calculate the field solutions in three–dimensions. There are some commercially available three–dimensional solvers to build three–dimensional finite element models for complicated geometry. One of them is I–DEAS from SDRC, which can create many three–dimensional shapes with a very user friendly interface.

8.2 An EICT Nuclear Waste Monitoring System in AECL

A nuclear waste monitoring system was built by AECL, Atomic Energy Canada Ltd., and has been under test for about a year. The preliminary results show good agreement between the theoretical solutions and the images generated from the EICT system. This is encouraging to apply this technique in a practical environmental protection problem.

8.2.1 Background in nuclear waste monitoring

Current approach of measuring the in–situ properties of Reference Buffer Material (RBM) at the Underground Research Laboratory (ULR), Atomic Energy Canada Ltd., is by taking direct measurements. The instruments are installed and readings are taken directly at their point of installation. There is great certainty in these measurements since the location of the measurements is precisely known, and the measurement is taken as directly as possible. However, since the scale of the currently performed experiments is so large, a corresponding large number of instruments has to be installed in order to get fine enough resolution of detail. This affects the results of the measurements since these instruments influence the measured properties of the system as a whole. As well, there is a great difficulty in accessing the instrument after installation and as a result, instruments often cannot be repaired, replaced, or maintained.

As a remote sensing technique, EICT provides an alternative way to measure ground water

infiltration of reference buffer material. In AECL, it is tested to be used to study components in Canadian Nuclear Waste Management Program's Concept of storing high–level radioactive waste by measuring saturation levels in buffer material since impedance values relate directly to saturation levels. The RBM is the primary engineered boundary between high–level radioactive waste and the sensitive biological systems, and fluid transported by ground water is the primary means of carrying the contaminates between these systems. It is critical to the Canadian Nuclear Waste Management Program to be able to study ground water flow in RBM to verify the Concept.

8.2.2 Problem description and system design

The region to be studied is a cylinder with measuring points contacting to the depth of 240 meters underground. A data acquisition system has been constructed along with a laboratory experimental apparatus to verify that measurements can be taken and valid results can be determined by this approach. The method works through injecting current into one or more electrode pairs in contact with the buffer and measuring voltages at all electrodes[35, 36]. Two finite element meshes, one coarse and one fine, are designed for this EICT system. The element used in both meshes is quadratic element with 9 Gauss points. There are 32 electrodes arranged on the circular boundary with 10 of them to be taken as excitation pairs. With the *sometimes* pattern in measurement, for the coarse mesh, there are $10 \times (32 - 2) = 300$ independent measurements corresponding to 113 unknown element conductivities; while for the fine mesh, the same number of independent measurements are used to recover 196 unknown element conductivities. The preliminary results show good agreement between the theoretical data and the data from the images recovered with EICT algorithms. It indicates the promising of this technique in environmental applications.

CHAPTER 9

CONCLUSIONS AND FUTURE RESEARCH

Three–dimensional applications of EICT are the reasons for studying this topic. Efficient and stable algorithms are important to the success of EICT systems. This thesis carries out research on finding algorithms which are suitable for three–dimensional EICT imaging by comparing different algorithms, not only in terms of speeds of convergence but also their ability to process large amounts of data from three–dimensional systems in a robust manner. Error function minimization algorithms discussed in this thesis partially meet these requirements. The ability of solving under–determined problems using such algorithms is explained. The cause of slow convergence with error function minimization algorithms is investigated in detail and new adaptive schemes are introduced to speed up the convergence process. Excitation effects and design rules for better excitation patterns are initially discussed, with sensitivity and accessibility analyses using network approaches. Methods of increasing resolution under limited number of independent measurements and using finite fineness meshes are proposed and tested. Simulations in two– and three–dimensional problems are performed. The measurement error effects are discussed with two–dimensional examples. Excitation effects on image quality in three–dimensional imaging are studied. The conclusions of these investigations are then summarized in the form of a set of guidelines for building a successful EICT industrial machine.

9.1 Conclusions

Comparisons of EICT algorithms with iterative characters Previous research focused on matrix inversion algorithms and evaluated different algorithms mainly by comparing speed of convergence in terms of iterations.

1. Matrix inversion algorithms

These algorithms use Newton–Raphson–like procedures to obtain acceptable solutions. Dense matrices cannot be avoided with these algorithms, which restricts the algorithms ability to deal with large three–dimensional systems.

Matrix inversion requires that the number of independent measurements be larger than the number of unknown element conductivities. As the number of electrodes may be limited in an EICT system, necessary compromise for such a condition results in a relatively coarse finite element mesh. Thus, these algorithms, in general, cannot recover an image with desired details.

Since the internal information is mapped onto the boundary measurements, matrix inversion algorithms are more sensitive to measurement noise or boundary distortions. Such mapping is efficient only when the entire mesh to be imaged is accessible.

Most simulations with matrix inversion algorithms have been done by assuming some degree of congruency between the objects and finite element meshes. Therefore, the testing condition is artificial rather than practical since it is impossible to design a mesh to accommodate completely unknown objects.

2. Error function minimization algorithms

The speed of convergence of EICT algorithms should not be used as the only factor for algorithm evaluations, especially when the algorithms have different objectives. Compared with matrix inversion algorithms, error function minimization algorithms have more advantages which have not been fully studied.

Error function minimization algorithms do not result in dense matrices. Sparse matrices from such algorithms make it possible for the algorithms to process large amounts of data from three–dimensional systems.

Most importantly, error function minimization algorithms can solve under–determined problems which are more realistic in applications. In the real world, an EICT problem with a limited number of measurements is always under–determined in the sense of representing

infinite details in a continuous field problem with finite models. Therefore, error function minimization algorithms are more suitable to the naturally occurring problems.

Error function minimization algorithms calculate new element conductivities one element at a time. They are thus more robust for measuring errors and boundary distortion.

Simulations without congruency between objects and finite element meshes are successfully performed and image qualities are compared.

Algorithm improvement The least squared technique proposed for the error function minimization algorithm is good at providing the convergence direction for the algorithm and keeping a currently best solution. By combining image processing and function minimization techniques, improvements and modifications to EICT so that they speed up the convergence procedures. Two proposed schemes in this thesis have proven to be efficient and reliable.

Network models for EICT Network recovery with error function minimization algorithms help identify problems from EICT algorithms and systems. They can also be used to discuss the characteristics of EICT systems.

Numerical and topological features represent two aspects of an imaging system. Numerical features depend on the system's parameters, while topological features of the system, which have been neglected previously, reflect the structure information which is not parameter dependent.

Sensitivity and accessibility analyses are essentially employed in this thesis to study EICT with network methodology. Reliable convergence regions can then be identified according to different EICT problems. Effective excitation patterns, which do not need to be changed during the imaging procedure, are determined based on such regions.

Resolution improvement with mesh interpolation When the number of independent measurements is limited, image resolution with these algorithms can still be improved by interpolating the element conductivity values in updating procedures without increasing the complexity of meshes and computation effort. With the methods introduced in this thesis, a

proper mesh can be found for each individual imaging problem.

System design A set of guidelines for building a successful EICT industrial machine is also proposed in this thesis.

9.2 Future work

Future research on EICT algorithms and systems can be addressed as follows:

1. The limitations of the EICT systems with error function minimization algorithms need more study.

2. Sensitivity analysis should be further investigated and be employed in the peak–detection method to decide, more intelligently, the regions where updating element conductivity should be accelerated.

3. The peak detection method in three–dimensional imaging needs to be implemented.

4. The improved image resolution with the peak detection method needs to be evaluated more thoroughly.

5. More tests, in simulation and in experiments, are needed to verify the guidelines proposed in this thesis for building a successful EICT system.

6. Measurement effects, such as skin effect (e.g. in breast cancer detection), need to be discussed.

7. More investigations are needed to explore the relationships between the sensitivity/accessibility and excitation/measurement patterns so that better final image can be obtained.

8. Network recovery proves that the principles and algorithms of EICT can be used in fault diagnosis of printed circuit boards. Research can be performed to investigate the possibilities and limitations.

REFERENCES

[1] Anderson, D.K, Tozer, R.C., and Freeston, I.L., Backprojection in an induced current impedance imaging system, Proc. IEEE 15th Ann. Conf. of Eng. in Med. and Biol. Soc., 80–81, 1993

[2] Bates, R. H. T., McKinnon, G. C., and Seagar, A. D., A limitation on systems for imaging electrical conductivity distributions, IEEE Trans. Biomed. Eng., Vol. BEM–27, 418–420, 1980

[3] Berryman, J.G., and Kohn, R., Variational Constraints for Electrical Impedance Tomography, Physical Review Letters, vol. 65 No.3, 325–328, 1990

[4] Berryman, J.G., Lecture notes on Electrical impedance tomography, Lawrence Livermore National Laboratory, Livermore, California, U.S.A., 1992

[5] Chari, M. V. K., and Silverster, P. P., Eds., Finite elements in electrical and magnetic field problems, Wiley, New York, 1980

[6] Cheney, M. and Isaacson, D., Distinguishability in impedance imaging, IEEE Trans. Biomed. Eng., vol. BEM–39, 852–860, 1992

[7] Chua, Leon O. and Lin, Pen–min: Computer–Aided Analysis of Electronic Circuits: Algorithms & Computational Techniques, Prentice Hall, 1971.

[8] Dijkstra, A. M., Brown, B. H., Leatherard, A. D., Harris, N. D., Barber, D. C., and Edbrooke, D. L., Review clinical applications of electrical impedance tomography, J. Med. Eng. & Tech., Vol. 17, No 3 89–98 May/June 1993

[9] Fry, B., A resistive tomography algorithm, M. Sc. Thesis, Department of Electrical Engineering, The University of Manitoba, Winnipeg, Canada, 1983

[10] Gisser, D. G., Isaacson, D., and Newell, J. C., Current topics in impedance imaging, Clin. Phys. Physiol. Meas. Vol. 8, Suppl. A, 39–46, 1987

[11] Guardo, R., Boulay, C., Murray, B., and Bertrand, M., An experimental study in electrical impedance tomography using backprojection reconstruction, IEEE Trans. on Bio. Eng.,

Vol 38, No 7, 617–627, 1991

[12] He, X. and Zhou, S., A reconstruction algorithm for electrical impedance tomography, Proc. IEEE 14th Ann. Conf. of Eng. in Med. and Biol. Soc., 1686–1688, 1992

[13] Henderson, R.P. and Webster, J.G., An impedance camera for spatially specific measurements of the thorax, IEEE Trans. Biomed. Eng. 25, 250–254, 1978

[14] Hua, P., Webster, J. G., and Tompkins, W. J., A regularized electrical impedance tomography reconstruction algorithm, Clin. Phys. Physiol. Meas. Vol. 8, Suppl. A, 137–141, 1988

[15] Hua, P., Woo, E., Webster, J. G., and Tompkins, W. J., Iterative reconstruction methods using regularization and optimal current patterns in electrical impedance tomography, IEEE Trans. Med. Ima. Vol. 10, 621–628, 1991

[16] Hua, P., Woo, E., Webster, J. G., and Tompkins, W. J., Improved methods to determine optimal currents in electrical impedance tomography, IEEE Trans. Med. Ima. Vol. 11, No 4, 488–495, 1992

[17] Isaacson, D., Distinguishability of conductivities by electric current computed tomography, IEEE Trans. Med. Imaging, MI–5, 91–95, 1986

[18] Kejariwal, M., Kaster, K., Jurist, J. and Pakanati, J., Breast cancer detection using electrical impedance tomography: SPICE simulation, IEEE International Symp. BEM, 1993

[19] Kohn, R.V. and Vogelius, M., Relaxition of a variational method for impedance computed tomography, Comm. Pure Appl. Math. 40, 745–777, 1987

[20] Liu, W., Hua, P., Webster, J.G., Three–dimensional reconstruction in electrical impedance tomography, Clin. Phys. Physiol. Meas. Vol. 9, Suppl. A, 131–135, 1988

[21] Mayeda, W. and Peponides, G., Determination of component values in passive networks under limited measurements, Proc. 12th ASLOMAR Conf., 761–764, 1979

[22] Mikhlin, S.G., Variational methods in mathematical physics, Oxford: Pergamon Press, 1964

[23] Mu, Z. and Wexler, A.: Electrical impedance computed tomography—algorithms and applications, IEEE International Symp. on Medical Imaging, Nov. 1993

[24] Mu, Z. and Wexler, A.: Electrical impedance computed tomography in three dimensional applications, IEEE International Symp. on Antenna and Propagation, June 1994

[25] Mu, Z. and Wexler, A.: Electrical impedance computed tomography with the point–accumulative and point–iterative algorithm, Accepted paper for ANTEM 1994

[26] Mu, Z. Strobel, G., and Wexler, A.: Monitoring Buffer Material In High–Level Radioactive Waste Repositories With Electrical Impedance Computed Tomography, Accepted paper for ANTEM 1994

[27] Murai, T. and Kagawa, Y., Electrical Impedance Computed Tomography Based on a Finite Element Model, IEEE Trans. Biomed. Eng., vol. BEM–32, 177–184 1985

[28] Nakonechny, R. L., A preconditioned conjugate gradient method using a sparse linked–list technique for the solution of field problems, M.Sc. Thesis, Department of Electrical Engineering, The University of Manitoba, Winnipeg, Canada, 1983

[29] Newell, J.C., Gisser, D., and Isaacson, D., An electric current tomography, IEEE Trans. Biomedical Eng., Vol. 35, No. 10, 828–834, 1988

[30] Newell, J.C., Gisser, D., and Isaacson, D., Images from an adaptive current tomography, Proc. IEEE 10th Ann. Conf. of Eng. in Med. and Biol. Soc., 275–276, 1988

[31] Price, L.R., Electrical impedance tomography (ICT): A new CT imaging technique, IEEE Trans. Nuclear Sci. Vol. NS–26, No 2, 2736–2739, 1979

[32] Seagar, A.D., Barber, D.C., and Brown, B.H., Electrical Impedance Imaging, IEE proceedings, Vol. 134, Pt.A, No.2, 201–210, 1987

[33] Shaw, J.G., A point–iterative, variational, finite–element algorithm for three–dimensional vector fields, Report TR81–6, Department of electrical Engineering, The University of Manitoba, 1981

[34] Stanley, R., Abildskov, J.A., and McFee, R., Resistivity of body tissues at low frequencies, Circulation research, Vol. XII, 40–50, 1963

[35] Stroble, G., Mu, Z., and Wexler, A.: Using electrical impedance measurements to image saturation levels for monitoring buffer material in high–level radioactive waste repositories,

Proc. ANTEM 1992

[36] Strobel G., Impedance computed tomography for monitoring moisture content in clay–based buffer, Report TR–586, Geotechnical Science and Engineering Branch, Whiteshell Laboratories, Atomic Energy of Canada Limited, 1993

[37] Tamburi, A., Roeper, U., and Wexler, A., An application of impedance computed tomography to subsurface imaging of pollution plumes, Field Methods for Ground Water Contamination ASTM STP963, 1988

[38] Telford, W. M., Geldart, L. P., Sheriff, R. E., and Keys, D. A., Applied Geophysics, Cambridge U. P., London, 1976

[39] Tozer, R., Simpson, J., Freeston, I., and Mathias, J., Noncontact induced current impedance imaging, Electronics Letters, Vol 28, No.8, 773–774, 1992

[40] Truyen, B., Cornelis, J., and Vandervelden, P., Image reconstruction in electrical impedance tomography: A selfadaptive neural network approach, Proc. IEEE 15th Ann. Conf. of Eng. in Med. and Biol. Soc., 72–73, 1993

[41] Wexler, A., Fry, B. and Neuman, M.R., Impedance–computed tomography algorithm and system, Appl. Opt. 24, 3985–3992, 1985

[42] Wexler, A. and Fry, B., Reconstruction system and methods for impedance imaging, U.S. Patent 4 539 640, Sept. 3, 1985

[43] Wexler, A., Finite elements for technologists, report TR80–4, Department of electrical Engineering, The University of Manitoba, 1980

[44]Woo, E. Hua, P., Webster, J. and Tompkins, W., Measuring lung resistivity using electrical impedance tomography, IEEE Trans. Biomed. Eng., vol. BEM–39, 843–852, 1992

[45]Woo, E. Hua, P., Tompkins, W. J., and Webster, J. G., A finite element model with node renumbering for adaptive impedance imaging, Proc. IEEE 10th Ann. Conf. of Eng. in Med. and Biol. Soc., 277–278, 1988

[46] Yorkey, T. J., Webster, J. G., and Tompkins, W. J., Comparing reconstruction algorithms for electrical impedance tomography, IEEE Trans. Biomed. Eng., vol. BEM–34, 843–852,

1987

[47] Zhou, X. and Gordon, R., Detection of early breast cancer: An overview and future prospects, Critical reviews in biomedical engineering, Vol. 17, Iss. 3, 203–255, 1989